NEW APPLICATIONS OF SEISMIC IMAGING IN RESOURCES EXPLORATION BASED ON SEISMIC ATTRIBUTES ANALYSIS AND SEISMIC INTERFEROMETRY

タレク サミール アブデル アジズ アリ イマム

https://hdl.handle.net/2324/6787587

出版情報：Kyushu University, 2022, 博士（工学），課程博士
バージョン：
権利関係：

NEW APPLICATIONS OF SEISMIC IMAGING IN RESOURCES EXPLORATION BASED ON SEISMIC ATTRIBUTES ANALYSIS AND SEISMIC INTERFEROMETRY

TAREK SAMIR ABDEL AZIZ ALI IMAM

2023

NEW APPLICATIONS OF SEISMIC IMAGING IN RESOURCES EXPLORATION BASED ON SEISMIC ATTRIBUTES ANALYSIS AND SEISMIC INTERFEROMETRY

By

TAREK SAMIR ABDEL AZIZ ALI IMAM

A dissertation submitted in partial fulfillment of requirements

for the degree of

Doctoral Engineering

Examination Committee:

Prof. Akira Imai (Chairman)

Prof. Takeshi Tsuji

Assoc. Prof. Tatsunori Ikeda

Assoc. Prof. Takashi Sasaoka

九州大学
KYUSHU UNIVERSITY

Department of Earth Resources Engineering

Graduate School of Engineering

Kyushu University

Japan

January 2023

Abstract

Geophysics has been essential in appraisal, reservoir characterization, drilling, well completion, and production since early stages of the exploration of resources. However, the effectiveness of using the geophysical technologies varies and is still facing many challenges such as data collection from the topographic areas and data analysis for imaging of complicated structures and deep sophisticated reservoirs. A wide frequency of signal, amplitude preservation, high precision and data integration are also challenges and key concerns in the seismic approach. Seismic exploration is the use of seismic energy to investigate the earth's subsurface not only for commercial oil, gas, or mineral reserves, but also for other engineering, archeological, and scientific research. The main objective of seismic exploration is to obtain high-precision seismic imaging, which ensures the accuracy of geological interpretations. With the development of seismic exploration, the targets of the seismic survey become more complex. Imaging on complex media like subsalt and small-scale, steeply-dipping structures, and heterogeneous structures brings a great challenge to the imaging techniques. In this study, I applied seismic-based approach for the complex geological imaging based on seismic attributes analysis and seismic interferometry approach. In the seismic attribute analysis, I used the seismic reflection data acquired from the active seismic surveys using the air gun and data recorded from the boreholes for structural mapping and imaging purposes. In the seismic interferometry approach, I utilized mainly the artificial blast mining signals to image the shallow subsurface structures of a minefield, beside using the other passive sources (i.e., natural earthquakes and ambient noise) to compare the results from different sources. This dissertation contains four chapters, and their descriptions are as follows.

Chapter 1 explains the research background, motivation, and objectives. In this chapter, I introduce some previous studies on the seismic attributes and the seismic interferometry methods used to image the subsurface structures associated with the resources.

In Chapter 2, the Ras El Ush field (Gulf of Suez, Egypt) characterized by complex geologic setting, which results in difficulties in terms of high-resolution seismic interpretation, was investigated. This study interpreted post-stacked reflection seismic and well data comprising the check shot velocity data to obtain and investigate detailed information about the structural fault orientation and dip of the Ras El Ush field. Seismic attributes were employed to improve the fault attributes by eliminating noise and residue of non-faulting events. Detailed enhanced structural modeling was achieved by integrating explicit faults, horizons, and selected zones into a three-dimensional grid. The models helped define geological discontinuities and structural traps, which would help develop the field and nearby similar hydrocarbon fields in the Gulf of Suez (Egypt).

In Chapter 3, the seismic data from natural earthquakes, ambient noise and mine blasts were analyzed to map P-wave reflection profiles at the Hishikari mine area by autocorrelation analysis. Because fissure-filled gold veins are dominant in this area, the potential of autocorrelation analysis for investigating the shallow subsurface was evaluated, including the ore deposits. Seismic interferometry is commonly performed based on the autocorrelation of ambient noise or natural earthquake signals; here, blasting in the mine was used instead since blast events include high-frequency signals that boost the spatial resolution of the imaging. Auto-correlograms were successfully obtained showing high-resolution seismic reflectors at shallow formation depths (< 500 m depth). A comparison with profiles obtained from ambient noise and earthquake data showed that blasting signals yielded highly spatially consistent reflections that would not be achievable with natural or ambient seismic sources. This study highlights the potential of using blast autocorrelation seismic analysis which can be done for short survey periods. By using a single blast shot and dense distribution of seismic stations, higher resolution 3D reflection images of lithological interfaces were successfully achieved, possibly including heterogeneities associated with ore veins.

Chapter 4 summarizes the results, key findings, and conclusion of this thesis, and a possible future vision is described. The results derived from the proposed methods demonstrate that further processing techniques and seismic attributes for the pre-stacked and post stacked data can resolve the distortion and the masking of seismic energy especially by the evaporite layers and complex structures. Also, using the blast as a source of seismic waves for the minefields in a short time survey could be a low-cost option to provide high-resolution information and images of the shallow subsurface structures of minefields.

Acknowledgement

Foremost, I thank my God (Allah) for everything and for countless gifts and blessings in my life. Also, I’d like to thank all my family, dear parents (father and mother), if I tried to thank them all my life, I could not return them the enough gratitude, without them I would be nothing, they are always supporting and taking care of me. I thank my lovely wife Heba for being my life partner, she always supports, encourages, and believes in me to be the best version of myself, she always provides the environment to work and study. The fruit of my life is my son Yahia, we have many funny and special moments, he gives my life precious meaning. I thank my brothers and sister who always present for help, and they find the time to communicate even the long distances.

Firstly, I am deeply thankful and extremely grateful for my supervisor Professor Takeshi Tsuji (University of Tokyo), one of the greatest researchers in the seismic field, he always shares his wide expertise and valuable knowledge with me and other students. I see him an extraordinary mentor, also I consider myself very lucky to be one of his students, it is a great honour for me. He is ambitious, active, intelligent, humble, polite, and respectful person. He is distributing positive energy, brilliant ideas, and good chances for everyone. I thank him for giving me the opportunity to work and promote my research with him. I learned much from him, he always has a plan and can easily distinguish the interesting points in any research. Also, he always pushes his students for the best and supports them by all possible means for achieving that.

I am also sincerely thankful for Associate Professor Tatsunori Ikeda (Kyushu University), he is very diligent, hard-working, full energy and cheerful person, I learned from him to be accurate, never to give up and always study more. Indeed, I learned from him a lot in the signal processing and analysis. His technical guidance has solved several research points that facilitated having good results. He always helps and supports the students by giving them much of his time. A special way of teaching is giving the clues and put you on the way, the quote: “Give a man a fish, and you feed him for a day. Teach a man to fish, and you feed him for a lifetime” is describing exactly what he does. I had always fruitful discussions with him.

I thank Professor Akira Imai (Kyushu University) for being my official supervisor and taking care of me. He is a very good and kind person. I learned from his research in the work of Hishikari gold mine. I thank him for being flexible and helpful with me. It is a great honour for me to deal with him.

Many thanks for Associate Professor Takashi Sasaoka (Kyushu University) for examining my dissertation, his reputation is well-known with the good personality, kindness, and high-quality research and teaching.

I feel gratefulness for the Ministry of Higher Education and Scientific Research, Egypt and Japan International Cooperation Agency (JICA) to fully fund and support my Ph.D. study through a Grant-in-Aid by the Egypt-Japan Education Partnership (EJEP) for developing human resources.

I much appreciate Kyushu University for hosting me, facilitating the circumstances and environment to have a good time, study, work, research and innovate. It was my beloved home in the past three years. Moreover, I want to say thank you for Kyushu University officer staff Yoko Kimura and Yasura Oiwa. They have given many supports related to administrative issues during my life in Japan.

I am grateful for the Egyptian General Petroleum Corporation (EGPC) and Gebel El Zeit Petroleum Company (PetroZeit) for providing seismic and well data for the study area (Ras El Ush) and their approval to use the data of the study described in chapter 2.

I am very thankful to Sumitomo Metal Mining Co., Ltd and Hishikari mine staff for providing the permissions to use and help in collecting the seismic data in the study described in chapter 3. Special thanks for Jiro Uesugi, Takeshi Nakamura, and Yoshinori Okaue. This study was supported by Kakenhi grant JP20H01997, JP20K04133 and JP21H05202 from the Japan Society for the Promotion of Science (JSPS)

Many thanks to my lab mates and colleagues in the Exploration Geophysics Department, for their help, support and sharing the special moments. Special thanks to Ichiro Hagimori, Shuto Takenouchi, Kota Mukumoto, Tomoki Uchigaki and Shuhei Tsuji for helping in the field survey of the Hishikari gold mine.

I am delighted to know and meet many good people in Kyushu University and Fukuoka such as the Egyptian friends Mohmed Shehata, Tamer Farag, Ahmed Bahaa, Ahmed Gendia,

Amany Harby and others. We had good memories and time together; they help and support whenever they could.

I much loved Japan and feel loyal to this beautiful country, and I consider it now my second home country. I have spent more than three years in Japan which are from the best years of my life, and I wish I could visit it again. This country is very special, has a magic environment to create, innovate and show the best of your skills and interests. I enjoyed the respectful manner of the people, the nature, cleanness, and fantastic seasons: Spring with Sakura trees and Autumn with red and yellow falling leaves. I am fascinated by the whole doctoral journey in Japan, which had a great influence on me, and I believe it will long last.

The Ph.D. journey Is considered for me like a small scale of the story of life. I failed, got upset and disappointed many times but with feelings of passion, motivation, enthusiasm, and ambition, I learned from the mistakes and finally succeed. Never give up and always try, even in other ways than traditional ones till you achieve is the main lesson I got from this journey. The Ph.D. journey was for me the first step to learn how to be a good independent researcher who can serve the community and this journey has just started. Many thanks for everyone had influenced me positively or negatively because I learned and got developed from both.

Fukuoka, January 2023

Tarek Samir Imam

Table of Contents

List of Tables

List of Figures

Chapter 1

Introduction

1.1 Research background and motivation

Earth resources are in great demand by humans as a source of power and electricity used in essential daily life activities and transportation. Also, the buried valuable minerals are used for various industrial and construction purposes. Therefore, mapping and imaging the subsurface structures by geophysical methods are beneficial to avoid the high cost of unsuccessful and unsafe drilling to extract these buried resources. Seismic methods based on the reflected seismic waves could provide helpful information about the underground physical properties to the extent of the detailed high-resolution images. Most of the seismic wave analysis research is to understand the geological structures and the properties of subsurface rocks as density, velocity, and elastic properties from the nanoscale (microscopic) to the geological scale (macroscopic). The investigation of the rock properties from seismic wave features is not only applied on the Earth (terrestrial) but also was extended outside the Earth to the Moon, Mars, and maybe other planets in the future (extraterrestrial) in attempts to provide insights about the planetary structures and possible associated resources. Therefore, analyzing the seismic wave propagation and reflection is vital in exploring the unconventional earth resources buried or confined under the surface of the Earth at the geological layers and structures within various depths. Moreover, this analysis could be helpful for other applications such as imaging and monitoring the reservoirs of the Carbon Capture Storage (CCS) and geothermal sites for predicting the CO2 leakage and the associated seismic activity that may occur due to the pore pressure resulting from the fluid injection (Chhun and Tsuji, 2020).

Seismic attributes are quantities derived from the seismic data that describe a seismic trace's shape or other characteristics over a specified time interval (or depth, if the seismic data has been converted to depth) (Misra and Mukherjee, 2018). Seismic attributes can be derived from a single trace by comparison of multiple traces or from an interpreted seismic horizon. Examples of seismic attributes are wavelet shape, frequency, amplitude, phase, acoustic impedance, envelope, chaos, ant-tracking, dip illumination, and complex trace information contained in transforms of the real trace (Marfurt and Alves, 2015). Also, seismic images generated using seismic attribute volumes enhance or quantify certain anomalies or characteristic features unrecognizable from the original amplitude data (Taner et al., 1979; Basir et al., 2013; Brown; 2001; Pedersen, 2002; Eng and Tsuji, 2019). Seismic attributes have been increasingly used in exploration and reservoir characterization and integrated into seismic interpretation. Seismic attributes are essential because they enable interpreters to extract hidden information from seismic data, and have been used to identify prospects, ascertain depositional environments (e.g., fluvial or deep-water channels, carbonate buildups), detect and enhance faults and fracture sets to unravel structural history, and even provide direct hydrocarbon indicators. They have proven helpful in geological settings, such as clastic, carbonate, salt-related basins, and tectonic regimes, including extensional, strike-slip, and compressional. Developments in digital recording and modern visualization techniques greatly impacted the growth of seismic attributes in the past decades. The geological setting of the Ras El Ush field in chapter 2 is complex and comprises several structures such as evaporites, high fracture zones, and unconformities due to the presence of the field in the active rift zone of the Gulf of Suez and this field is subjected to different tectonic stress trends. Therefore, we developed methods of seismic imaging to explore such geophysical reserve fields. The proposed methods in chapter 2 could also be effective in investigating similar geological formations of the unconventional earth resources targets, such as the geothermal power fields, which commonly have complex geologic settings from the occurrence of volcanic intrusions, severe faulting, and unconformities. In chapter 2, the developed method comprised the following attributes: seismic conditioning and structural smoothing and 3D edge enhancement and fault detection for better visualization of the data's seismic profiles and occurred complex faults in addition to using modern modeling techniques and advanced interpretation tools to construct detailed 3D structural models of the formations of primary interest to assist in defining the geological discontinuities and structural traps for development of the field.

Seismic interferometry is a seismic technique by which we can obtain Green's function by autocorrelating the seismic data recorded by a single receiver (Schuster et al., 2004; Schuster, 2009; Wapenaar & Fokkema, 2006; Wapenaar et al., 2010). In other words, it turns a single physical geophone into a virtual source and receiver for imaging subsurface structures. The approximated Green's function is calculated by measuring the similarity between a data time series and a delayed version of itself in the function of time. Compared with cross-correlation, which is subject to two geophones, autocorrelation is a particular type of cross-correlation via a single geophone. The seismic interferometry methods can be used for several applications, such as monitoring geothermal and CCS sites (Tsuji et al., 2021), imaging the shallow (sedimentary basins and bedrocks) (Saygin et al., 2017; Chimoto and Yamanaka, 2019, 2020; Zhang,et al., 2021) and deep (crust-mantle boundary) structures and lithologies using; active sources of seismic waves as Man-made explosions and controlled sources as vibroseis or passive sources as natural earthquakes and ambient noise (Tibuleac and von Seggern, 2012; Gorbatov, et al., 2013; Kennett et al., 2015; Taylor et al., 2016; Oren and Nowack, 2017; Romero and Schimmel, 2018; Heath et al., 2018; Becker and Knapmeyer-Endrun, 2018; Mroczek and Tilmann, 2021). Seismic interferometry can extract a zero-offset reflection response beneath a seismic station based on autocorrelation analysis of the observed seismic signals (Claerbout, 1968; Wapenaar, 2004; Nakahara, 2006; Suemoto et al., 2020). Therefore, the seismic interferometry method was used to image high-resolution seismic profiles in chapter 3. Most previous studies performing seismic interferometry by autocorrelation used the codas of earthquakes or ambient noise data as input signals. Nevertheless, in chapter 3, we developed the autocorrelation process to exploit the blast mining's high frequency and amplitude signals as a source of seismic waves that boost the spatial resolution of the imaging to retrieve the body wave reflectivity of the shallow structures.

1.2 Research objectives

The seismic interferometry and seismic attributes of the reflected seismic wave components can be used for several imaging applications of the subsurface geological structures and lithologies, especially those associated with the earth resources (such as potential geothermal reservoirs as well as mine and hydrocarbon fields).

The objectives of this dissertation were as follows:

a) Utilization of the seismic attribute analyses to enhance the detection of the Clysmic fault-offsetting aggregate and the minor and significant cross faults that passed through the field. Also, enhancing the post-stacked seismic data for building a detailed 3D structural model of the Ras El Ush field that could map apparent geological discontinuities and structural traps would aid in developing the field and nearby, similar hydrocarbon fields in the Gulf of Suez (Egypt) (chapter 2).

b) Investigation of the feasibility of using buried mining blasts as a source of high frequency and amplitude seismic waves for the autocorrelation analysis. By extracting high-resolution images of the shallow subsurface geological and lithological features of the Hishikari minefield by the seismic interferometry based on the autocorrelation analysis of the blast mining P-wave reflectivity (chapter 3).

1.3 Chapter description

In this dissertation, there are two topics for the utilization of active seismic reflection data in the processing, imaging, and interpretation purposes using the reflected seismic body waves: building a 3D structural model by applying the seismic attributes and enhancing the reflections profiles that are attenuated and distorted due to the negative influence of the evaporites (salt layers) and severe faulting in the Ras El Ush field, Egypt (Chapter 2); using the blasting mining reflected signals to extract high-resolution images of the shallow geological structures and lithological boundaries by the seismic autocorrelation analysis (Chapter 3).

Chapter 2 describes using the post-stacked reflection seismic (P-wave) and well data comprising the check shot velocity data from active sources (air guns) to obtain and investigate detailed information about the structural fault orientation and dip of the Ras El Ush field (Egypt). In our case, the seismic energy was masked by the Pre-Miocene salt formation and attenuated by evaporite deposits in the upper Miocene, complicating the seismic interpretation process. The proper seismic attributes were used to get enhanced images and structural models to overcome the various complex structural features, such as evaporite deposits and high faulting zones that characterize this field and nearby areas of the Gulf of Suez active rift zone. Such complex geologic setting results in difficulties in terms of high-resolution seismic interpretation. Proper geophysical seismic imaging and interpretation of Ras El Ush field's associated structures and sedimentation can provide insights into the geological controls on hydrocarbon systems in the Gulf of Suez rift zone *(The contents of this chapter were published in Journal of African Earth Science (Imam T.S. et al., 2022)).*

Chapter 3 describes the potential of autocorrelation analysis for investigating shallow subsurface lithological imaging, including the ore deposits, using high-frequency blast mining signals. Autocorrelation analysis analyzed seismic data from the natural earthquake, ambient noise, and mine blasts to map P-wave reflection profiles at the Hishikari mine area (Japan). Seismic interferometry is commonly performed based on the autocorrelation of ambient noise or natural earthquake signals; here, the blasting in the mine was used instead since blast events include high-frequency signals that boost the spatial resolution of the imaging. To effectively extract P-wave reflections from seismic signals, including blast events, Gaussian smoothing, and spectral whitening were applied to remove source effects, and then the optimum frequency band was investigated. Auto-correlograms were obtained showing high-resolution seismic reflectors at shallow formation depths. A comparison with profiles obtained from ambient noise and earthquake data showed that blasting signals yielded highly spatially consistent reflections that would not be achievable with natural or ambient seismic sources. This study highlights the potential of using blast autocorrelation seismic analysis during short survey periods. By using single blast shot and dense seismic station spacings, higher resolution 3D reflection images of lithological interfaces were successfully achieved, possibly including ore veins *(The contents of this chapter were published in Geophysical Prospecting (Imam T.S. et al., 2022)).*

Chapter 4 summarizes the dissertation content and the main conclusions. By constructing 3D structural models based on the seismic and well logging data with the proper seismic attributes, advanced processing and interpretation techniques could resolve such complicated geological structures dominating the Gulf of Suez, Egypt, focusing on the potential productive layers. The active sources, such as the blast mining signals, can be an option for investigating and exploring other minefields that use the blasts to extract the potential minerals from hard rocks with a cost-effective method such as the seismic autocorrelation methods.

1.4 References

Basir, H.M., Javaherian, A. and Yaraki, M.T. (2013). ‘Multi-attribute ant-tracking and neural network for fault detection: A case study of an Iranian oilfield’. Journal of Geophysics and Engineering, 10(1), p.015009.

Becker, G. and Knapmeyer-Endrun, B. (2018). ‘Crustal thickness across the Trans-European Suture Zone from ambient noise autocorrelations’, Geophysical Journal International, 212(2). doi: 10.1093/gji/ggx485.

Brown, A.R. (2001). ‘Understanding seismic attributes’. Geophysics, 66(1), pp.47-48.

Chhun, C. and Tsuji, T. (2020). ‘ Pore pressure analysis for distinguishing earthquakes induced by CO2 injection from natural earthquakes’, Sustainability 12(22): 9723. doi: 10.3390/su12229723.

Chimoto, K. and Yamanaka, H. (2019). ‘S-Wave velocity structure exploration of sedimentary layers using seismic interferometry on strong motion records', Exploration Geophysics, 50(6). doi: 10.1080/08123985.2019.1654835.

Chimoto, K. and Yamanaka, H. (2020). 'Tuning S-wave velocity structure of deep sedimentary layers in the Shimousa region of the Kanto Basin, Japan, using autocorrelation of strong-motion records', Bulletin of the Seismological Society of America, 110(6), pp. 2882-2891. doi: 10.1785/0120200156.

Chopra, S. and Marfurt, K.J. (2007).' Volumetric curvature attributes add value to 3D seismic data interpretation'. The Leading Edge, 26(7), pp.856-867.

Claerbout (1968) 'Synthesis of a Layered Medium from its Acoustic Transmission Response'. Geophysics, 33(2), pp. 264–269.

Eng, C. and Tsuji, T. (2019). 'Influence of faults and slumping on hydrocarbon migration inferred from 3D seismic attributes: Sanriku-Oki forearc basin, northeast Japan'. Marine and Petroleum Geology, 99, pp.175-189.

Gorbatov, A., Saygin, E. and Kennett, B. L. N. (2013). 'Crustal properties from seismic station autocorrelograms', Geophysical Journal International, 192(2), pp. 861–870. doi: 10.1093/gji/ggs064.

Kennett, B. L. N., Saygin, E. and Salmon, M. (2015). 'Stacking autocorrelograms to map Moho depth with high spatial resolution in southeastern Australia', Geophysical Research Letters, 42(18). doi: 10.1002/2015GL065345.

Marfurt, K.J. and Alves, T.M. (2015). 'Pitfalls and limitations in seismic attribute interpretation of tectonic features'. Interpretation, 3(1), pp.SB5-SB15.

Misra, Achyuta Ayan, and Soumyajit Mukherjee, eds. (2018). 'Atlas of structural geological interpretation from seismic images'. John Wiley & Sons.

Mroczek, S. and Tilmann, F. (2021) 'Joint ambient noise autocorrelation and receiver function analysis of the Moho', Geophysical Journal International, 225(3). doi: 10.1093/gji/ggab065.

Nakahara, H. (2006) 'Theoretical background of retrieving Green's function by cross-correlation: one-dimensional case', Geophys. J. Int., 165, pp. 719–728.

Oren, C. and Nowack, R. L. (2017). 'Seismic body-wave interferometry using noise autocorrelations for crustal structure', Geophysical Journal International, 208(1). doi: 10.1093/gji/ggw394.

Pedersen, S.I., Randen, T., Sonneland, L. and Steen, Ø. (2002). 'Automatic fault extraction using artificial ants'. In SEG Technical Program Expanded Abstracts. Society of Exploration Geophysicists, pp. 512-515.

Romero, P. and Schimmel, M. (2018). 'Mapping the Basement of the Ebro Basin in Spain With Seismic Ambient Noise Autocorrelations', Journal of Geophysical Research: Solid Earth, 123(6). doi: 10.1029/2018JB015498.

Saygin, E., Cummins, P. R. and Lumley, D. (2017) 'Retrieval of the P wave reflectivity response from autocorrelation of seismic noise: Jakarta Basin, Indonesia', Geophysical Research Letters, 44(2). doi: 10.1002/2016GL071363.

Schuster, G. T., Yu, J., Sheng, J., & Rickett, J. (2004). 'Interferometric/daylight seismic imaging'. Geophysical Journal International, 157(2), pp. 838-852.

Schuster, G. T. (2009). ‘Seismic Interferometry’. Cambridge University Press. doi: 10.1017/CBO9780511581557.

Suemoto, Y., Ikeda, T., and Tsuji T. (2020). ‘Temporal variation and frequency dependence of seismic ambient noise on Mars from polarization analysis’, Geophysical Research Letters, 47(13), e2020GL087123, doi:10.1029/2020GL087123.

Taner, M. Turhan, Fulton Koehler, and R. E. Sheriff (1979). ‘Complex seismic trace analysis.’ Geophysics 44.6: pp. 1041-1063.

Taylor, G., Rost, S. and Houseman, G. (2016). ‘Crustal imaging across the North Anatolian Fault Zone from the autocorrelation of ambient seismic noise’, Geophysical Research Letters, 43(6). doi: 10.1002/2016GL067715.

Tibuleac, I. M. and von Seggern, D. (2012). ‘Crust-mantle boundary reflectors in Nevada from ambient seismic noise autocorrelations’, Geophysical Journal International, 189(1). doi: 10.1111/j.1365-246X.2011.05336.x.

Tsuji, T., Ikeda, T., Matsuura, R., Mukumoto, K., Hutapea, F. L., Kimura, T., Yamoka, K., and Shinohara M. (2021). ‘Continous monitoring system for safe managements of CO_2 storage and geothermal reservoirs’ Sci Rep 11, 19120. doi: 10.1038/s41598-021-97881-5.

Wapenaar, K. (2004). ‘Retrieving the Elastodynamic Green’s Function of an Arbitrary Inhomogeneous Medium by Cross Correlation’, Physical Review Letters, 93(25). doi: 10.1103/PhysRevLett.93.254301.

Wapenaar, K., and J. Fokkema (2006). ‘Green’s function representations for seismic interferometry’, Geophysics,71, pp. SI33–SI46.

Wapenaar, K., and Neut, J. (2010). "A representation for Green’s function retrieval by multidimensional deconvolution." The Journal of the Acoustical Society of America 128.6, pp. EL366-EL371.

Zhang, Y., Li, Y. E. and Ku, T. (2021) ‘Soil/rock interface profiling using a new passive seismic survey: Autocorrelation seismic interferometry’, Tunnelling and Underground Space Technology, 115, p. 104045. doi: 10.1016/j.tust.2021.104045.

Chapter 2

Mapping the geological structures in the Ras El Ush field (Gulf of Suez, Egypt), based on seismic interpretation and 3D modeling techniques

2.1 Introduction

In the Gulf of Suez (Egypt), hydrocarbon exploration has been conducted for over 50 years, and several significant oil fields have been discovered, such as Belayim (2.3 billion STB), Morgan (more than one billion STB), and July and October fields (more than 700 MSTB) (Awni et al.,1990). The Gulf of Suez represents the north-western extension of the Red Sea rift regime, bordering the western coast of the Sinai Peninsula and eastern desert of Egypt (Figure 2.1). The Cenozoic rift extends with 300 km long and about 80 km wide. The area of sedimentary basin is 30,000 km2 with average sedimentary cover around 6 km. Rifting along the Gulf of Suez was initiated during the early stages of separation of the Arabian plate from the African plate. In general terms, the structural elements of the Gulf of Suez are sophisticated, and many attempts were done to explore this area. It comprises a large number of kilometer-scale tilted fault blocks enclosed by main normal faults of the NW-SE orientation (Makky et al., 2010; Abd-Allah et al., 2019; Abuzied et al., 2020).

Based on trends of the tilted fault blocks, the Gulf of Suez consists of three mega-half grabens at the north, center, and south of the Gulf of Suez Basin. These are defined as Darag Basin with dominant dip direction to SW, Belayim Province with a main dip direction to the NE; and Amal-Zeit Province (the study area) with SW dip direction, respectively. Moreover, two accommodation zones connect these three mega-half-grabens, namely Morgan accommodation zone, linking between central and southern half-graben, and Galala-Zenima (Zaafarana) accommodation zone, linking between the central and northern half-graben. These zones have good potentialities for hydrocarbon accumulations (Younes and McClay, 2002; Othman, 2021). The Gulf of Suez rift basin initiated across four major fault trends during the Upper Oligocene-

Lower Miocene. These fault trends are known as the Clysmic trend in the NW-SE direction (Patton et al., 1994; Abd El-Naby et al., 2009; Othman and Fathy, 2015) the North and the NW oblique faults running to the Clysmic trend, and the cross-faults trend with near-orthogonal orientations to the Clysmic trend.

The Ras El Ush (REU) field (Figure 2.1) was discovered in the petroliferous Egyptian Gulf of Suez in 1995. This complex, fault-bounded, structural trap system was first suggested by outcrop geology and subsequently delineated from an aeromagnetic anomaly that corresponds to a regional basement high (Younes and McClay, 2002). Shortly after its discovery, the offshore REU field was delineated with five deviated wells drilled from onshore with deviations and directions extend to greater depths of the offshore parts of the field (Badri et al., 1999). These wells were adjusted in that orientation to be productively effective with the reservoirs occur in rotated fault blocks bounded by normal and strike-slip cross faults. Hydrocarbon accumulations may be affected by persistent rotation of oblique fault blocks in the southern zone of the Suez rift and the northwestern Red Sea, which might led to a lowering of the dip angles of the main-bounding faults, where they got locked and broke down by second episode of faults (Moustafa and Khalil, 2020). Seismic 2D imaging in the Gulf of Suez, in general, and the REU field area particularly is hampered by the thick Miocene South Gharib and Belayim formations. These formations consist of a thick sequence of evaporites interbedded with thin clastics, hence generating severe seismic reflection multiples that mask the reflections from the underlying reservoirs (Badri et al., 1999). The study area is located in the Gebel El-Zeit area in the southwestern region of the Gulf of Suez (Figure 2.1). Ras El Ush oil field is situated 80 km north of Hurghada in the offshore transition marine zone 1.5 km east of the saddle between the main Gebel El Zeit and little Zeit (Bedri et al., 1999).

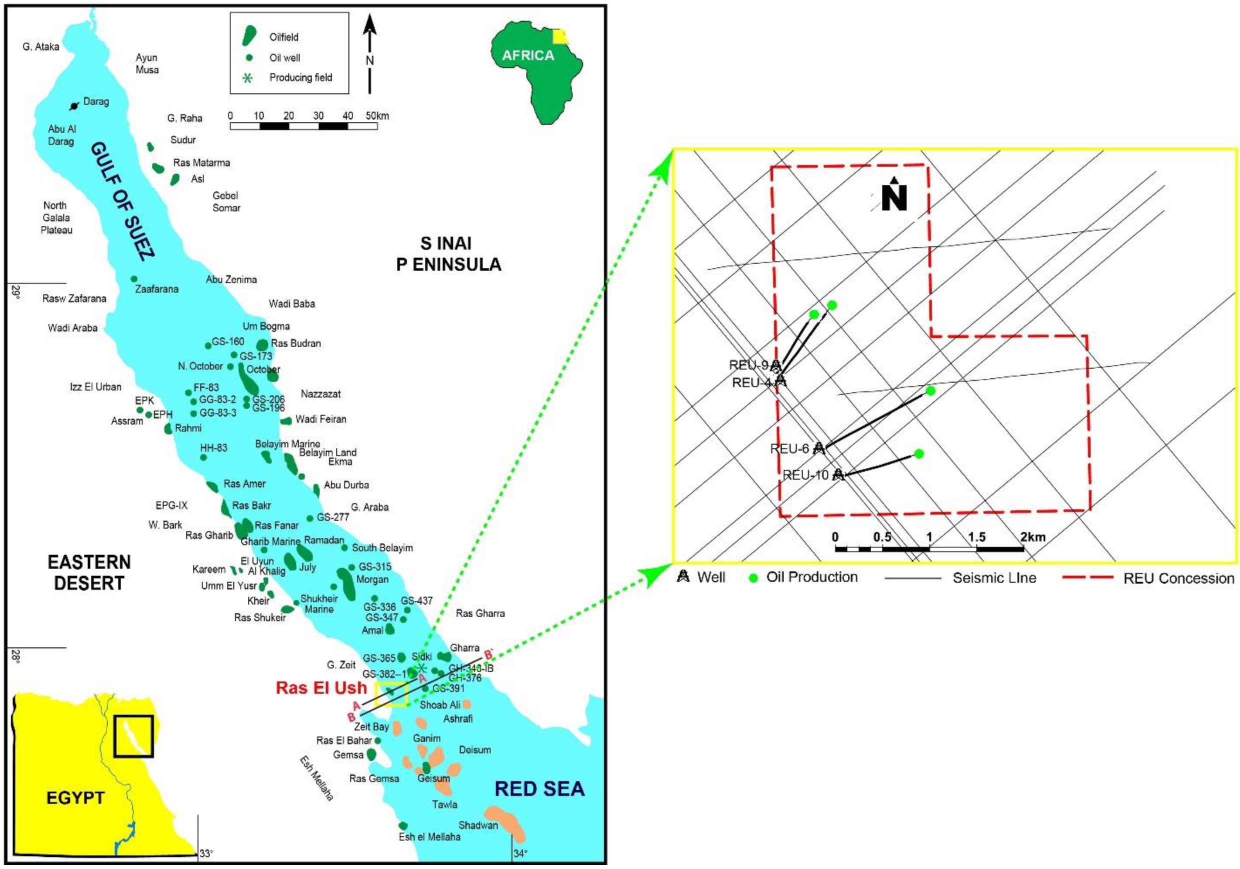

Figure 2.1: Location of Ras El Ush field showing the base map with the distribution of seismic lines and well locations of the Ras El Ush study area., Gulf of Suez, Egypt.

The main target of the present study is to use seismic reflection data, in the light of the geological and stratigraphic information, to achieve the following: (1) enhance the seismic data to obtain clearer seismic images and subsequently better seismic interpretation aided with applying seismic attributes , (2) define and recognize the possible subsurface structures deformed alterations and influence of the tectonic framework of the area, that may facilitate locating undiscovered hydrocarbon prospects, (3) construct a detailed structural model for the REU area.

Almost entirely in the REU area, the seismic wave capacity was obscured by the Pre-Miocene salt strata in this field. Hence, seismic interpretation of the reflected horizons deeper than Pre-Miocene salt is difficult and uncertain (Bedri et al., 1999). In this study, the seismic data (2D and 3D) with the well and velocity data were integrated to construct a structural model using the fault pattern recognitions from the seismic data. The model would help in optimizing the exploratory and development plans of the field by creating more precise images of the sedimentary structures especially fault data and their accurate locations. The significance of using seismic attributes and modeling techniques were also referred as an effective integrated way to avert the dry holes and drilling risks (Abdel-Fattah et al., 2017) using Ras El Ush field as an example for this approach. Certainly, these kinds of analyses are necessary to describe and appraise the hydrocarbon reservoir and related complex structures and raise the gaining rate of the upcoming hydrocarbon investigation and enhanced recovery plans in the REU field, Gulf of Suez, Egypt.

2.2 Geological setting

The Gulf of Suez began as a depositional region during the Early Paleozoic period (Said 1962; 1990). Unlike the Red Sea and the Gulf of Aqaba, which were formed by upwarping of the Nubian-Arabian shield followed by rifting, transform faulting, and eventual break-apart (Friedman, 1980; McClay and Khalil, 1998; Bosworth and McClay, 2001), the Gulf of Suez was formed by tensional movement and subsidence along NW-SE trending normal faults, most likely before Devonian time (Figure 2.2). During the early stages of the East African rifting in the Oligocene-Miocene, the Gulf of Suez, as a crustal weakness, followed suit and changed to its current shape

(McClay and Khalil, 1998; Bosworth and McClay, 2001). The Gulf of Suez is an intensely faulted area, and Figure 2.3 shows a typical cross-section. Fractures generated by tectonic processes such as movements of the Nubian, Arabian, and Sinai plates, as well as the consequent East African Rift system, have shaped the current structure of the Gulf of Suez (Said, 1990; Abd-Allah et al., 2019; Abdel-Fattah et al., 2021a). The NNW-SSE Erythrean trend, the N-S East African Rift trend, the NNW-SSE Aqaba trend and the E-W Tethyan trend are responsible for the development of the Gulf of Suez, as seen in Figure 2.3.

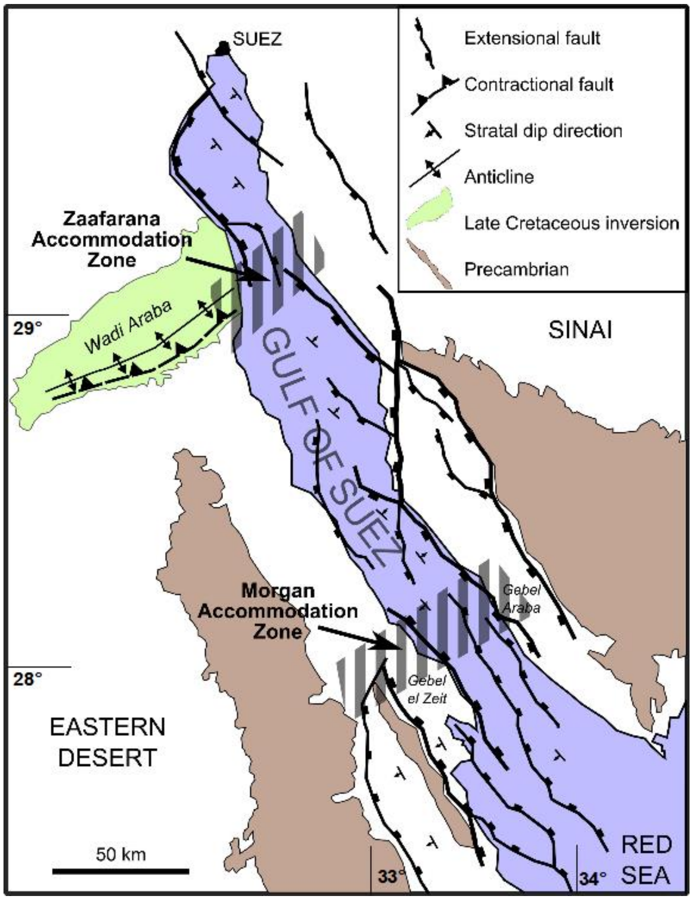

Figure 2.2: Tectonic regime of the Red Sea and Gulf of Suez, Egypt (Friedman, 1980; Khalil, 1998; Bosworth and McClay, 2001).

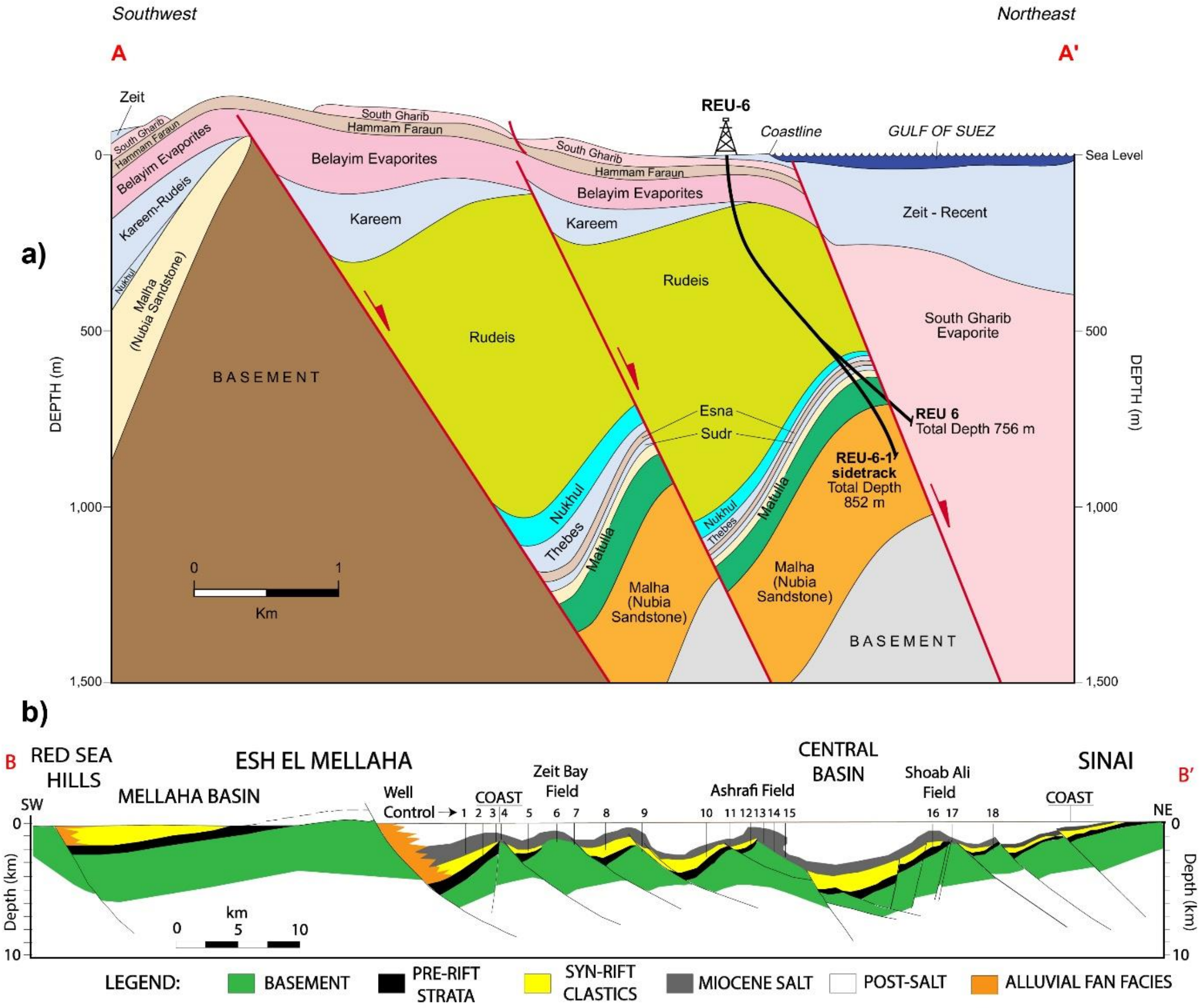

Figure 2.3: a) Geological cross-section showing the structural and stratigraphic complexity across the Ras El Ush field, Gulf of Suez, Egypt (modified after Badri et al., 1999) (see A-A` in Figure 2.1). b) Cross-section across the Zeit basin in the southern Gulf of Suez, illustrating its characteristic structural setting (Bosworth et al., 2005) (see B-B` in Figure 2.1).

The Erythrean trend controls to a large extent the normal faults flanking and running parallel to the present Gulf of Suez. The Aqaba trend is thought to have affected the Gulf with slight rotation of fault blocks (Younes and McClay, 2002). The Tethys trend is limited to the extreme north and is manifested by gently folding of pre-Pliocene formations. Most likely the Gulf of Suez area was a zone of crustal weakness since Precambrian times (Meshrif et al., 1976). The East African trend gives the coastline a sort of zigzag appearance, more pronounced in the Red Sea than in the Gulf area (Patton et al., 1994; Abd El-Naby et al., 2009). The combined effect of these tectonic events led to intense structuring and break-up into an enormous number of fault blocks composed of formations ranging from Precambrian to Eocene. This faulting must have occurred towards the end of erosional pre-Miocene period that produced the marked unconformity surface between the Lower Miocene and the pre-Miocene (Abd-Allah et al., 2019; Abdel-Fattah et al., 2021a).

Figure 2.4 depicts the Gulf of Suez's generalized stratigraphy, which is divided into three depositional stages (EGPC, 1996; Badri et al., 1999). The first consists of the formations that range in age from the Devonian to the Eocene. The Nubia sandstone is part of these formations, which are important as reservoir rocks and to a lesser extent as source rocks. The Lower Miocene is the second phase, and it is distinguished by its overall great features as a source, reservoir, and seal rock. In essence, the third phase, which spans the Upper Middle Miocene and Pliocene epochs, brings the Suez graben's depositional history to a close (Said, 1990).

The Upper Cretaceous sequences are overlying conformably to non-conformably by Cenomanian sediments (EGPC, 1996). The conformable contact with Cenomanian is gradational and is hardly to be detected while the non-conformable section occurs with sharp marine contacts of Cenomanian facies. The Raha, Wata and Matulla formations were grouped as Nezzazat Group. Nubia and Matulla sandstones are the major productive horizons within the pre-rift sediments (Alsharhan, 2003).

The Lower Miocene, also known as the Gharandal Group, and the Middle Miocene, also known as the Ras Malaab or Evaporite Group, make up the Gulf of Suez's Miocene sequence (Darwish and El Araby, 1993). The lower group has the richest source rocks in combination with outstanding reservoir deposits under the most ideal structural conditions, while the upper group provides the most efficient seal for both Miocene and pre-Miocene reservoirs (Farhoud, 2009). The Gharandal Group is subdivided into three stragraphic units that can be seen across virtually the whole graben area. The Nukhul Formation, the bottom unit, contains carbonates and high-energy reefal build-ups on pre-Miocene topographic highs, as well as sands and shales in the lows between fault blocks and on fault block named surfaces (Badri et al., 1999; Alsharhan, 2003). The Rudeis Formation, which lies above the Nukhul, is primarily made up of extremely fossiliferous shales and marls known as the Globigerina Marls, as well as sandstones. The Kareem Formation is primarily shaly, with sandstones interspersed throughout. Shales from the Rudeis and Kareem formations are thought to be the Gulf of Suez's principal source rocks. The interbedded sandstones provide good reservoirs, with porosities ranging from 10% to 20% (EGPC, 1996).

The massive development of evaporitic series, particularly in the graben zones of the Gulf of Suez and the Red Sea, characterizes the Middle Miocene. Along the graben's borders, thick anhydritic and calcareous phases evolved, giving way to thick salt basin ward. Near the confluence of the Red Sea and the Gulf of Suez, the salt is the thickest. Gypsum, anhydrite, and carbonates eventually push rock salt to the north in the northern Gulf of Suez (Said, 1990; EGPC, 1996; Badri et al., 1999).

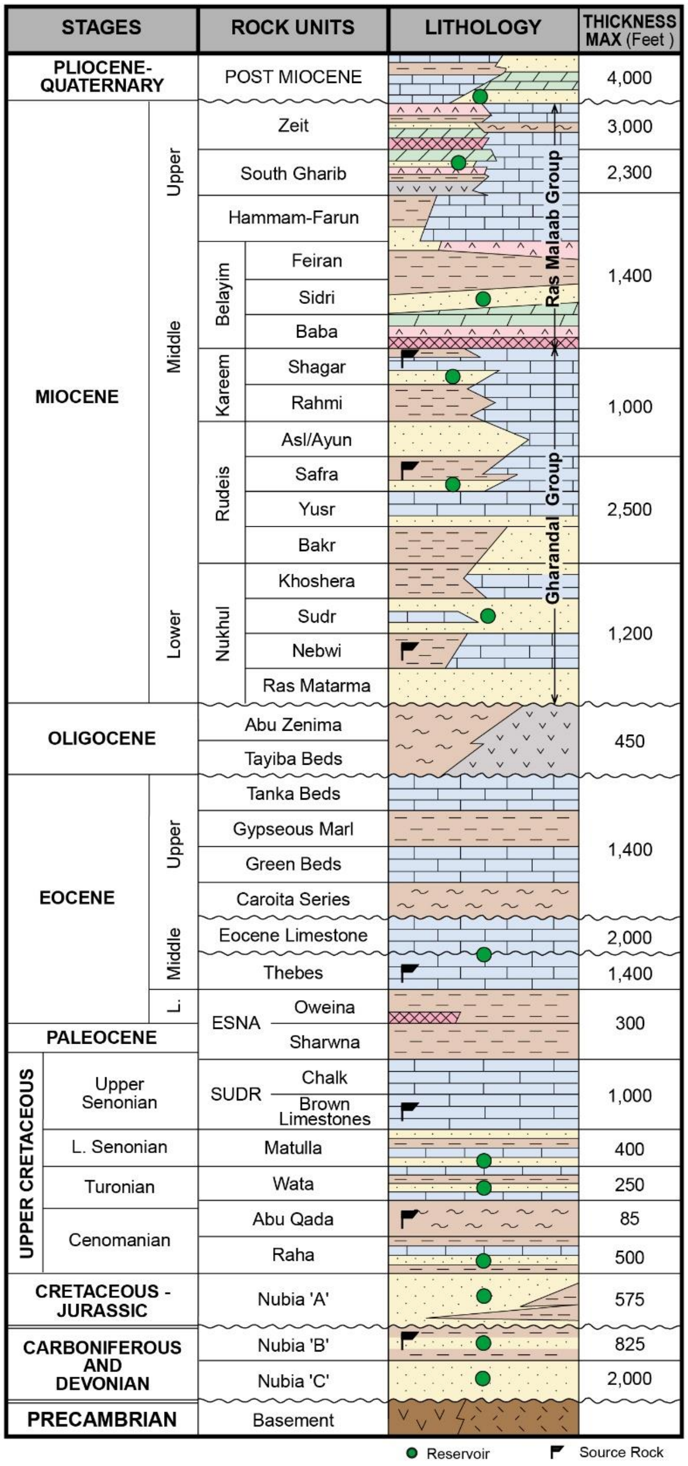

Figure 2.4: Stratigraphy and petroleum systems of the Gulf of Suez, Egypt (Badri, 1999; EGPC, 1996).

2.3 Data and applied methodology

The available data include four composite log data provided by Egyptian General Petroleum Corporation (EGPC) and Gebel El Zeit Oil Company (PetroZeit) for the wells (REU-4, REU-6, REU-9, and REU-10). The data also include the encountered well tops, well surveys or paths, well logging data (gamma-ray, resistivity, density, sonic, and neutron logs for specific intervals) and check shots. The four wells were drilled and extended to the offshore (Figure 2.1). The seismic data comprise twenty 2D seismic lines (ten inlines in the NE trend, and eight crosslines in the NW trend, and two in the EW trend). Figure 2.1 shows the base map and the exact locations of seismic profiles and wells. Petrel TM software was used for the interpretation of the seismic, well data, and generated maps. We succeed in extracting the complex structural and stratigraphic information from local to reservoir scale.

2.3.1. Seismic attributes

Identifying and mapping fault structures often help to determine the size, geometry, and level of compartmentalization of reservoirs (Abdel-Fattah and Alrefaee, 2014). When faults are mapped on seismic profiles, they can provide valuable information about how fluids flow in the reservoir and the connectivity of the fluid within reservoirs (Neves et al., 2004; Chopra et al., 2007). However, manual picking of fault planes for structural interpretation is tedious for low quality (much attenuated) seismic profiles in three dimensions. Therefore, utilizing the seismic attributes is useful to visualize the trends of hard-to-see or invisible faults on a conventional seismic profile (Tsuji et al., 2005). Information from different seismic attributes is used to form fault geometry, and this information can generally be used to optimize well locations (Santosh et al. 2013; Abdel-Fattah et al., 2020).

2.4 Seismic interpretation methods

By using the seismic reflection method, we can locate and map subsurface structural features as anticlines, faults, salt domes, and reefs. Many of these geologic structures have a strong likelihood of being linked to oil and gas accumulation (Abdel-Fattah et al., 2021b). As a result of mapping these characteristics, we can locate structures where potential fluids may be held, as well as faults that could obstruct fluid movement in a producing field. Consequently, the chance of drilling a dry exploratory well can be mitigated. Another useful benefit of using seismic interpretation is monitoring the possible hydrocarbon flow pathways through the reservoir during production. Therefore, for subsurface mapping, the seismic data interpretation approach is perhaps the most employed geophysical technique for hydrocarbon structural trap mapping (Fadul et al., 2020; Abdel-Fattah et al., 2020; Abdel-Fattah et al., 2021b). Applied seismic interpretation techniques in this study, included analysis of velocity, reflectivity, and detecting the subsurface structural configuration, and depth maps construction for tops of middle and upper Miocene formations in the Ras El Ush field, Gulf of Suez, Egypt.

2.4.1 Velocity analysis

Seismic velocity provides essential information to characterize or quantify the geological structures. We used seismic RMS and stacked velocity derived from seismic and sonic log data as the main approaches to determine the velocity in the studied field. In the present work the interval velocity (Vi), and the one-way time (T) are computed and displayed in the form of depth-time-velocity relations (Figure 2.5), the time depth curve could then be obtained. The interval seismic velocity depends largely on several geologic conditions such as lithology, stratigraphy, pore pressure, and gas saturation (Tsuji et al., 2014; Chhun et al., 2018). We performed this velocity study in the Ras El Ush field for the four wells REU-4, REU-6, REU-9, and REU-10 and their distribution maps over the studied area.

2.4.2 Well-seismic tie

The connection between lithology and seismic reflections is provided by the well control. Implementing the correlation between seismic reflections and lithologic strata is one of the first stages in analyzing a seismic dataset. Integrating well data (in-depth) with seismic data (in-time) facilitates in the identification of seismic occurrences (reflections) that corresponds to geological formations (Badley, 1985; Abdel-Fattah et al., 2015). In addition, check shots survey results helped in enhancing the well and seismic tying. As a result, because the frequency content of downhole data is much higher than that of surface seismic recordings, especially at deeper depths, these data give the optimum velocity control (Paulsson et al., 2001). Well velocity surveys were used to enhance the precision of time-depth conversions (Figure 2.5).

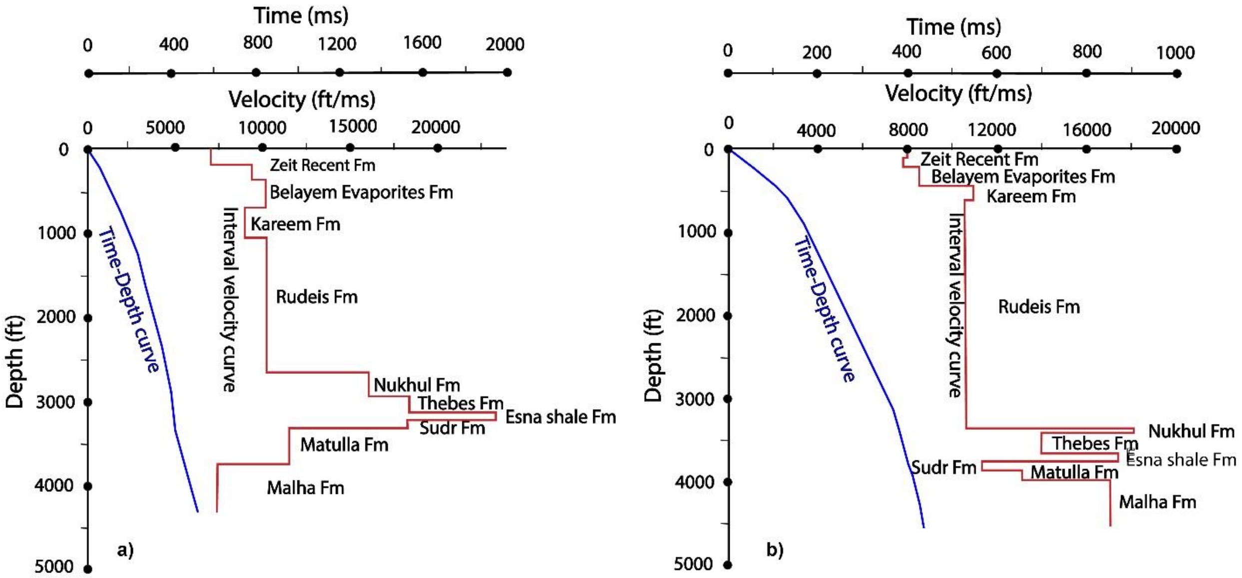

Figure 2.5: The depth-velocity-time relation for the wells (a) REU 4 (b) REU 6. This relation includes one-way time, and interval velocity versus depth of the encountered formations in Ras El Ush, Gebel El Zeit area, south Gulf of Suez.

2.4.3 Horizon and fault interpretation

The top horizons of the Rudeis, Nukhul, and Matulla formations were chosen as structural elements of the grid, to regulate reservoir geometry in the study area. Because all reflections at sequence boundaries and those exhibiting unique geological features should be chosen and interpreted throughout the grid if the area is relatively obscure. Other supplementary reflectors were picked as a framework limitation throughout the interpretation process to mitigate errors (Badley, 1985).

In this study, seismic phantom horizon interpretation method was applied, which is a horizon on a reflection profile obtained by averaging the dips of the reflections within a band. Hence, the dip's trend is indicated, although it does not necessarily match with an actual boundary plane (Harding, 1985). Moving a selected horizon from its original location to a constant is one approach, which is beneficial for showing seismic facies in an interval defined by parallel or subparallel horizons with no lateral thickness variation. The purpose is to properly interpolate between the two selected horizons, which is effective for visualizing a variable-thickness interval bordered between two disconformable stratigraphic surfaces. We incorporate a range of horizontal and vertical slicing along in-lines, crosslines, and arbitrary lines to evaluate the interpretation quality and to mitigate the flaws in defining the horizons (Tsuji et al., 2013; Abdel-Fattah et al., 2020). Figure 2.6 shows how the horizon and fault picking process were done in the seismic section to achieve our final interpretation, evaporite deposits negatively influenced the seismic reflection data to be below the seismic resolution.

The following are the most common evidence of faulting on seismic reflection cross sections: (Abdel-Fattah et al., 2015; Fadul et al., 2020): (1) Reflection discontinuities that follow a roughly linear trend. (2) Discrepancies in dip that are not stratigraphical dependent. (3) diffraction patterns, especially those with vertices that match up with local faulting regularly. (4) Reflections are distorted or dissipate beneath possible fault lines. Our approach was to interpret the faults impacting the zone of interest to elucidate the area's geological and tectonic evolution and anticipate what style of hydrocarbon traps may be present in the area, as the field research area is highly faulted.

We created structural TWT maps to the tops of the Rudeis, Nukhul, and Matulla formations, the picked time values and locations of fault segments are marked on the constructed maps. Also, to generate the structural depth maps, we utilized the time and velocity models to convert reflection times to depths.

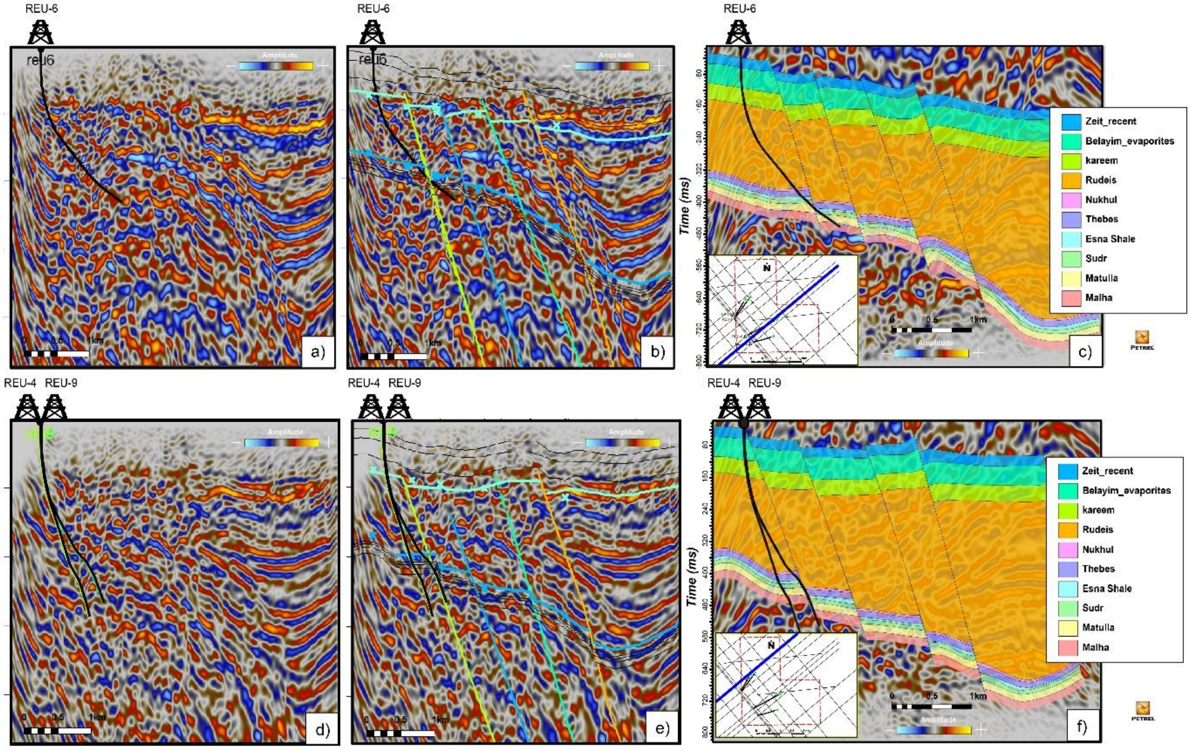

Figure 2.6: Examples of seismic interpretation observed by horizon and fault picking (a) and (b) are before and after interpretation for the seismic line (Inline 1293), (d), and (e) panels are another example for the line (Inline 1362) interpretation. Generated geo-seismic sections show the layers with their expected thickness in corresponding right panels (c) and (f).

2.5 3D structural model construction

The extent of the modeling process is influenced by the quality of the dataset together with the geological, geophysical, and petrophysical interpretations made in the field. A realistic high-resolution geological model of the reservoir structure and stratigraphy is necessary for hydrocarbon identification and recovery (Abdel-Fattah et al., 2018; Khan and Abdelmaksoud, 2020; Abdullah et al., 2021). The Ras El Ush structural model was constructed using modeling software (Petrel TM) that is simply integrated with geophysical and reservoir engineering tools. Structural modeling is the first step in constructing 3D models, so we performed three modeling processes: fault modeling, pillar gridding, and geological horizons extraction.

We defined the fault in the geological model and generated fault planes in the 3D grid model (Figure 2.7) by synthesizing "Key Pillars". A fault architecture and transmitted fault sticks have been generated based on interpreted seismic lines. The length, shape, azimuth, and dip specify the fault plane through "Key Pillars". Making an accurate and consistent Ras El Ush structural model demands fault modeling and editing of Key Pillars (Figure 2.8). The pillar gridding process generates the structural model, the grid provides a framework for the modeling. The Ras El Ush field employed a grid that was 100 m x 100 m x 0.5 m in size (Figure 2.8a). To construct the structural and property models, and to define the reservoir geometry, all the data was loaded in a 3D grid. (Abdel-Fattah, 2010; Abdel-Fattah et al., 2018). Pillar Gridding produces a group of pillars that run parallel and within the faults.

The stratigraphic horizons (Rudeis, Nukhul, and Matulla) were entered into the grid, then estimate horizon locations that reveal fault displacements across single faults. The later phase in structural modeling is layering, or the formation of stratigraphic horizons. We added constructed grid and the faults described in previous phases, consequently, we inserted the interpreted stratigraphic horizons in the Ras El Ush model (Figure 2.8b). Fault modeling, pillar gridding, and vertical layering are all incorporated into a single data model (3D grid). This structural model is the backbone of the research area by which all subsequent property and dynamic models could be built.

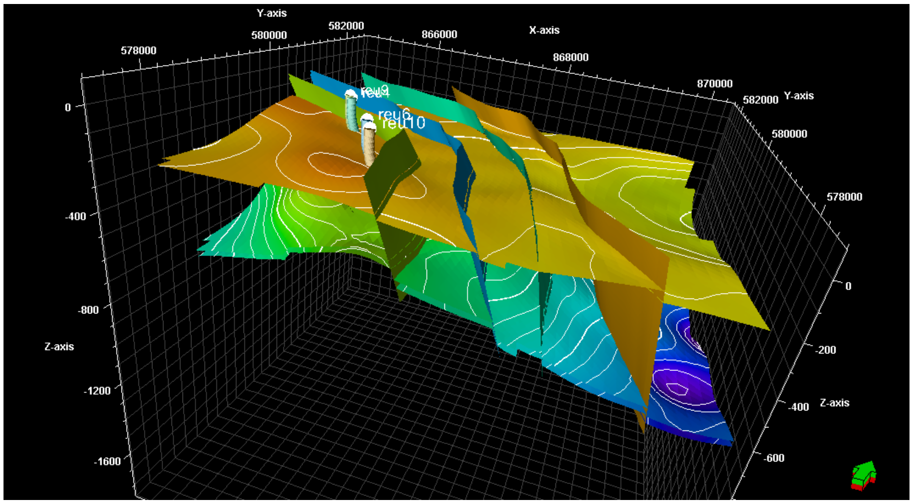

Figure 2.7: The horizons tops (Rudeis, Nukhul, and Matulla) and fault model displayed in a 3D window after Key Pillar operations.

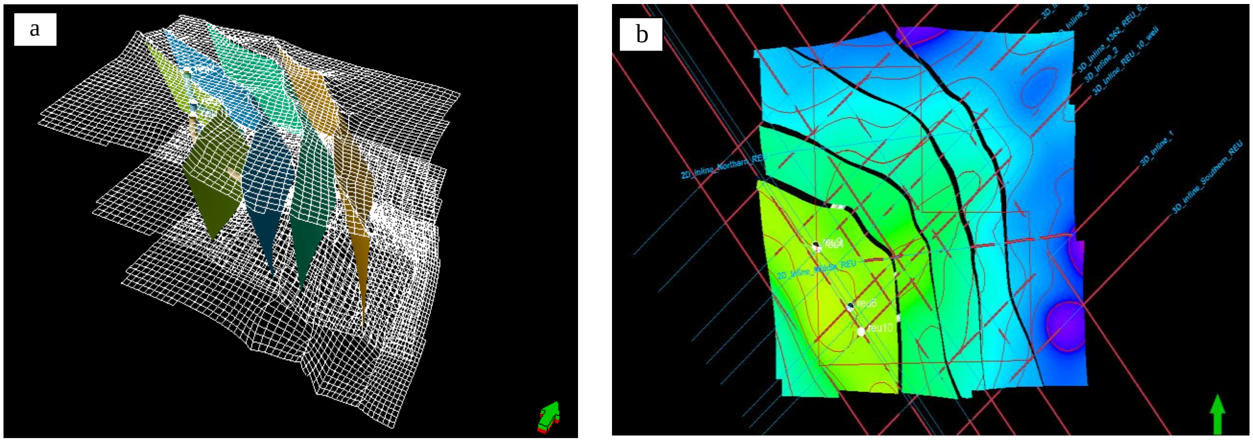

Figure 2.8: (a) Three skeletal grids (Top, Mid, and Base) with fault junctions running through the grid, displaying the pillars that link grid cells. (b) In 2D windows, all fault blocks and the skeleton are illustrated.

2.6 Results

2.6.1 Seismic interpretation

Salt layer and complex fault structure have magnified noise and artifacts in the Ras El Ush seismic data (Figure 2.9a). Some faults are masked while the salt formation generates distortions in seismic images. Seismic attribute analyses in this study includes two steps, the first step was conditioning and structural smoothing of the seismic data to reduce the noise in the data (Figure 2.9b and 2.9c). The second step was to enhance the seismic data spatial discontinuities (fault attribute generation and edge detection) (Figure 2.9d). These procedures significantly improve the fault attributes by removing the noise and the remains of non-faulting events. Seismic attributes are often sensitive to the noise present in seismic data. Therefore, we often use a spatial filter (structural smoothing) to remove the noise while retaining the geometrical details (Basir et al., 2013; Brown; 2001; Pedersen, 2002; Eng and Tsuji, 2019). In structural smoothing, the Gaussian weighted filter method was offered to attenuate the noise and optimize the discontinuities in the seismic volume (Acuña-Uribe et al., 2021).

We also used the structural smoothing attribute to highlight flat spots within the seismic volume, by conducting the smoothing operation without dip guiding (Marfurt and Alves, 2015). The results could be recovered to the original data or used as a smooth interpretation of regional surfaces. Structural smoothing helped in illustrating the reflectivity in the present study area (Figure 2.9). Using the post-stack seismic attributes and interpretation helped to reveal the structural architecture of the Ras El Ush field. At the Ras El-Ush oil field, the use of seismic attributes obtained from 3D seismic data showed subsurface structural features of a buried volume of rock. The resolution of standard seismic amplitude data would generally be sufficient to resolve such structural features. Figures 2.9c and 2.9d show a higher resolution post-stack seismic image after applying seismic attributes that better visualize the discontinuities so that faults could be seen even in complex geologic sequences. Integration of well data with the seismic attribute volumes increased the reliability and accuracy of our interpretation. The results of the seismic interpretation after using seismic attributes enhancement methods showed remarkably improved horizontal and vertical resolution and provided higher certainty in mapping faults and discontinuities.

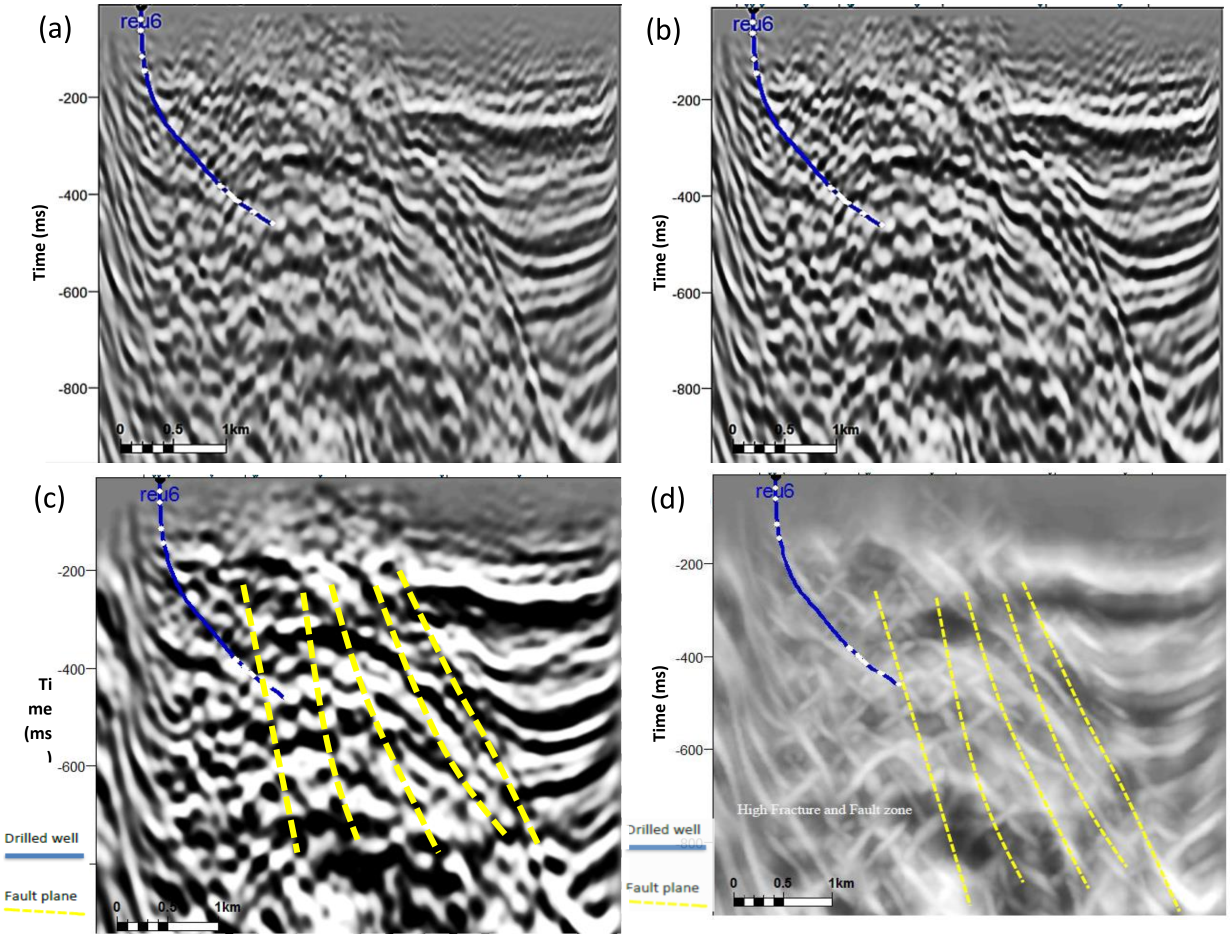

Figure 2.9: a) Original seismic data of the Ras El-Ush field (Gulf of Suez, Egypt), b) First iteration of seismic conditioning and structural smoothing, c) Second iteration of seismic conditioning and structural smoothing, d) 3D edge enhancement attribute shows the high fracture and fault zone.

In the study area, the average velocity map down to a studied horizon indicates the lateral velocity distribution through the geological formations overlying that horizon. The average and interval velocity with their lateral and vertical distributions down to tops of Rudeis, Nukhul, and Matulla formations have been determined from P-wave velocity data of the available wells using depth-velocity relations and plotted at the study wells (Figure 2.10). Three average velocity distribution maps have been constructed for studying the Miocene (Rudeis and Nukhul) and pre-Miocene (Matulla) sections (Figures 2.10a, 2.10b and 2.10c, respectively). The generated velocity maps highlighted the significant velocity changes vertically because of the overburden and depth. Meanwhile, the velocity changes laterally depending on the minor and major lithologic variations of the subsurface sedimentary section of Pre-Miocene and Miocene. Therefore, this indicates great facies changes vertically and horizontally at the arbitrarily chosen horizons.

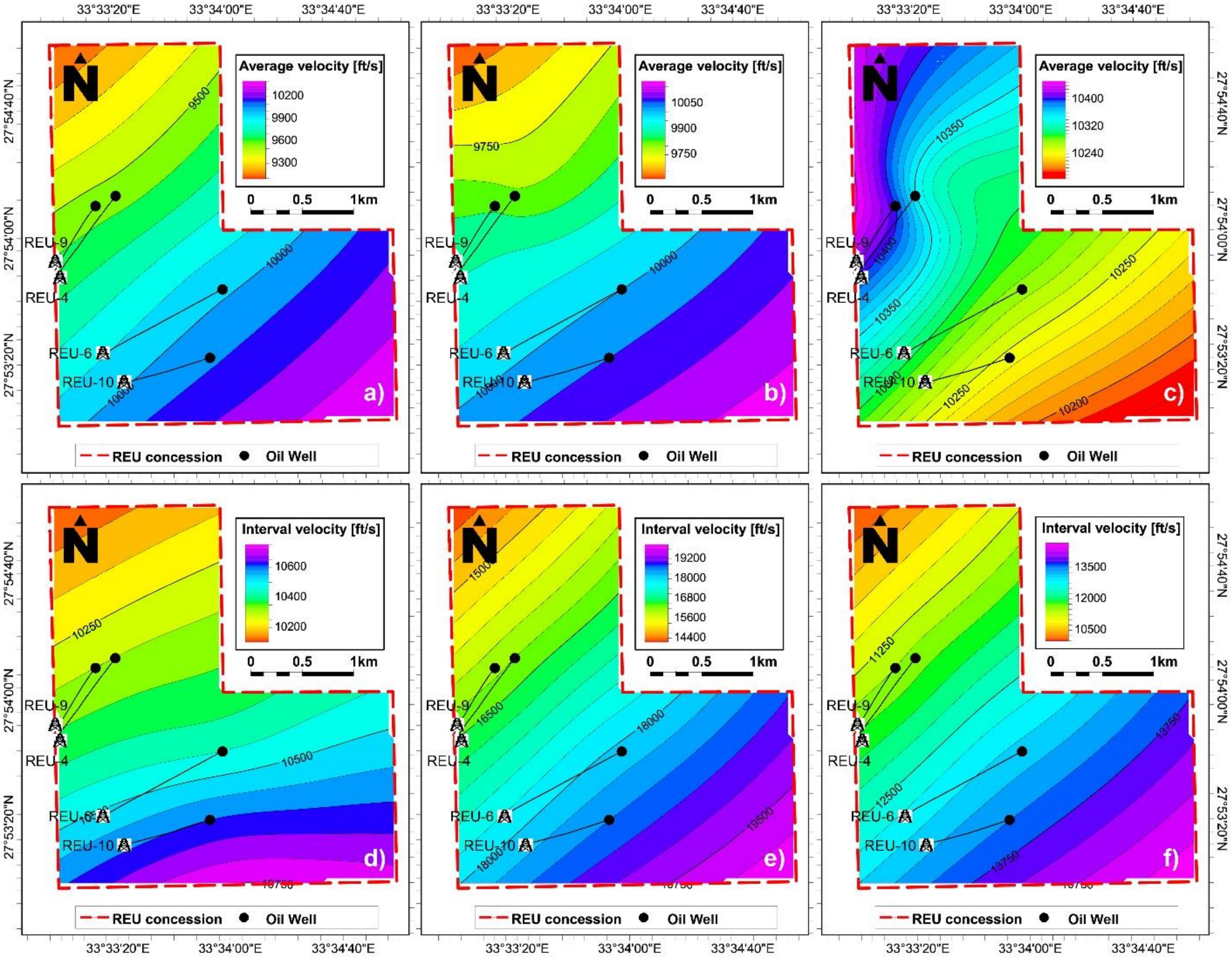

Figure 2.10: Distribution of average velocities of Rudeis, Nukhul, and Matulla horizons represented by (a), (b), and (c), respectively. While the distribution of interval velocities of Rudeis, Nukhul, and Matulla horizons represented by (d), (e), and (f), respectively.

Two-way time reflection contour maps for the early Miocene reservoir (represented by Rudeis and Nukhul) vary between 80 milliseconds to 280 milliseconds two-way travel time (Figure 2.11). When converted to depth using the velocity model the depth to the top of Miocene reservoir was ranging from 270 to 1500 ft, the deepest portion was in the east. The horizons are tilted towards the southeast direction. Low-relief regions are found in the eastern and south-eastern sections of the studied area, while high-relief areas are found in the western part, which is inclined slightly to the south (Figure 2.11).

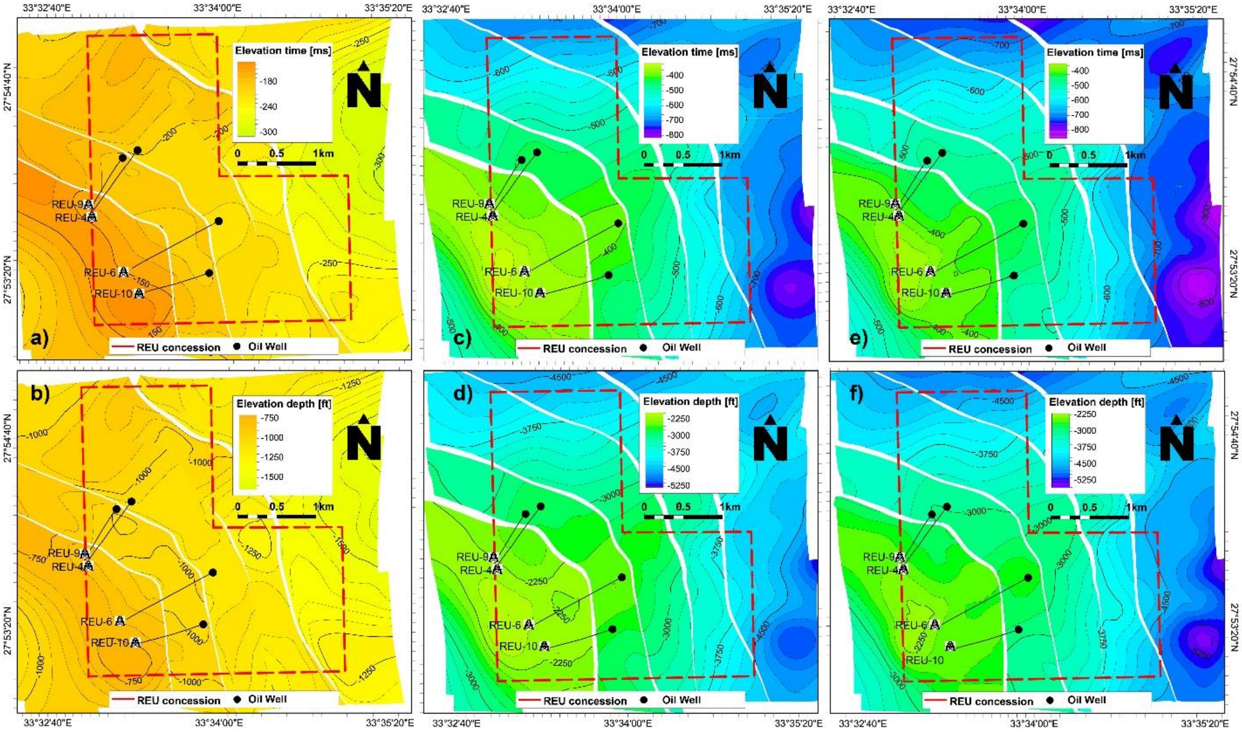

Figure 2.11: Isochronous (two-way time) and depth structure maps of Rudeis (a and b), Nukhul (c and d), and Matulla (e and f) formations, showing the depth conversion for these main horizons in Ras El Ush area, Gulf of Suez, Egypt.

2.6.2 3D structural Model

In the 3D structural model of Ras El Ush field, all faults are described as segmentation boundaries. A segment is prescribed as a region bounded by faults in all directions if the faults are connected appropriately. The REU model has five fault segments (fault blocks). Figure 2.8 shows a skeleton grid color-coded for each segment and it indicates how connected faults and boundaries limit the segments, and the relevant segments are colored specifically. The spatial and temporal distribution of Ras El Ush field zones, as well as their thickness variations, can be seen in structural cross-sections produced from the 3D structural model in various directions across the research area. The Ras El Ush model is split into fault sections based on the structural components in the study area (Figure 2.12).

Several Clysmic faults cut across the research area, revealing a regime of normal faults. These faults run parallel to the Gulf of Suez with NNW-SSE and NW-SE trends, controlling the morphology of the study area. The downthrow of most of these faults are to the northeast and southeast. All the faults identified in the seismic sections are extensional normal faults that formed grabens and half grabens. The length of these fault planes ranges from more than 6 kilometers to a few hundred meters. Their vertical extension (on a time scale) ranges from around 200 milliseconds for minor faults to 2500 milliseconds for major faults (Figure 2.6). The resulted 3D representation of the structural Ras El Ush model shows depths and fault planes. Several cross-sections in the N-S and E-W directions have been shown in addition to the 3D structure model to illustrate the basic geological setting in the research area (Figure 2.12). The Rudeis, Nukhul, and Matulla horizons’ 3D structural models show the same arrangement and structural components. This agreement suggests that the Rudeis and Nukhul, as well as the Matulla horizons, were conformably formed in the same basin and were exposed to similar tectonic stresses following their deposition.

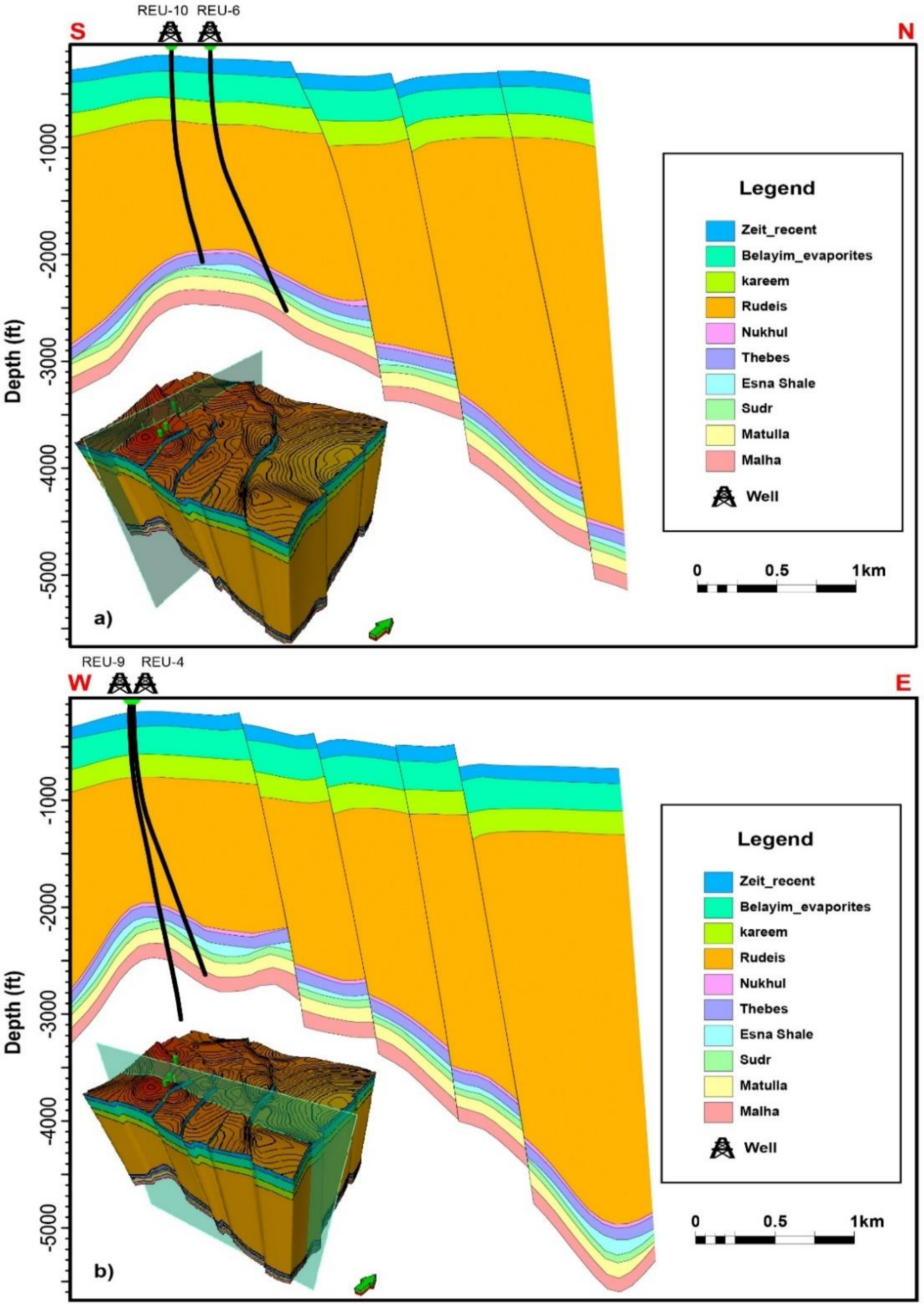

Figure 2.12: 3D structural model and two cross-sections in N-S direction (a) and in W-E direction (b) showing lateral and vertical extension of Rudeis, Nukhul, and Matulla formations and their thickness variations, including the faults and folds of Ras El Ush succession, Gulf of Suez, Egypt.

2.7 Discussion

The Ras El Ush field (Gulf of Suez, Egypt) contains the main elements of hydrocarbon systems of shale source rock, sandstone reservoir formations, and the seal evaporite salt layers at several levels of depths due to successive cycles of marine transgression and regression. The Lower Cretaceous Nubia and Matulla sandstone members are previously discovered, with highly productive reservoir wells (Figure 2.4). Further reservoir analysis and petrophysical investigations on the lower and middle Miocene formations (Nukhul, Rudeis, Kareem, and Belayim formations), using the structural model and interpretations of this paper, could be effective in new hydrocarbon accumulation discoveries.

The tectonic regime of this area is affected by several tectonic stresses in several directions. Firstly, compressional stress, igneous activity and basement uplift caused the anticline fold structures, strike-slip faults and shear zones (McClay and Khalil, 1998; Badri et al., 1999; Bosworth and McClay, 2001; Farhoud K., 2009) (Figure 2.3). The extensional stresses and NE trending shear zones dominated the area during rifting of the Gulf of Suez and Red Sea, resulting in a series of rotated normal fault structures that were significant in the created structural models and extracted cross sections (Figures 2.11 and 2.12). The area also subjected to extension and subsidence, during the deposition of Rudeis Formation in the early Miocene. Hence, the fault and geological structures generated by such severe tectonics affects the migration and accumulation process of hydrocarbons in the area. The hydrocarbon is trapped in the peak of anticlines and at the rotated fault planes. By investigating the occurred faults patterns (Figures 2.11 and 2.12) together with lithological facies of the Miocene formations (Figures 2.3 and 2.4), we could detect several promising hydrocarbon accumulation reservoirs to be drilled and exploited.

In an intensive study of the lithology (EGPC, 1996; Badri, 1999) of Nukhul, Rudeis, and Kareem formations, it was found that they comprise both shale source rocks and sandstone reservoir rocks. In the upper Miocene formations, Belayim and South Gharib formations consists of the seal evaporite rocks with interbedded sandstone layers. The hydrocarbon migration is interpreted to move from lower Miocene source rocks along fault planes and trapped by evaporite salt rocks or by the lateral change in lithology among the fractures and fault planes, such as when Nukhul formation is aligned with Sudr Chalk Formation. The presence of unconformities plays an important role in fluid dynamics and trapping, such as Mid Clysmic unconformity dividing Rudies Formation into lower and upper members (Farhoud, 2009). Harding (1985) stated that early structural pattern characterization is an essential exploration function, and the proper picking of prospect models is commonly relevant to the certainty of such identification. Therefore, the structural features of the REU field were analyzed thoroughly by mapping the distribution of faults and geological continuities that could control the trapping style.

In the REU area and most of Gulf of Suez, the evaporite salt layers played main role the seismic data quality in addition to its influence on the sealing and trapping the hydrocarbon dynamics. The quality of the Miocene seismic reflectors was good, especially for the tops of Belayim, Kareem, Rudeis, and Nukhul formations, except the parts with shallow basement blocks, these blocks are characterized by wave diffractions, noises, and energy absorption. As a result, even among the shifted parts, the contact between the Miocene layers and the bedrock layers was barely visible. The proportions of this shallow basement block are difficult to see, and the reflector continuity is inconsistent, while the quality of seismic data in areas impacted by listric faults was fair. The data quality above the fault plane was influenced by distortions and dispersed noises, while the data purity below it was hampered by multiples. The source of these multiples reflected from the South Garib and Belayim formations consisting of a thick sequence of evaporites interbedded with thin clastics.

The quality of the Pre-Miocene reflectors was poor because: (1) In the Zeit and Belayim formations, a thick evaporite portion was observed, that was the reason for seismic energy mitigation and absorption; 2) The acquired data and velocity analysis interpretation were influenced by dip reversals detected in the Miocene layers, which had numerous dips in different orientations; (3) The Rudeis formation’s thickness reaches a thousand meters in certain locations, causing absorption and dispersion of both incident and reflected waves, declaring a lack of acoustic energy transmission; and (4) Diffractions and dispersed acoustics were developed by tight space and cross fractures, which could be tampered and accumulated to produce false reflections of arbitrary trends.

In other respects, to achieve a good and more accurate interpretation and pre-salt image, integration of recent advanced seismic reprocessing techniques (e.g., adaptive beam migration (ABM), 3D depth/time migration) should be applied on the pre-stacked seismic data of the REU area. These processing methods could solve and image clearly the cases that requires multi-arrival (multi-component) imaging, steeply dipping and/or overturned structures as below complicated salt bodies. Higher-resolution pre-salt images requires a precise post-salt velocity model, thereby a combination of tilted transverse isotropy (TTI) tomography and full waveform inversion (FWI) should be applied (Sriram A. et al., 2020).

2.8 Conclusions

A detailed structural model for the Ras El Ush field (Gulf of Suez, Egypt) was constructed based on seismic and well logging data. Implementation of seismic attributes complemented offshore subsurface structural features, such as up-thrown trapping, subsalt structures, fault interpretation, and its related possible hydrocarbon structural trap occurrence. This paper shows an approach that offer clues to unlock some of the secrets of the active rift and its structural aspects on the fluid dynamics, and to explore undiscovered reserves. Also, these results provide recent geologic structural updates could be helpful for possible future effective enhanced recovery methods of oil and gas among previously drilled reserves of deeper formations as Matulla and Nubia sandstones. The structural evaluation of the Rudeis, Nukhul, and Matulla formations in the Ras El Ush field exhibits distinct NW-SE to NE-SW fault systems. The final extracted 3D modeling subdivided the research area into several blocks, allowing future selection of appropriate wells in the area and offers insights of the Ras El Ush’s structural framework. Also, this model could be utilized to re-evaluate the hydrocarbon potentially in Rudeis and Nukhul formations. The structural model can be used in future monitoring and investigating variations in physical properties, if the complex structures are developed due to various tectonic stresses dominate the Gulf of Suez as the area lies in the active rift zone. Finally, the reprocessing of the post-stacked seismic data of REU is recommended, to achieve more accurate interpretation and high-resolution pre-salt images, especially for the productive layers as Nubia, Matulla and Lower Miocene formations.

2.9 References

Abd-Allah, Z.M., Abdullah, W.H. and Abdel-Fattah, M.I., 2019. Assessment of Eocene, Paleocene and Cretaceous source rocks in the West Feiran area, offshore Gulf of Suez, Egypt. Journal of Petroleum Science and Engineering, 180, pp.756-772.

Abd El-Naby, A., Abd El-Aal, M., Kuss, J., Boukhary, M. and Lashin, A., 2009. Structural and basin evolution in Miocene time, southwestern Gulf of Suez, Egypt. Neues Jahrbuch für Geologie und Paläontologie–Abhandlungen, 251(3), pp.331-353.

Abdel-Fattah, M.I., 2010. Geophysical Reservoir Evaluation of Obaiyed Field, Western Desert, Egypt. PhD Dissertation.

Abdel-Fattah, M.I. and Alrefaee, H.A., 2014. Diacritical seismic signatures for complex geological structures: case studies from Shushan Basin (Egypt) and Arkoma Basin (USA). International Journal of Geophysics, 2014.

Abdel-Fattah, M., Gameel, M., Awad, S. and Ismaila, A., 2015. Seismic interpretation of the aptian Alamein dolomite in the razzak oil field, Western Desert, Egypt. Arabian Journal of Geosciences, 8(7), pp.4669-4684.

Abdel-Fattah, M.I., Metwalli, F.I. and El Sayed, I.M., 2018. Static reservoir modeling of the Bahariya reservoirs for the oilfields development in South Umbarka area, Western Desert, Egypt. Journal of African Earth Sciences, 138, pp.1-13.

Abdel-Fattah, M.I., Pigott, J.D. and Abd-Allah, Z.M., 2017. Integrative 1D-2D basin modeling of the cretaceous Beni Suef basin, Western Desert, Egypt. Journal of Petroleum Science and

Engineering, 153, pp.297-313.

Abdel-Fattah, M.I., Pigott, J.D. and El-Sadek, M.S., 2020. Integrated seismic attributes and stochastic inversion for reservoir characterization: insights from Wadi field (NE Abu-Gharadig Basin, Egypt). Journal of African Earth Sciences, 161, p.103661.

Abdel-Fattah, M.I., Shendi, E.A.H., Kaiser, M.F. and Abuzied, S.M., 2021a. Unveiling geothermal potential sites along Gulf of Suez (Egypt) using an integrated geoscience approach. Terra Nova, 33(3), pp.306-319.

Abdel-Fattah, M.I., Attia, T.E., El-Aal, A., Mohamed, H. and Hanafy, M.I., 2021b. Seismic interpretation of the Late Albian-Early Cenomanian Bahariya reservoirs of Burg El Arab oil field for tectonic evaluation: a case study from Western Desert, Egypt. Arabian Journal of Geosciences, 14(5), pp.1-11.

Abdullah, E.A., Abdelmaksoud, A. and Hassan, M.A., 2021. Application of 3D Static Modelling in Reservoir Characterization: A Case Study from Qishn Formation in Sharyoof Oil Field, Masila Basin, Yemen. Acta Geologica Sinica ‐ English Edition.

Abuzied, S.M., Kaiser, M.F., Shendi, E.A.H. and Abdel-Fattah, M.I., 2020. Multi-criteria decision support for geothermal resources exploration based on remote sensing, GIS and geophysical techniques along the Gulf of Suez coastal area, Egypt. Geothermics, 88, p.101893.

Acuña-Uribe, M., Pico-Forero, M.C., Goyes-Peñafiel, P. and Mateus, D., 2021. Enhanced ant tracking: Using a multispectral seismic attribute workflow to improve 3D fault detection. The Leading Edge, 40(7), pp.502-512.

Alsharhan, A.S., 2003. Petroleum geology and potential hydrocarbon plays in the Gulf of Suez rift basin, Egypt. AAPG, Bull, V. 87, No. 1, pp. 143-180.

Awni F., A.R., M.A. and S.A. 1990. Belayim Marine and Belayim Land Oil Fields structural Styles. EGPC, 10th Petrol. Expl. And Prod. Conf. In: 10th Petroleum Exploration and Production Conference. pp. 1–30, Cairo.

Badley, M.E., 1985. Practical Seismic Interpretation. IHRDC, Boston.

Badri, M.A., Taha, T.M. and Wiley, R.W., 1999. Subsalt Depth Imaging Using 3-D VSP Technique in the Ras El Ush Field, Gulf of Suez, Egypt. GeoArabia, 4(3), pp.363-378.

Basir, H.M., Javaherian, A. and Yaraki, M.T., 2013. Multi-attribute ant-tracking and neural network for fault detection: A case study of an Iranian oilfield. Journal of Geophysics and Engineering, 10(1), p.015009.

Bosworth, W., Huchon, P. and McClay, K., 2005. The red sea and gulf of aden basins. Journal of African Earth Sciences, 43(1-3), pp.334-378.

Bosworth, W. and McClay, K., 2001. Structural and stratigraphic evolution of the Gulf of Suez rift, Egypt: a synthesis. Mémoires du Muséum national d'histoire naturelle (1993), 186, pp.567-606.

Brown, A.R., 2001. Understanding seismic attributes. Geophysics, 66(1), pp.47-48.

Chhun, C., Kioka, A., Jia, J. and Tsuji, T., 2018. Characterization of hydrate and gas reservoirs in plate convergent margin by applying rock physics to high-resolution seismic velocity model. Marine and Petroleum Geology, 92, pp.719-732.

Chopra, S. and Marfurt, K.J., 2007. Volumetric curvature attributes add value to 3D seismic data interpretation. The Leading Edge, 26(7), pp.856-867.

Darwish, M. and El-Araby, A.M., 1993. Petrography and diagenetic aspects of some siliciclastic hydrocarbon reservoirs in relation to the rifting of the Gulf of Suez: Geological Society of Egypt Special Publication 1.

De Jager, G. and Pols, R.W.J., 2006. A fresh look at integrated reservoir modelling software. First break, 24(10).

Egyptian General Petroleum Corporation (EGPC), 1996. Gulf of Suez oil fields (a comprehensive overview). 736-undefined.

Eng, C. and Tsuji, T., 2019. Influence of faults and slumping on hydrocarbon migration inferred from 3D seismic attributes: Sanriku-Oki forearc basin, northeast Japan. Marine and Petroleum Geology, 99, pp.175-189.

Fadul, M.F., El Dawi, M.G. and Abdel-Fattah, M.I., 2020. Seismic interpretation and tectonic regime of Sudanese Rift System: implications for hydrocarbon exploration in neem field (Muglad Basin). Journal of Petroleum Science and Engineering, 191, p.107223.

Farhoud, K., 2009. Accommodation zones and tectono-stratigraphy of the Gulf of Suez, Egypt: a contribution from aeromagnetic analysis. GeoArabia, 14(4), pp.139-162. Friedman, G.M., 1985. Gulf of Elat (Aqaba) geological and sedimentological framework. In Hypersaline Ecosystems (pp. 39-71). Springer, Berlin, Heidelberg.

Harding, T.P., 1985. Seismic characteristics and identification of negative flower structures, positive flower structures, and positive structural inversion. AAPG bulletin, 69(4), pp.582-600.

Khan, M. and Abdelmaksoud, A., 2020. Unfolding impacts of freaky tectonics on sedimentary sequences along passive margins: Pioneer findings from western Indian continental margin (Offshore Indus Basin). Marine and Petroleum Geology, 119, p.104499.

Makky, A.F., Sayed, M.I.E. and Abd-Allah, Z.M., 2010. HYDROCARBON POTENTIALITY OF SOME MIOCENE ROCK UNITS IN THE CENTRAL PART OF THE GULF OF SUEZ, EGYPT. International Journal of Academic Research, 2(2).

Marfurt, K.J. and Alves, T.M., 2015. Pitfalls and limitations in seismic attribute interpretation of tectonic features. Interpretation, 3(1), pp.SB5-SB15.

McClay, K. and Khalil, S., 1998. Extensional hard linkages, eastern Gulf of Suez, Egypt. Geology, 26(6), pp.563-566.

Meshref, W.M., Refai, E.M. and Abdel-Baki, S., 1976, November. Structural interpretation of the Gulf of Suez and its oil potentialities. In EGPC 5th Exploration Seminar, Cairo, Egypt.

Moustafa, A.R. and Khalil, S.M., 2020. Structural setting and tectonic evolution of the Gulf of Suez, NW red sea and Gulf of Aqaba Rift systems. In The geology of Egypt (pp. 295-342). Springer, Cham.

Neves, F.A., Zahrani, M.S. and Bremkamp, S.W., 2004. Detection of potential fractures and small faults using seismic attributes. The Leading Edge, 23(9), pp.903-906.

Othman, A.A. and Fathy, M., 2015. Structure Modeling and Petrophysical Analysis in the Ras El Ush Field, Gulf of Suez, Egypt. New York Science Journal. 8, 3, 73–87.

Othman, A.A., Fathy, M., Othman, M. and Khalil, M., 2021. 3D static modeling of the Nubia Sandstone reservoir, gamma offshore field, southwestern part of the Gulf of Suez, Egypt. Journal of African Earth Sciences, 177, p.104160.

Paulsson, B.J.Ö.R.N., Fuller, B., Karrenbach, M. and Heuermann, F., 2001. Borehole Data: Closer to the rocks. Explorer, 22(7).

Patton, T.L., Moustafa, A.R., Nelson, R.A. and Abdine, S.A., 1994. Tectonic evolution and structural setting of the Suez Rift: Chapter 1: Part I. Type Basin: Gulf of Suez.

Pedersen, S.I., Randen, T., Sonneland, L. and Steen, Ø., 2002. Automatic fault extraction using artificial ants. In SEG Technical Program Expanded Abstracts 2002 (pp. 512-515). Society of Exploration Geophysicists.

Said, R., 1962. Geology of Egypt: New york, Amesterdam, El Sevier, 317P.

Said, R., 1990. The Geology of Egypt: A. A. Balkeme / Rotterdam / Brook field, 727P.

Santosh, D., Aditi, B., Poonam, K., Priyanka, S., Rao, P.H., Hasan, S.Z. and Harinarayana, T., 2013. An integrated approach for faults and fractures delineation with dip and curvature attributes. In 10th biennial international conference and exposition on petroleum geophysics, Kochi (pp. 23-5).

Sriram A., Mavilio, A.V., Lebit, H., 2020. Improved presalt imaging using innovative model-driven imaging technology. First Break, 38 (3), (pp 83 – 89).

Tsuji, T., Matsuoka, T., Yamada, Y., Nakamura, Y., Ashi, J., Tokuyama, H., Kuramoto, S.I. and Bangs, N.L., 2005. Initiation of plate boundary slip in the Nankai Trough off the Muroto peninsula, southwest Japan. Geophysical Research Letters, 32(12).

Tsuji, T., Kamei, R. and Pratt, R.G., 2014. Pore pressure distribution of a mega-splay fault system in the Nankai Trough subduction zone: Insight into up-dip extent of the seismogenic zone. Earth and Planetary Science Letters, 396, pp.165-178.

Tsuji, T., Kodaira, S., Ashi, J. and Park, J.O., 2013. Widely distributed thrust and strike-slip faults within subducting oceanic crust in the Nankai Trough off the Kii Peninsula, Japan. Tectonophysics, 600, pp.52-62.

Younes, A.I. and McClay, K., 2002. Development of accommodation zones in the Gulf of Suez-Red Sea rift, Egypt. AAPG bulletin, 86(6), pp.1003-1026.

Chapter 3

Extracting high-resolution P-wave reflectivity of the shallow subsurface by seismic interferometry based on autocorrelation of blast mining signals

3.1 Introduction

Seismic interferometry can be used to extract a zero-offset reflection response beneath a seismic station based on autocorrelation analysis of the observed seismic signals. This technique is attractive as it turns a single physical geophone into a virtual source and receiver for imaging subsurface structures (Claerbout, 1968; Wapenaar, 2004; Nakahara, 2006; Suemoto et al., 2020). Station deployment for autocorrelation analysis is also simpler compared to traditional seismic reflection methods. Most previous studies performing seismic interferometry by autocorrelation used the codas of earthquakes or ambient noise data as input signals.

In autocorrelation analyses, the frequencies of the used signals mainly determine the investigable depth and resolution. High-frequency signals over a broad frequency range are required to resolve reflectors from shallow target depths at high-resolution (Saygin et al., 2017). However, the earthquake or ambient noise signals conventionally used in autocorrelation analyses have limited high-frequency energy, despite the utility of their low-frequency components for deep-earth exploration (e.g., deep-basin imaging or crustal thickness determinations). For instance, the depth of the Moho and crustal thickness are estimated from autocorrelation analysis using frequencies of 0.2–4 Hz (Tibuleac and von Seggern, 2012; Gorbatov, et al., 2013; Kennett et al., 2015; Taylor et al., 2016; Oren and Nowack, 2017; Becker and Knapmeyer-Endrun, 2018; Mroczek and Tilmann, 2021). In contrast, numerous studies have mapped shallower subsurface features such as basins using higher frequency ambient noise. Saygin et al. (2017) retrieved P-wave reflectivity responses from noise autocorrelations in the Jakarta basin using frequencies of

2–4 Hz. Romero and Schimmel (2018) successfully used autocorrelations of ambient noise signals at 3–18 Hz to map the basement depth in the Ebro basin (Spain). Chimoto and Yamanaka (2019, 2020) applied autocorrelation analysis to the horizontal components of S-waves from regional natural earthquakes to image the depths of deep sedimentary layers. Zhang et al. (2021) extracted P-wave reflectivities related to the soil/rock interface within 50 m of the surface using ambient noise signals with peak frequencies at ~5 Hz by exploiting velocity information obtained from drilled well data. Heath et al. (2018) used autocorrelation analyses of both ambient noise and teleseismic earthquake coda signals to investigate the structures of upper crustal magmatic systems at volcanic geothermal sites by filtering the signals into two frequency bands (3–9 Hz and 0.5–2 Hz).

Here, we present a new approach using high-frequency mine explosions (blasts) as an applied signal in the autocorrelation analysis to retrieve P-wave reflectivity data for the shallow subsurface. Since the blast signals include higher frequency components than natural earthquakes and ambient seismic noise, their use in autocorrelation analysis has the potential to image the boundaries of shallow subsurface structures at high-resolution. To demonstrate the feasibility of our approach, we conducted two seismic surveys by recording mine blasts in the Hishikari area, Japan. In the first survey, seismic data were continuously acquired over a period of two months (including a natural earthquake) at a relatively large receiver spacing. The second survey was performed in a single day but with a denser receiver spacing. A comparison of the results highlights the merits and drawbacks of obtaining coherent reflections from each type of seismic data and demonstrates that blast-mining events are more reliable and obtain higher amplitude reflections, especially at shallow depths. Using the blast signals acquired with the dense seismometer array, we extracted high-resolution reflection profiles of shallow lithological boundaries in the Hishikari area, from which we detected heterogeneities that are possibly related to fissures filled by ore deposits.

3.2 Geological setting

The Hishikari mine epithermal gold-silver deposit (~50 km northeast of Kagoshima, southern Kyushu, Japan) is the largest gold mine in Japan and one of the world’s richest gold mines (Figure 3.1a). The ore deposits are remarkably high-grade concentrations of gold occurring in fractures and fissure-filling vein systems within the volcanic andesitic rocks and shale of the Shimanto supergroup. Topography in this area ranges from 200 to 600 m elevation. Geologically, the mine area consists of the Shimanto supergroup (Cretaceous) and Quaternary volcanic rocks and alluvial deposits. The Shimanto supergroup comprises shale, sandstone, and their alterations, and is unconformably overlain by the Quaternary volcanic rocks (Figure 3.1c and 3.1d; (Izawa et al., 1990; Uto et al., 2001; Sekine et al., 2002)). The Quaternary calc-alkaline volcanic rocks consist of the Hishikari lower and middle andesites, the Shishimano dacites, welded tuffs, and pyroclastic flow deposits. The Metal Mining Agency of Japan performed geophysical surveys in the area to identify valuable ore deposits and generate regional geological maps. Drilling operations began in 1981, and holes drilled during the subsequent development of the mine by Sumitomo Metal Mining (SMM) intersected high-grade ores (Okada, 2000). The basement in this area was previously delimited by Okada (1995) using a combination of geophysical surveys (gravity, electrical resistivity, and induced polarization).

3.3 Data

In our first survey, we continuously recorded seismic data over the Hishikari mine for two months between March and May 2021. We deployed 12 McSEIS-AT seismometers (2 three-component and 10 single-component vertical seismometers) at the ground surface above the mine. The stations were deployed in two parallel profiles, including seven stations in the western profile and five in the eastern profile; station spacing was about 100 m in both profiles (Figure 3.1a).

We performed our second survey on 24 November 2021 during a period of about three hours that included mine blasting. In this survey, we used a denser station array of 33 three-component seismometers, including 23 McSEIS-AT seismometers with a sampling rate of 0.004 s and 10 IGU-BD3C-5 seismometers with a sampling rate of 0.001 s, deployed in the Yamada paddy field about 300 m west of the western profile in the first survey (Figure 3.1b). In the single-day (second) survey, to check the consistency of the seismic responses of both types of seismometers McSEIS-AT and IGU-BD3C-5 in the autocorrelation analysis, we deployed one IGU-BD3C-5 seismometer (442) alongside one McSEIS-AT seismometer (114) at the same location. We calculated the autocorrelation functions of the same shot for both stations in the frequency range 12–40 Hz (Figure 3.2). This comparison shows that most reflections are consistent between the two seismometers.

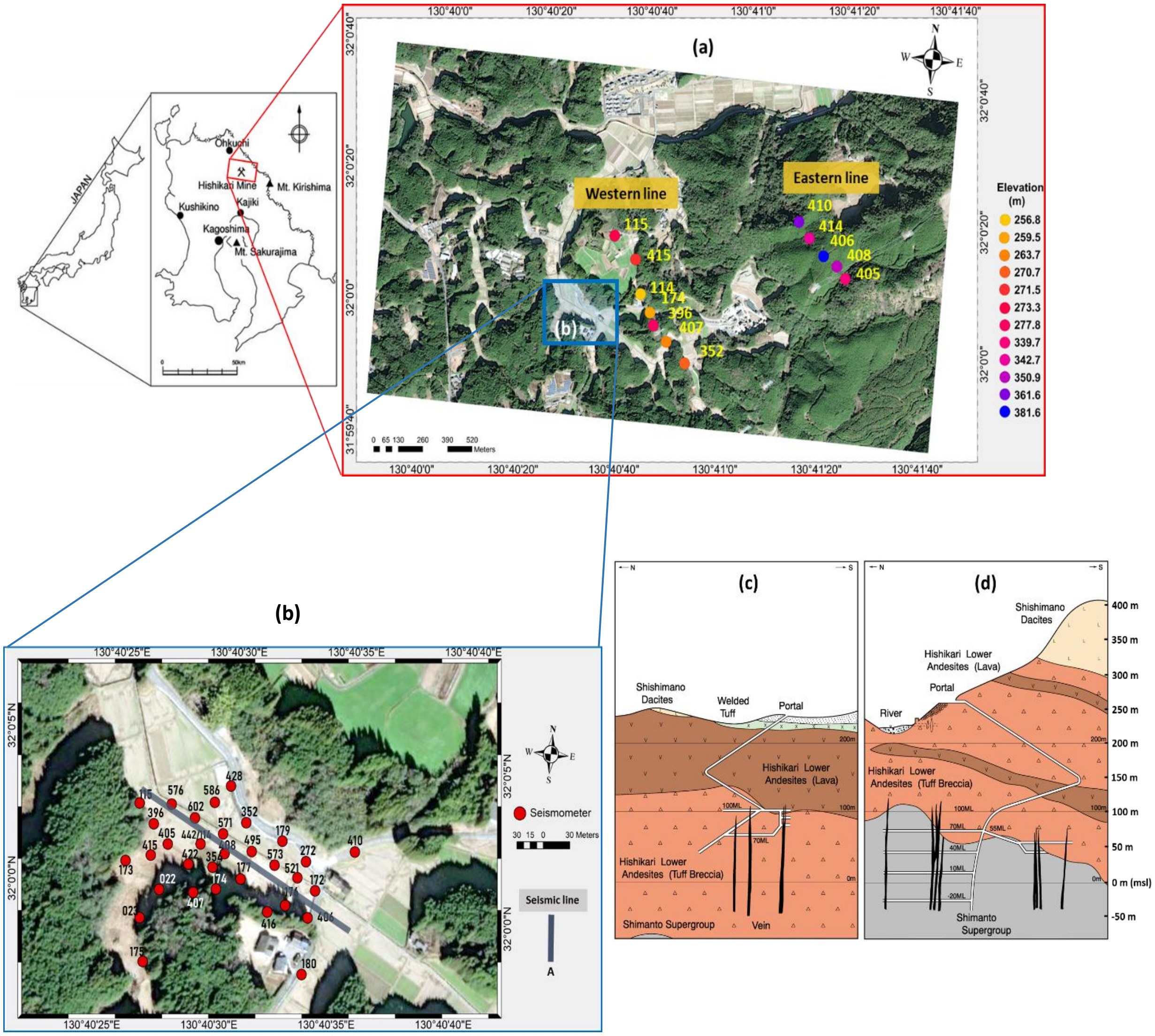

Figure 3.1: (a) Map of the Hishikari mine area showing the two parallel lines of seismic stations (dots) used during the two-month survey (March to May 2021). The western and eastern lines include seven and five stations, respectively. Station elevations are shown on the map. (b) Enlarged map showing the locations of the 33 stations (dots) used in the single-day survey (24 November 2021) and the seismic line (black line, 'A') used for projection. The average elevation is about 225 m. (c) and (d) Schematic geological cross sections showing the lithologies in the (a) western (Yamada field) and (b) eastern areas (Honko field)(Izawa et al., 1990; Okada, 1995; Sekine et al., 2002), as well as associated gold veins.

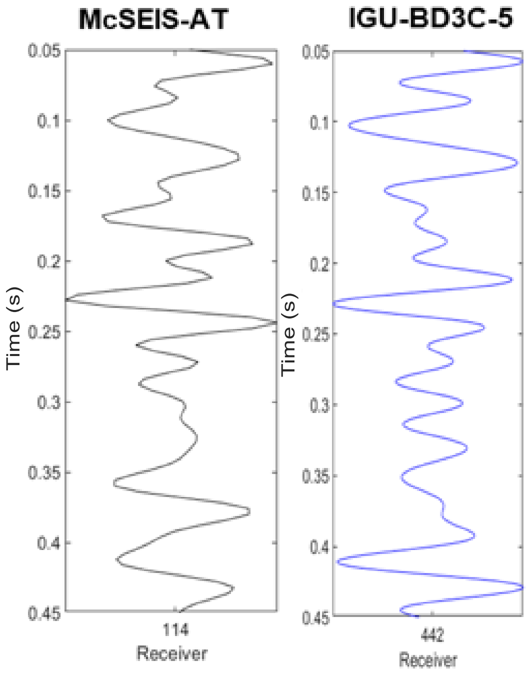

Figure 3.2: The autocorrelation seismic responses of the two types of stations used (McSEIS-AT and IGU-BD3C-5) when deployed at the same location (single-day survey) and filtered to the same frequency range (12–40 Hz).

Mine blasts occurred in the horizontally and sub-horizontally drilled mine shafts at known depths in the subsurface. Considering the seismic waves from the blasts travelled to and reflected off different lithological boundaries, they can be used to estimate the P-wave reflectivity beneath each station associated with the lithological boundaries identified by autocorrelation analysis. In the first survey, we recorded more than 100 blasts, of which we used 40 in our analysis. In the second survey, we observed three blasts, but used only one that was carefully selected considering the signal-to-noise ratio (SNR) and the consistency of autocorrelation between two surveys (see Discussion). We calculated the SNRs of the blasts by dividing the amplitude spectra of the signal by that of the noise (Figures 3.3a–3.3d). Based on these frequency dependent SNRs, we determined the optimum frequency range for our analysis. The calculated SNR spectrum showed that the blasts produced signals over a broad frequency range from 10 Hz to more than 90 Hz (Figure 3.3e). The lower SNR at 60 Hz is associated with electric noise, and other low SNRs were observed at certain frequency bands (Figure 3.3c–3.3e). To prevent these noisy frequencies from influencing our autocorrelation analysis, they were removed by applying bandpass filters.

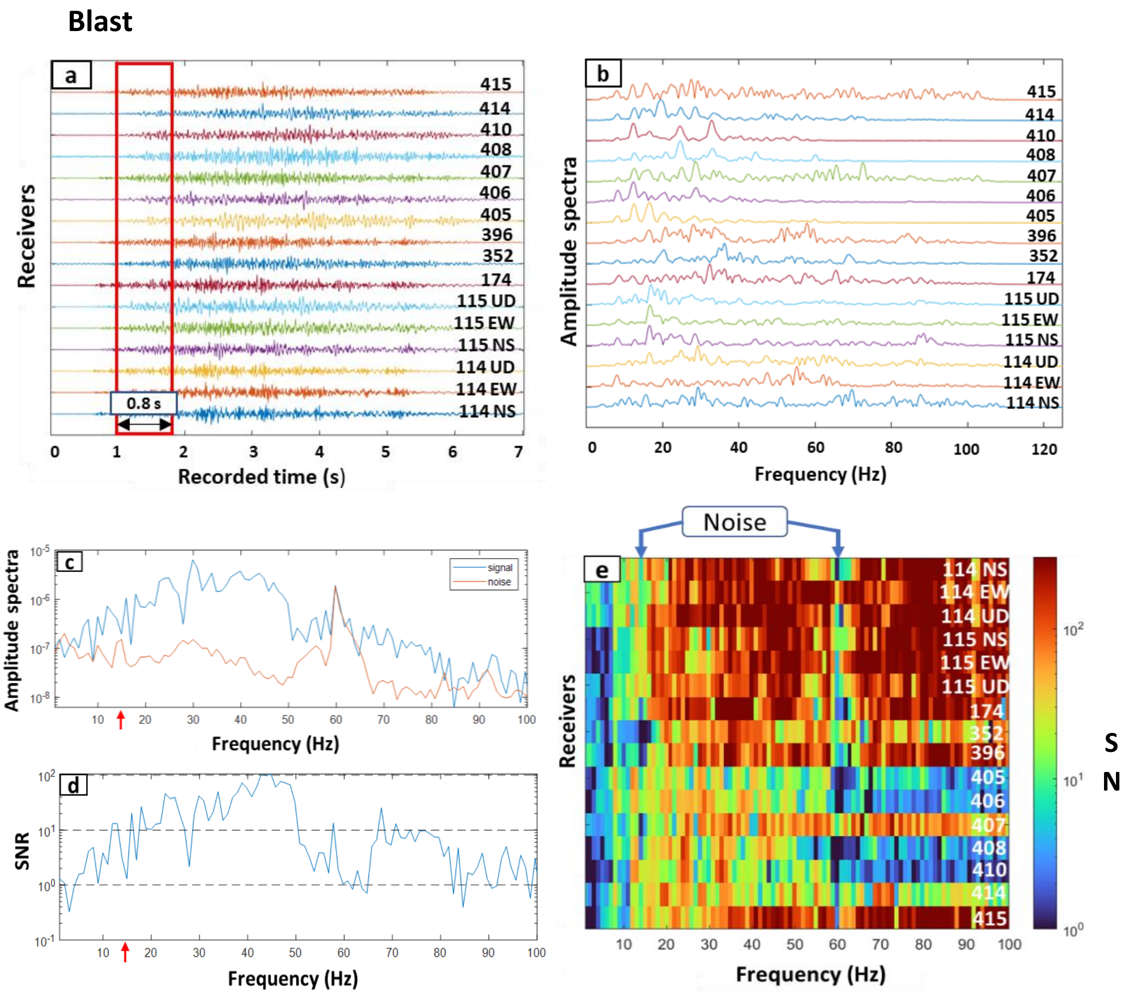

Figure 3.3: (a) Examples of raw blast signals from all stations, (b) their amplitude spectra before spectral whitening, (c) Fourier amplitude spectra of the signal (blast) and noise, (d) the frequency-dependent signal-to-noise ratio (SNR) obtained by dividing the amplitude spectrum of the signal by that of the noise, and (e) frequency-dependent SNRs for all stations. Red arrows in (c and d) highlights the observed noise around 14 Hz.

We also compared profiles derived from natural earthquake data and ambient noise data to the reflections obtained using the blast signals. The observed natural earthquake data show distinct P- and S-wave components (Figure 3.4a). Compared to the blast signals (Figure 3.3e), the SNR spectrum of the natural earthquake signals peaks in a lower and narrower frequency range between 0 and 40 Hz (Figure 3.4e). Localized noise was again observed at 60 Hz (Figure 3.4c–3.4e).

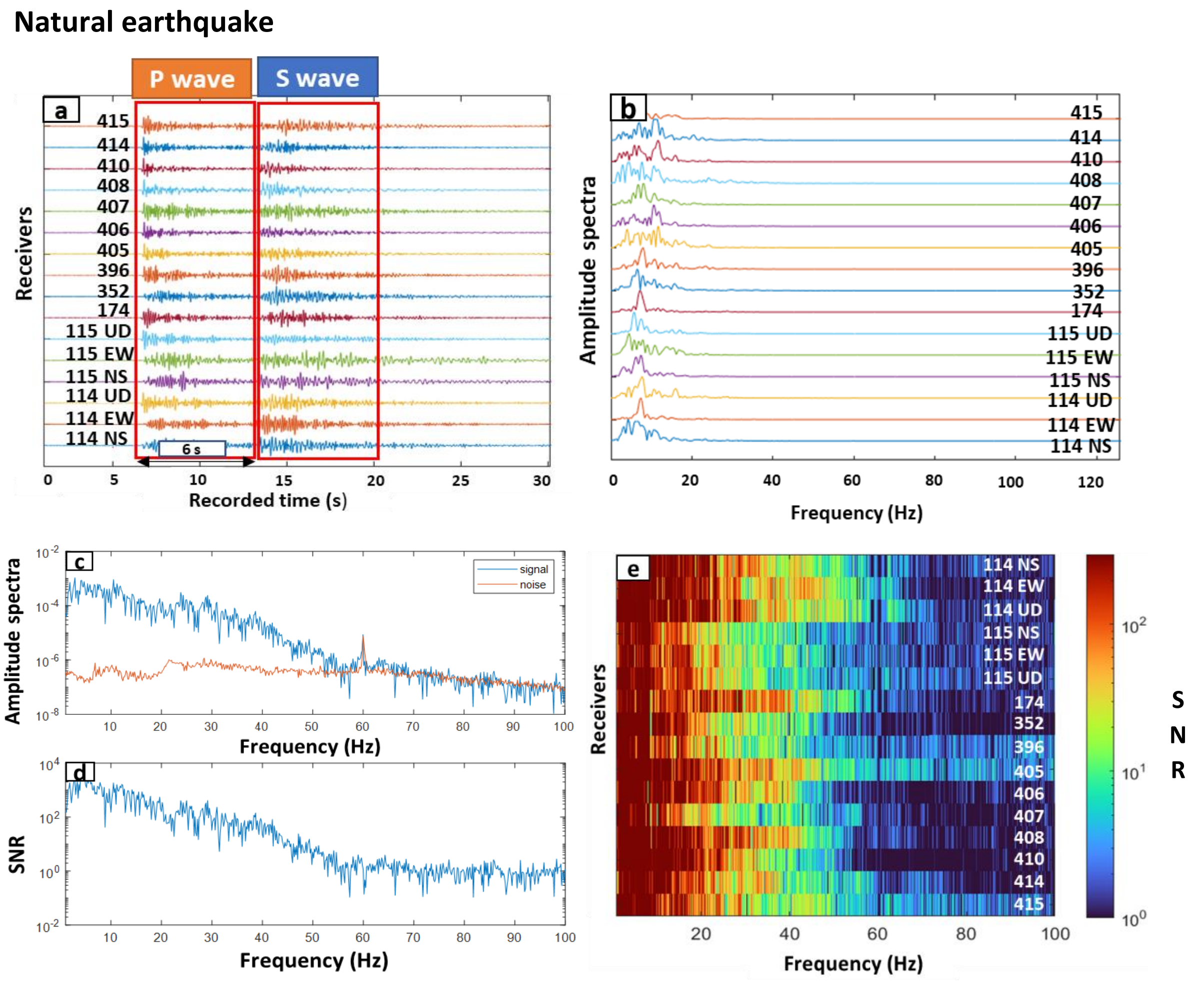

Figure 3.4: (a) Raw natural earthquake body wave signals from all stations, (b) their amplitude spectra before spectral whitening, (c) Fourier amplitude spectra of the signal and noise, (d) the frequency-dependent SNR obtained by dividing the amplitude spectrum of the signal by that of the noise, and (e) frequency-dependent SNRs for all stations.

Most of the ambient noises were probably sourced from the nearby Sakurajima and Kirishima volcanic activities and human activities near the mine. The amplitude spectra of ambient seismic noise (treated as noise in the blast and earthquake signals) showed two bands of local noise at around 8 and 60 Hz (Figure 3.5). Local noise at 14-Hz was only observed in the blast signals (red arrow in Figures 3.3c and 3.3d), and we observed a difference in the noise level between blast and earthquake signals (Figure 3.3c and 3.4c). These differences may be related to industrial and mining activities during the survey periods. Indeed, the natural earthquake event and the ambient noise used for our analysis were recorded on a non-working day (no mining operation). Therefore, we assume that mining activities caused the localized 14-Hz noise, as well as the difference in noise level between blast and earthquake signals.

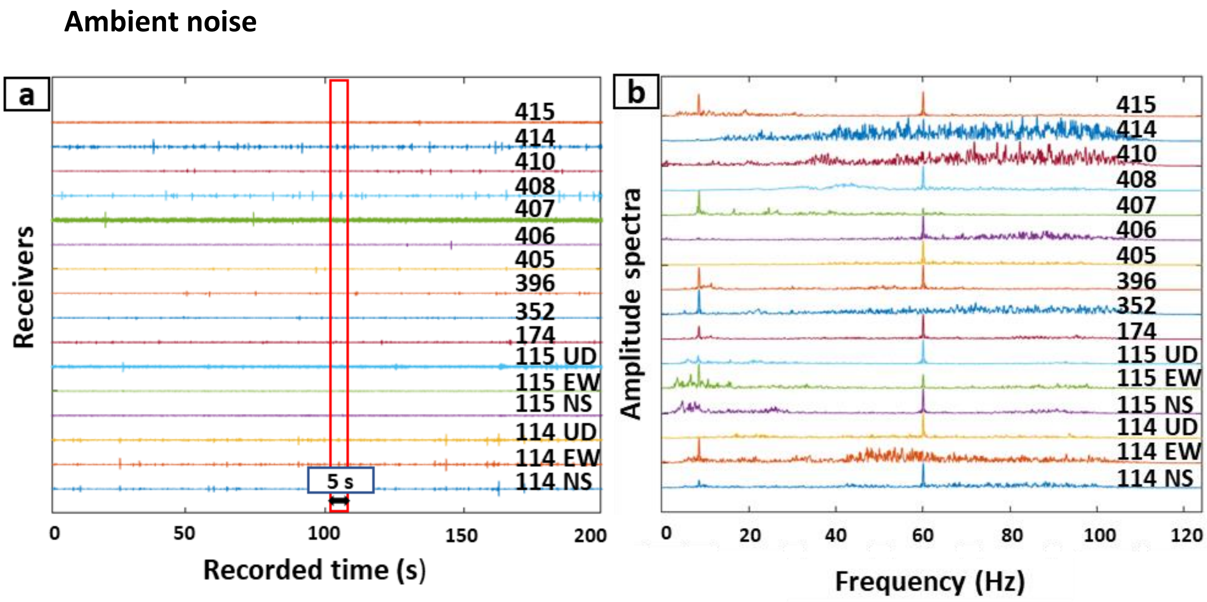

Figure 3.5: (a) Raw ambient noise from all stations, and (b) their amplitude spectra before spectral whitening.

3.4 Methods

To effectively extract P-wave reflections from seismic signals by autocorrelation analysis, we applied the processing workflow shown in Figure 3.6. When analyzing the blast data from the first survey, we extracted the raw blast data using a time window of 0.8 s. The mean value was removed from the raw data by applying a 10% cosine taper and the amplitude spectrum was then calculated by fast Fourier transform (FFT). To remove source effects from the blast signals, the amplitude spectrum was whitened by dividing the original amplitude spectrum by the smoothed one (Bensen et al., 2007; Oren and Nowack, 2017; Chimoto and Yamanaka, 2019; Wang et al., 2020). The calculated amplitude spectra were smoothed using a Gaussian smoothing filter. The autocorrelation function was calculated by applying an inverse FFT to the whitened spectrum after bandpass filtering. Finally, all individual autocorrelations from different blast events were linearly stacked to distinguish the dominant P-wave reflections. This stacking process attenuates incoherent signals or noise while boosting stationary signals (Becker and Knapmeyer-Endrun, 2018).

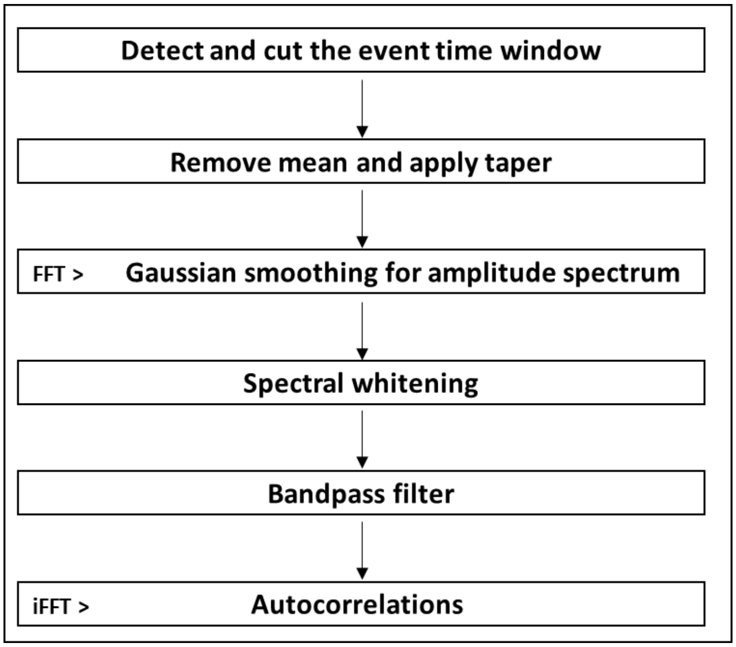

Figure 3.6: The processing workflow used to compute autocorrelations.

Although we used the same basic processing sequence described above to calculate the autocorrelation function from the earthquake data and ambient noise, we varied the specific processing parameters such as (1) the analyzed frequency ranges, (2) the width of the smoothing filter used to compute the Fourier amplitude spectrum, and (3) the time window of signal extraction for each source type (Table 3.1). The determinations of the specific values used for each parameter are described below.

Table 3.1 Frequency filtering ranges and smooth bandwidths applied to the blast, natural earthquake, and ambient noise signals.

Signal Processing	Blast		Earthquake		Ambient noise	
Frequency range	Bandpass filter (Hz)	Smoothing bandwidth (Hz)	Bandpass filter (Hz)	Smoothing bandwidth (Hz)	Bandpass filter (Hz)	Smoothing bandwidth (Hz)
Low	**6-20**	**10**	**2-20**	**8**	**2-20**	**10**
High	**15-58**		**5-38**		**5-30**	
Time window (s)	**0.8**		**6**		**5**	

It is desirable to use higher and wider frequency bands to image shallower lithological boundaries at high-resolution. Although body waves at lower frequencies (longer wavelength) can penetrate into the deeper parts, high-frequency components (shorter wavelength) are required to extract reflections from shallower layers with high-spatial resolution. In addition, the undulation frequencies f_D in the whitened spectrum is related to the delayed arrival times $T_D(= 1/f_D)$ (Oren and Nowack, 2017; Chimoto and Yamanaka, 2019). This means higher and wider frequency band is required to extract early time reflections from shallow boundaries in autocorrelation analysis. For each source type, we applied two bandpass filters to investigate the frequency (depth) dependence of the resulting reflection profiles. The two frequency ranges reported for each source type in Table 3.1 were determined by considering the amplitude spectra, the frequency dependent signal-to-noise ratios (SNRs) (Figures 3.3e, 3.4e and 3.5), and the quality of coherent reflections in the resulting reflection profiles. The reflection profiles from different frequency bands were compared for the blast shots. Although the frequency ranges selected for ambient noise (i.e., 2–20 and 5–30 Hz) include localized noise at 8 Hz, the noise was suppressed by applying a band-stop filter.

To define and select the optimum frequency parameters we show autocorrelation results using blasts for different frequency parameters: (1) the analyzed frequency range and (2) the width of smoothing in computing the smoothed Fourier amplitude spectrum.

Figure 3.7 shows single-blast autocorrelation images from the first survey obtained by applying several different smoothing bandwidths from 0.5 to 20 Hz and fixing the bandpass frequency range at 15–58 Hz. With smoothing bandwidths of 0.5 and 1 Hz, no clear reflected waves are produced, even at arrival times earlier than ~0.4 s, corresponding to shallower depths, although this 0.5-Hz bandwidth was used by Chimoto and Yamanaka (2020) for strong-motion data when imaging a deeper sedimentary basin. In contrast, with a smoothing bandwidth of 5 Hz, reflected waves were apparent at earlier arrival times, but no high-amplitude reflections were recorded before 0.3 s TWT. When applying 10 and 20 Hz bandwidths, the reflections are emphasized at earlier arrival times, but the reflection signals amplitudes slightly reduced for arrival times later than 0.4 s with the 20 Hz bandwidth. Therefore, we selected the 10 Hz bandwidth for processing the blasts.

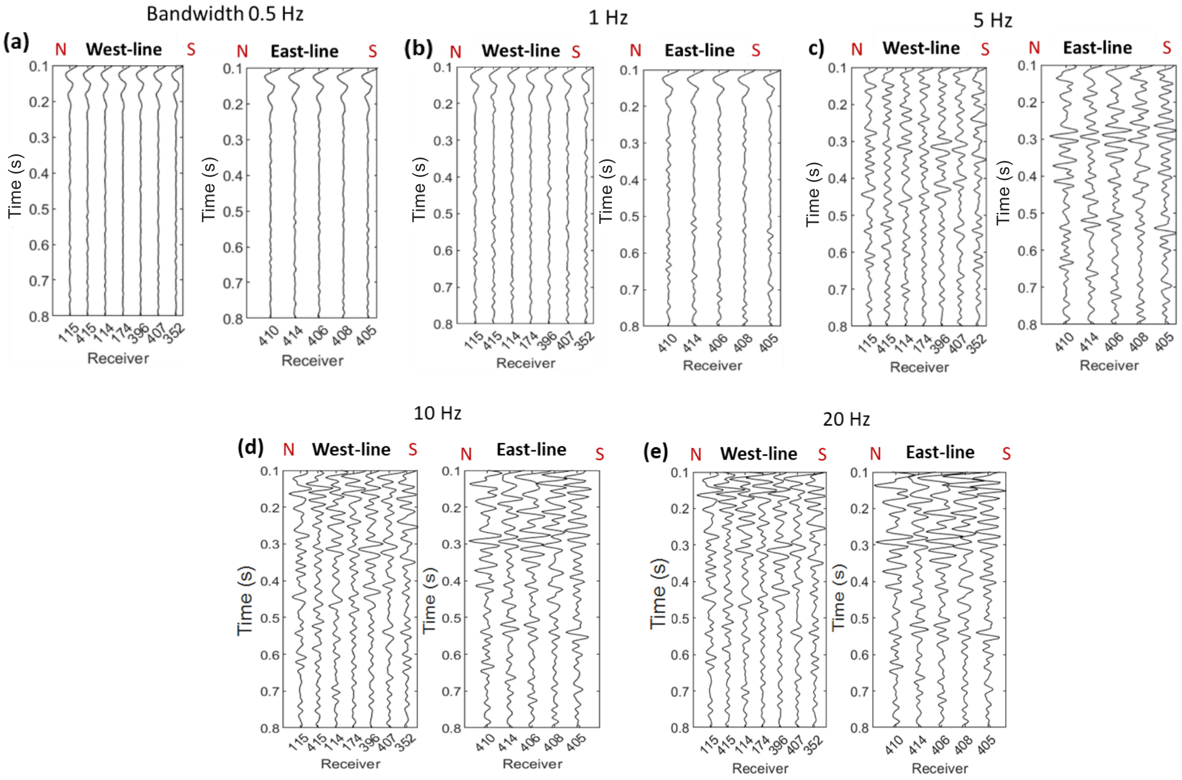

Figure 3.7: (a–e) Autocorrelation functions calculated using various smoothing bandwidths (0.5, 1, 5, 10, and 20 Hz, respectively) for the same single blast event used in Figure 3.3 (fixed bandpass filter at 15–58 Hz). For reference, (d) is identical to Figure 3.8e.

Figure 3.8 shows single blast autocorrelation images from the first survey obtained by applying various bandpass frequencies and fixing the smoothing bandwidth at 10 Hz. With a lower and narrower frequency bandpass filter (0.5–3 Hz), clear reflections were difficult to be extracted at any arrival time. Using a higher and wider frequency range (2–10 Hz), we were able to image the reflected waves, but only with low-resolution. In contrast, the highest frequency range (65–95 Hz) was characterized by low SNR, whereas the ranges 6–20, 15–35, and 15–58 Hz showed better reflection images. The 15–35 Hz range showed distortions and reduced resolution in some parts.

Therefore, we used the widest and highest possible frequency range of 15–58 Hz to obtain high SNR at early arrival times. To investigate reflections at later arrival times, we used the lower frequency range of 6–20 Hz.

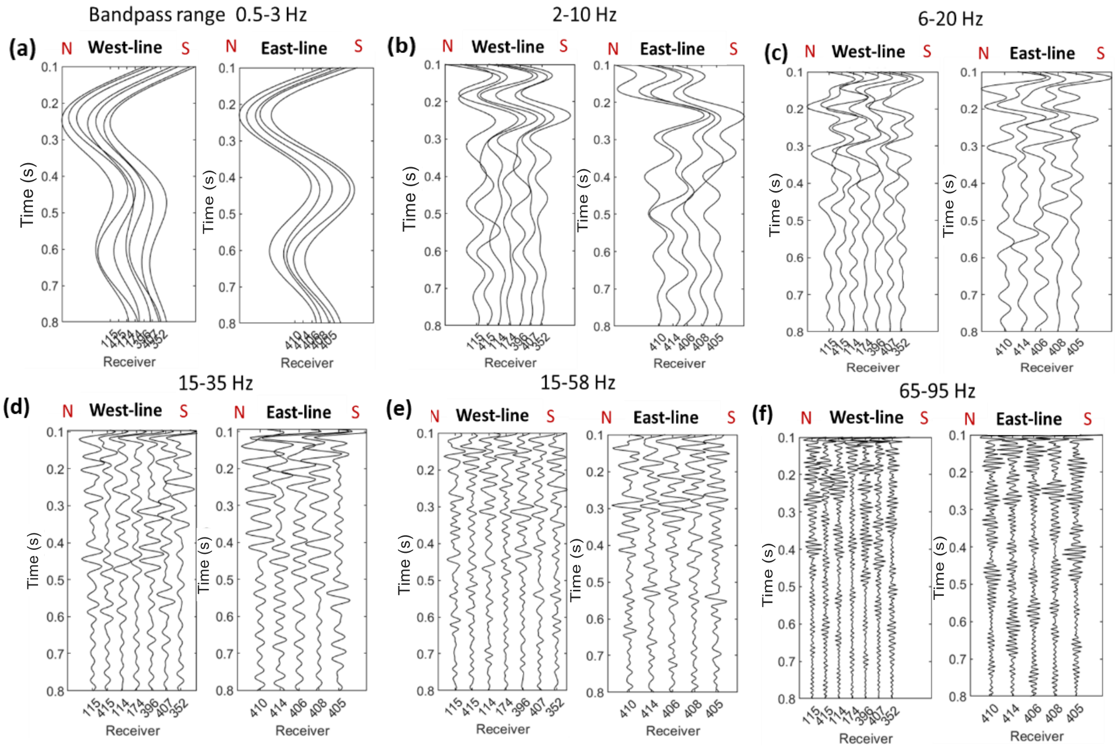

Figure 3.8: Autocorrelation images for the same single blast event shown in Figures 3.3 but here with different bandpass filter ranges and a fixed smoothing bandwidth of 10 Hz. For reference, (e) is identical to Figure 3.7d.

The width of the smoothing filter used to compute the Fourier amplitude spectrum impacts the reliability of the reflection signals obtained. Since the longer frequency cycles (i.e., higher undulation frequencies) are necessary to extract earlier reflections from shallower boundaries (e.g., Chimoto and Yamanaka, 2019), we used a relatively wide smoothing band. After testing the effects of several smoothing widths on the resulting autocorrelations (Figure 3.7), we chose optimal smoothing widths of 8–10 Hz (Table 3.1).

The time windows used to extract the blast, earthquake, and ambient noise in the first survey were 0.8, 6, and 5 s respectively (Table 3.1). The time window used for the blast signals was limited to 0.8 s in the first survey (Figure 3.3), because periodic signals were observed to influence the blast signals. These periodic signals might have resulted from the occurrence of many explosions in a short period of time (Figure 3.9), restricting the interpretable two-way travel time (TWT) in the autocorrelation results. To decrease the possible influence of these periodic signals, we calculated autocorrelations for each 0.8 s time window within the analysis period. Therefore, we stacked the many autocorrelations obtained from 0.8 s time windows and 40 shots. Considering that our target depth was shallow, however, the short time interval was sufficient to investigate shallow lithological boundaries (<500 m) or vein deposits shallower than 300 m.

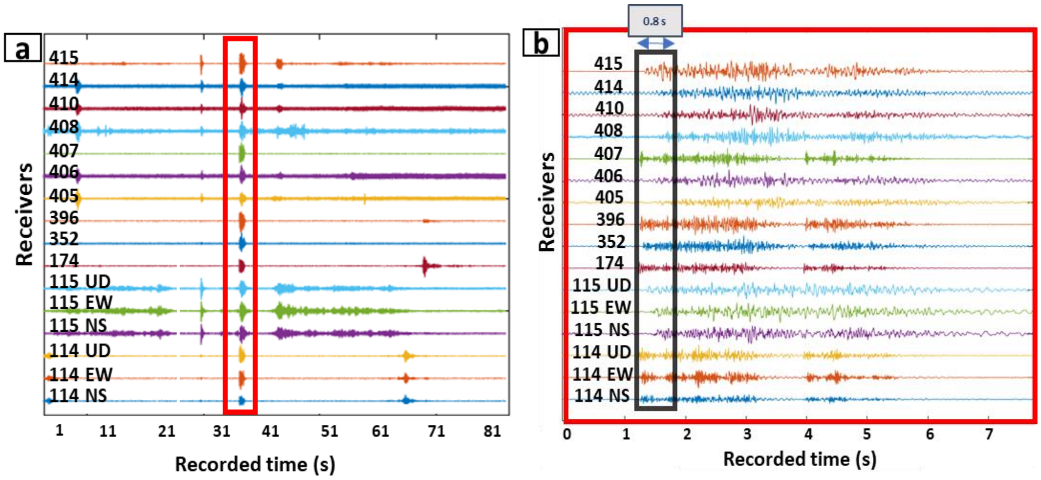

Figure 3.9: (a) Examples of raw blast data (two-month survey) at all stations in the time domain, and (b) a close-up of (a) showing the blast shot in the shorter time window indicated by the red rectangle in (a). Note the occurrence of periodic signals (minor shots) during the 0.8-s time window following the main blast marked in (b).

In ambient noise data analysis, 3-hour ambient noise data from non-working day were cut into 5-s time windows, and the resulting autocorrelations were calculated by stacking from each window. The preference of 5-s time window used for ambient noise was determined by testing several time intervals (e.g., 1, 5, 30, and 60 s) in autocorrelation function calculation. Based on analysis of 3 hours of noise data, better autocorrelations at shallow depths were obtained when using shorter time intervals. In addition, we investigated the influence of stacking time by changing the analyzed periods from 1 min to 72 hours. We computed autocorrelations for ambient noise during 1 min, 3 h, 12 h, 24 h and 72 h as shown in Figures 3.10 and 3.11 for both frequency ranges 2-20 Hz and 5-30 Hz, respectively. The results of 3-hour data stacking (Figures 3.10b and 3.11b) are much improved from those of 1 min data stacking (Figure 3.10a and 3.11a). However, further stacking (e.g., 12 hours) does not significantly improve results, thus we interpretated that 3 hours data were enough to obtain stable autocorrelations in our data.

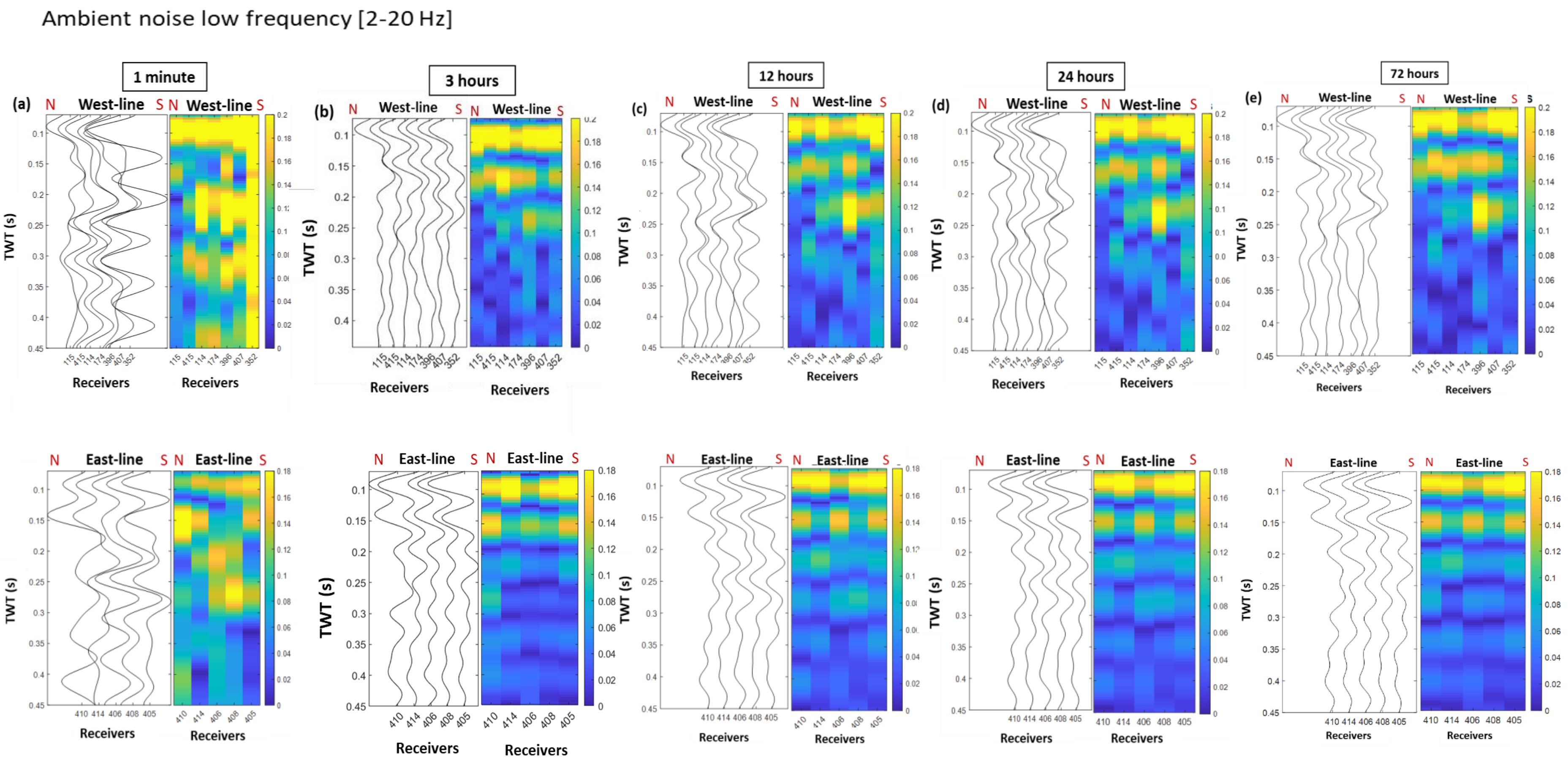

Figure 3.10: Stacking of 5-s time window for low-frequency (2-20 Hz) autocorrelation results of ambient noise data. Stacking was plotted for time periods (a) 1 minute, (b) 3 hours, (c) 12 hours, (d) 24 hours, and (e) 72 hours. The western lines were plotted side-by-side to show the effect of stacking and the same were done for the eastern lines.

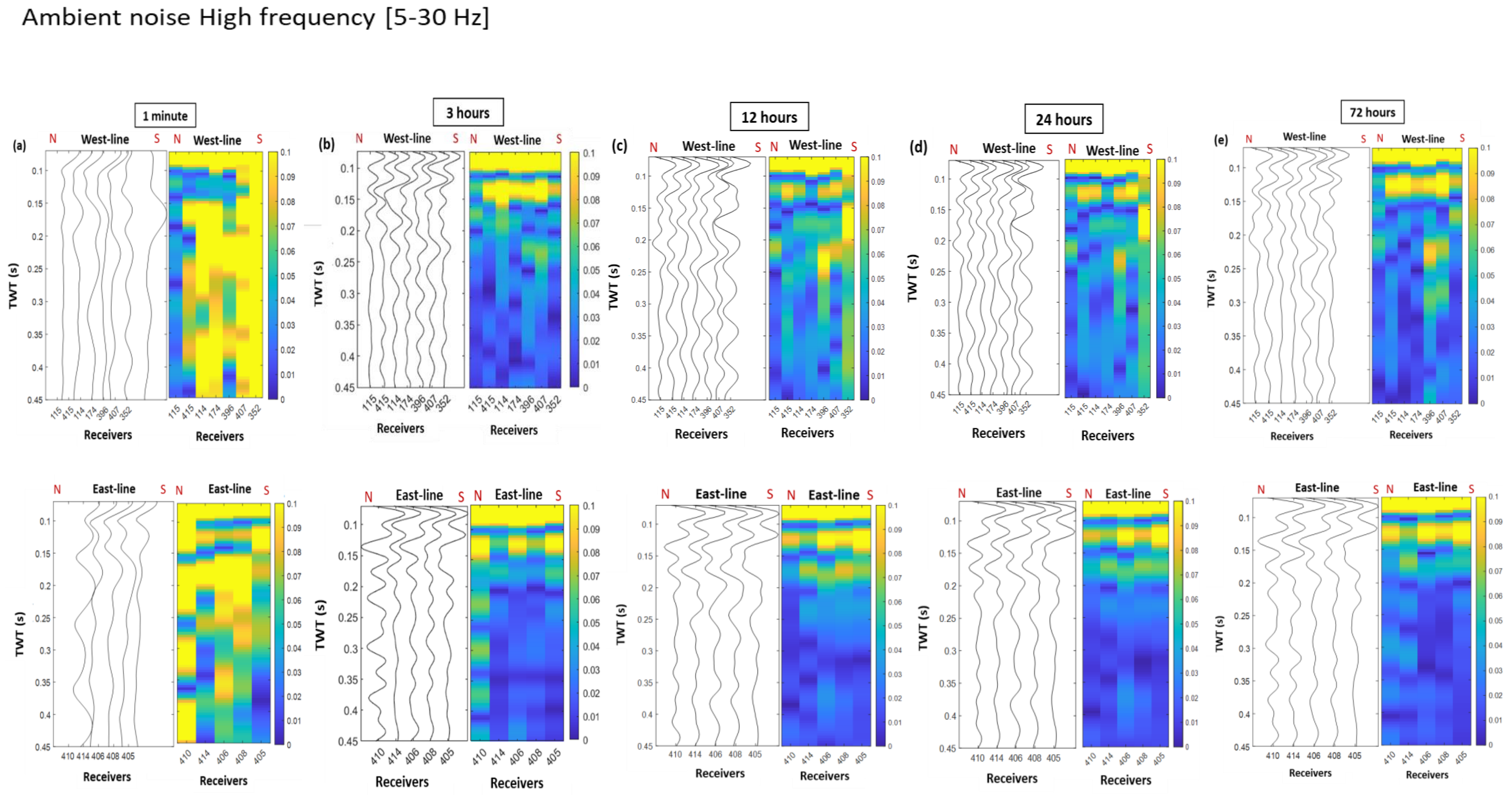

Figure 3.11: Stacking of 5-s time window for high-frequency (5-30 Hz) autocorrelation results of ambient noise data. Stacking was plotted for time periods (a) 1 minute, (b) 3 hours, (c) 12 hours, (d) 24 hours, and (e) 72 hours. The western lines were plotted side-by-side to show the effect of stacking and the same were done for the eastern lines.

3.5 Results and interpretations:

3.5.1 Autocorrelations using long-term sparse seismometer data (first survey)

Figures 3.12–3.14 show high- and low-frequency reflection profiles from the first survey computed using blast, earthquake, and ambient noise, respectively. Since the seismic autocorrelation approximates the zero-offset reflection profiles, the lag time is the two-way travel time (TWT) for the reflected waves. We also computed the absolute amplitude (envelope) for all the autocorrelations to better visualize the dominant reflections. Several reflections were clearly imaged at arrival times between 0.1 and 0.4 s in the three datasets (Figures 3.12–3.14). Furthermore, the results from the lower frequency range produced clearer reflections at later arrival times than those from the high-frequency range (panels c–d and a–b, respectively, in Figures 3.12–3.14).

In the autocorrelation results obtained by stacking 40 blast events at higher frequencies (15–58 Hz), we observed clear high-amplitude reflections at 0.11, 0.15, and 0.21 s TWT (Figure 3.12a and 3.12b). In the results using the lower frequency range (6–20 Hz), we observed two more reflections at 0.26 and 0.36 s TWT (Figures 3.12c and 3.12d). Because the high-frequency range was much wider than the low-frequency range, the autocorrelation reflections calculated using the high-frequency range (Figures 3.12a and 3.12b) are sharper and clearer than the low-frequency reflections (Figures 3.12c and 3.12d) at earlier times between 0.1 and 0.25 s TWT.

Blast

(High-frequency range [15-58 Hz])

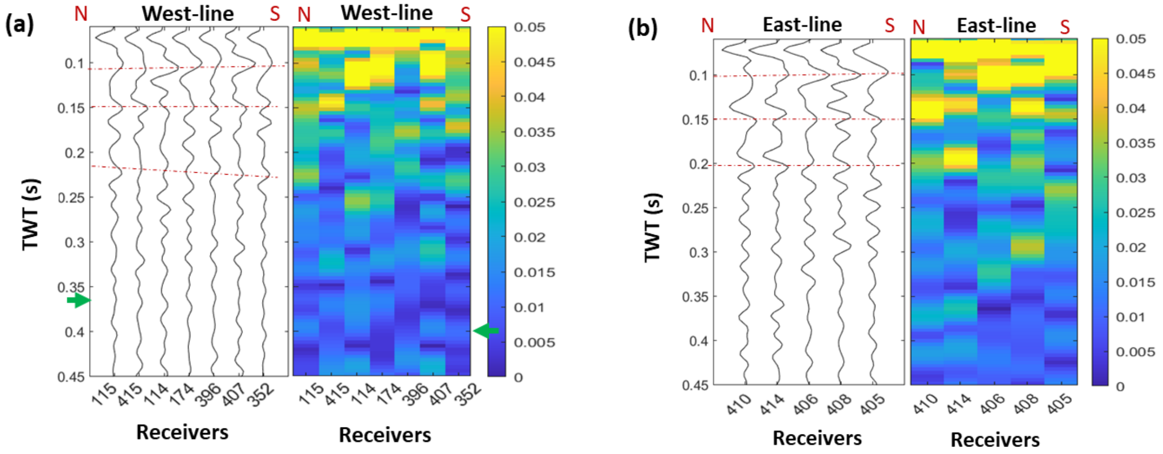

(Low-frequency range [6-20 Hz])

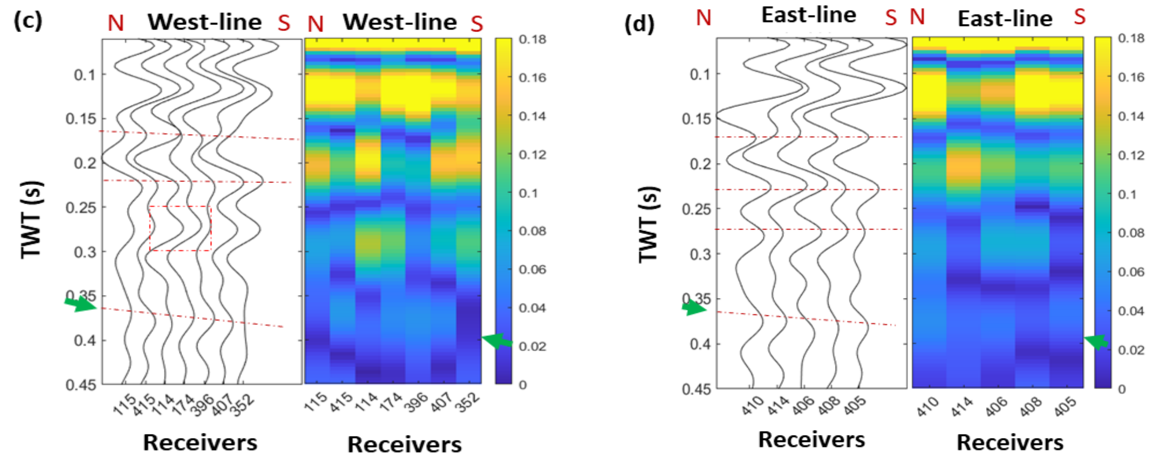

Figure 3.12: Blast autocorrelations (two-month survey) of 40 stacked shots in two frequency ranges for the western and eastern lines and their envelopes. A high-frequency range of 15–58 Hz was used in (a and b) and a low-frequency range of 6–20 Hz in (c and d). Green arrows indicate reflections assumed to correspond to bedrock interfaces. Dotted horizontal lines indicate the continuous reflectors, and rectangle indicates the interpreted vein-related reflection features.

In the autocorrelation results obtained for the natural earthquake at higher frequencies (5–38 Hz; Figure 3.13a and 3.13b), we extracted three clear reflections at 0.12, 0.16, and 0.21 s TWT, roughly corresponding to the shallow reflectors obtained from the blast events. We also observed two more reflections at 0.25 and 0.34 s TWT. In the lower frequency range (2–20 Hz) results, we obtained similar reflections to those obtained with blast signals, but the amplitude and inter-station coherency were larger for the 0.34 s TWT reflection in the earthquake results (Figure 3.13c and 3.13d). The reflection at 0.34 s TWT appeared to be inclined to the south. The earthquake-derived reflections at around 0.25 s in both frequency ranges showed remarkably high-amplitude and were quite discontinuous at stations 114, 410 and 414 (red rectangle in Figure 3.13). Similar reflections were observed in the low-frequency 6-20 Hz blast results at station 114 (red rectangle in Figure 3.12c) and in the data from the second survey (red rectangles in Figure 3.17a; see next subsection) that may be related to vein deposits (see Discussion).

Natural earthquake

(High-frequency range [5-38 Hz])

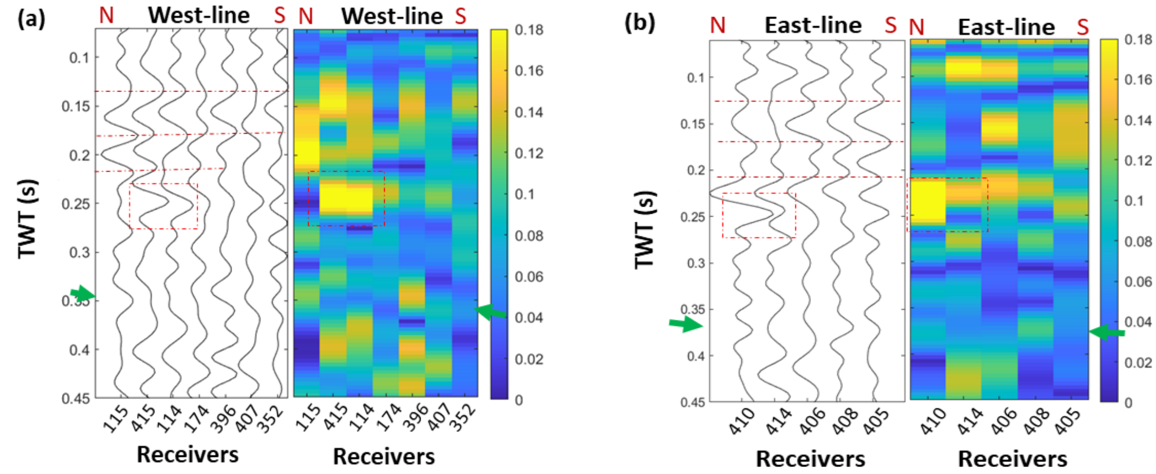

(Low-frequency range [2-20 Hz])

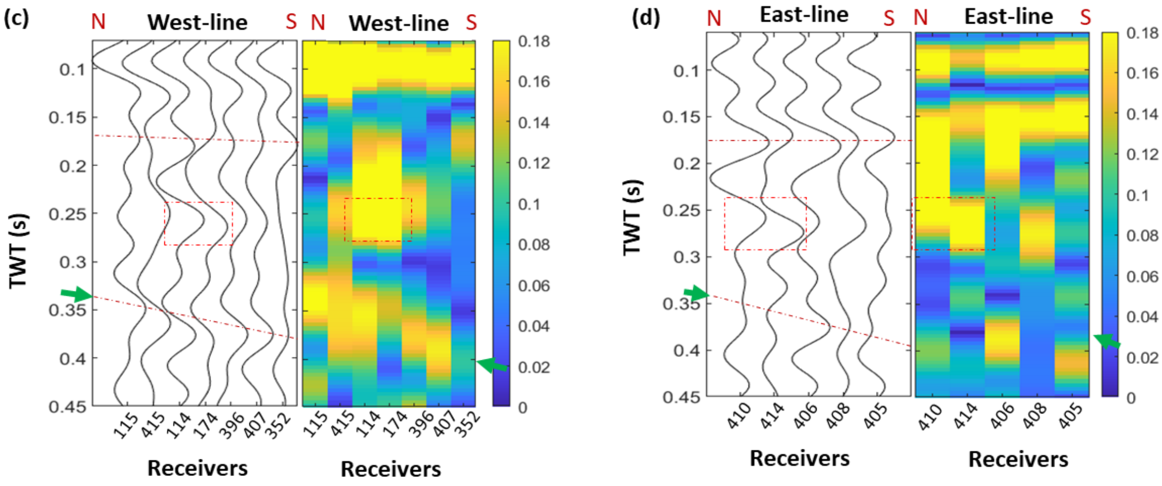

Figure 3.13: Natural earthquake autocorrelations (two-month survey) in two frequency ranges for the western and eastern lines and their envelopes. A high-frequency range of 5–38 Hz was used in (a and b) and a low-frequency range of 2–20 Hz in (c and d). Green arrows indicate reflections assumed to correspond to bedrock interfaces showing the dipping trend to the south direction especially in the west line. Dotted horizontal lines indicate the continuous reflectors, and rectangle indicates the interpreted vein-related reflection features.

The autocorrelations obtained by stacking 3 hours of ambient noise of higher frequencies (5–30 Hz) showed three fair reflections at 0.12, 0.16, and 0.2 s TWT (Figure 3.14a and 3.14b). These reflection arrivals are consistent with those observed in the blast and natural earthquake-derived results at higher frequencies, despite of a negligible time difference of ∼0.02 s. The slight difference may be due to the use of different frequency bands for each seismic source. In the case of lower frequency range (2–20 Hz), two low-amplitude reflections were roughly distinguished at 0.27 and 0.36 s TWT (Figure 3.14c and 3.14d). In general, the envelope sections calculated for the lower frequency ranges showed broader reflection amplitudes than those calculated for the higher frequency ranges for each seismic data type (Figures 3.12–3.14).

Ambient noise

(High-frequency range [5-30 Hz])

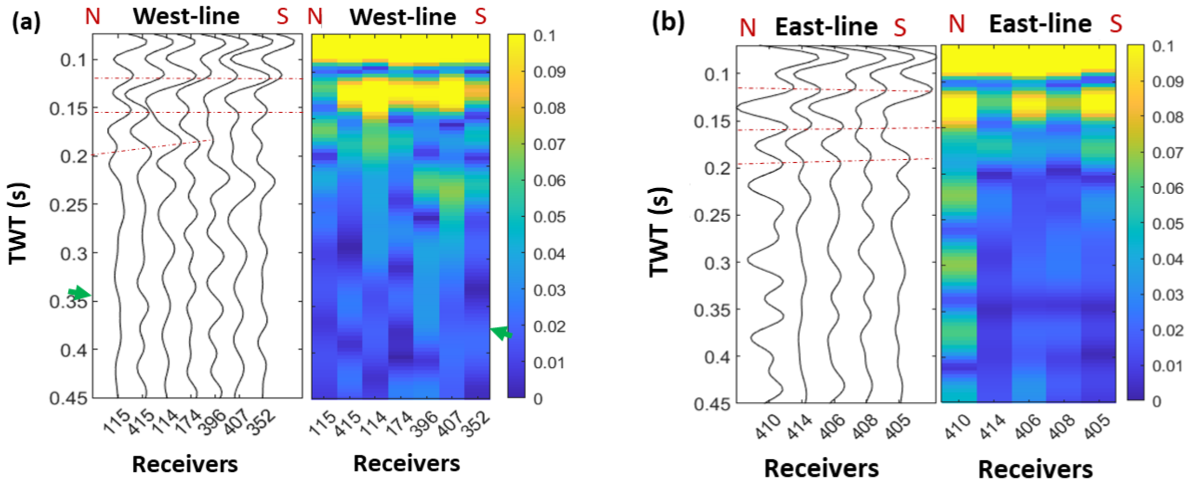

(Low-frequency range [2-20 Hz])

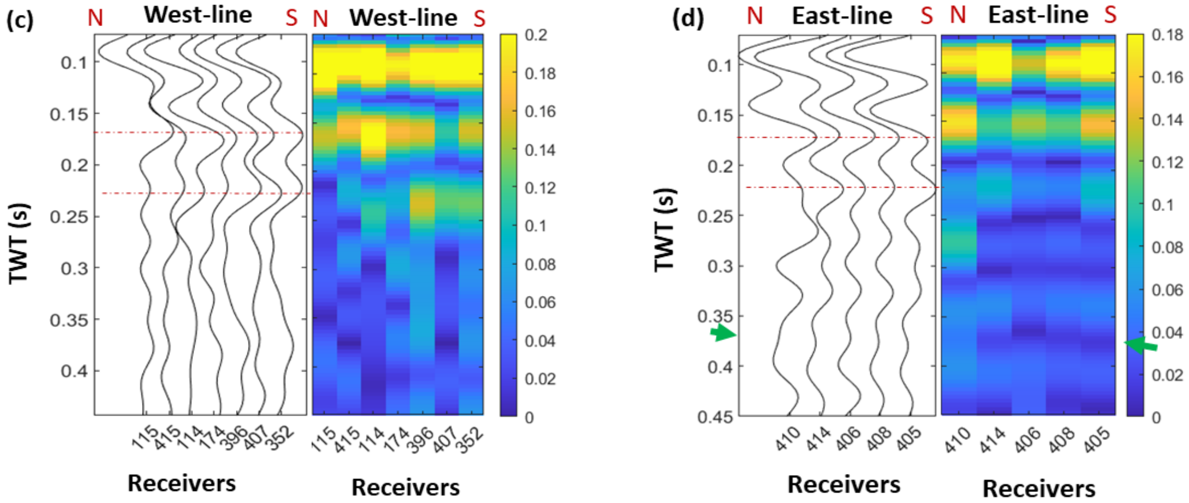

Figure 3.14: Three-hour stacked ambient noise autocorrelations (two-month survey) in two frequency ranges for the western and eastern lines and their envelopes. A high-frequency range of 5–30Hz was used in (a and b) and a low-frequency range of 2–20 Hz in (c and d). Green arrows indicate reflections assumed to correspond to bedrock interfaces. Dotted horizontal lines indicate the continuous reflectors.

Of the three source types, the blast and earthquake reflection arrival times were mostly continuous among the different stations (Figures 3.12-3.16). The blast reflection results showed enhanced amplitude, especially in the higher frequency range. The higher signal-to-noise ratio (SNR) of the natural earthquake at lower frequencies enabled us to obtain more reflections than with the blast-source autocorrelations in the low-frequency range (e.g., the reflection at ~0.35 s; see Discussion). The ambient noise-derived reflections were fair and consistent with the results of blast and earthquake in the earlier arrival times. On the other hand, weak and unclear reflections were obtained in later parts of the noise-derived reflection profiles. When comparing the single-shot autocorrelation images with those of the stacked shots, we observed clearer high-amplitude reflections in some parts of the autocorrelation profiles for unstacked single shots. We discuss the effect of stacking including stationary phase contribution (see Discussion). This field experiment demonstrates that clear results can be obtained by using a smaller number of clear blast events. However, the limited number of seismometers used in this first survey precluded 3D imaging of the subsurface geological structure. Therefore, we acquired a limited number of blast events using many seismometers in the second survey.

The correlation between reflections in autocorrelations from the blast and earthquake was further investigated. The observed reflections in the low- and high-frequency ranges of both blasts and earthquake were plotted side-by-side for the same stations (Figures 3.15a, 3.15b, 3.16a and 3.16b). The peaks of blasts and earthquake-derived reflections were picked and plotted in Figures 3.15c and 3.16c for low- and high-frequency ranges, respectively. To pick the peaks, we set the search range of arrival times for each reflection as shown in the shaded portions in Figures 3.15, 3.15b, 3.16a and 3.16b. The reflections were ordered 1 to 3 (Figure 3.15c and 3.16c) as from the earlier (shallower) observed reflectors to later ones. Despite the difference in characteristics (energy and location) of the used seismic sources (blast or earthquakes), the arrival times of each reflection were basically consistent. In the higher frequency range, we observed the small difference of the arrival times between blast and earthquake. This can be caused by the difference in the applied frequency filter ranges 15-58 for blast and 5-38 Hz for earthquake signals (Figures 3.16). On the other hand, the reflections in the low-frequency ranges of for the blast and earthquake are more consistent among both event reflections at about 0.17, ~ 0.25 and 0.36 s TWT (Figures 3.15). Because of the small difference between the used low-frequency filters 6-20 Hz for blasts and 2-20 Hz for earthquake, the reflection arrival times are close to each other for the corresponding reflections.

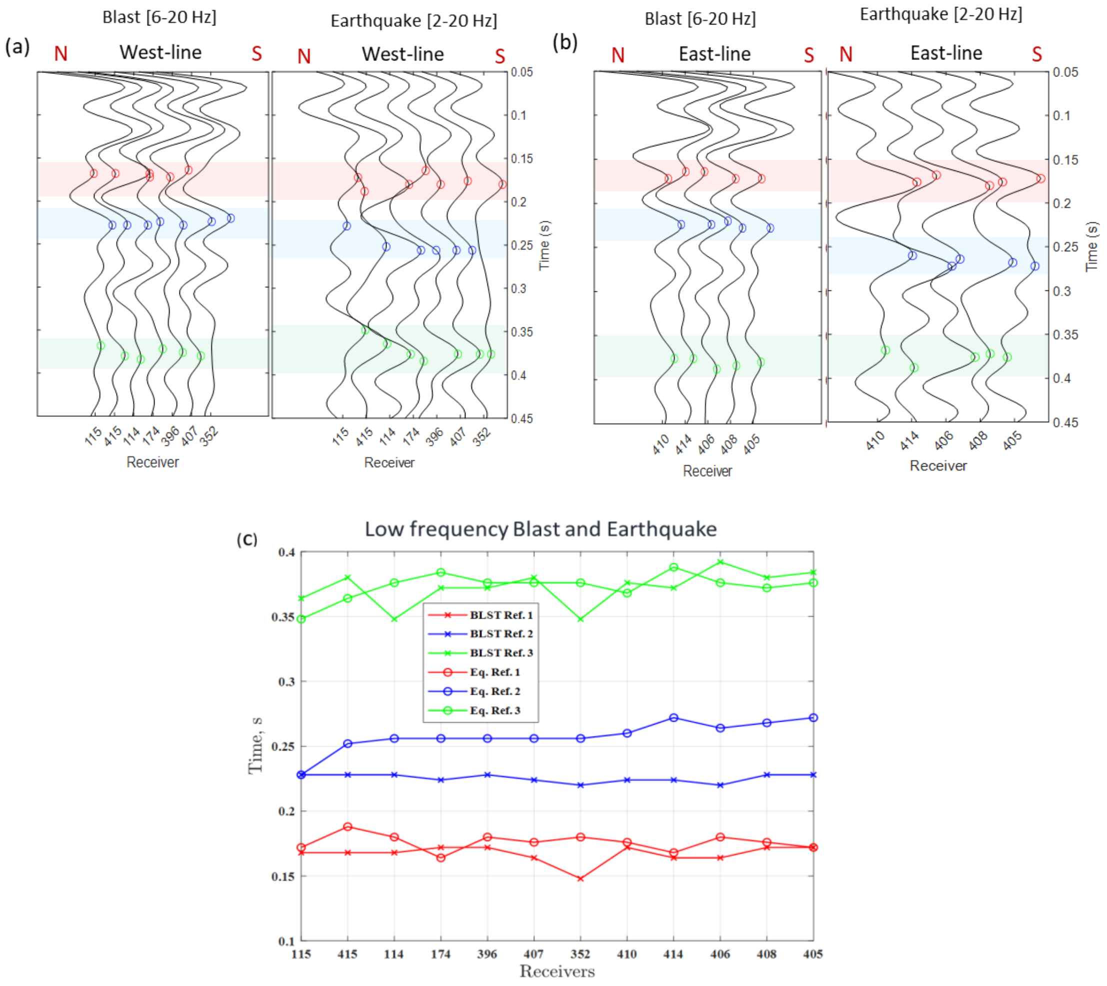

Figure 3.15: The autocorrelations of the blast and earthquakes for the low-frequency filters in the (a) west profiles and (b) east profiles. The peaks of the observed reflections from the early to late arrivals times (1 to 3) are plotted in the panel (c). The crosses and circles represent the reflections from blast and earthquake-derived reflections, respectively.

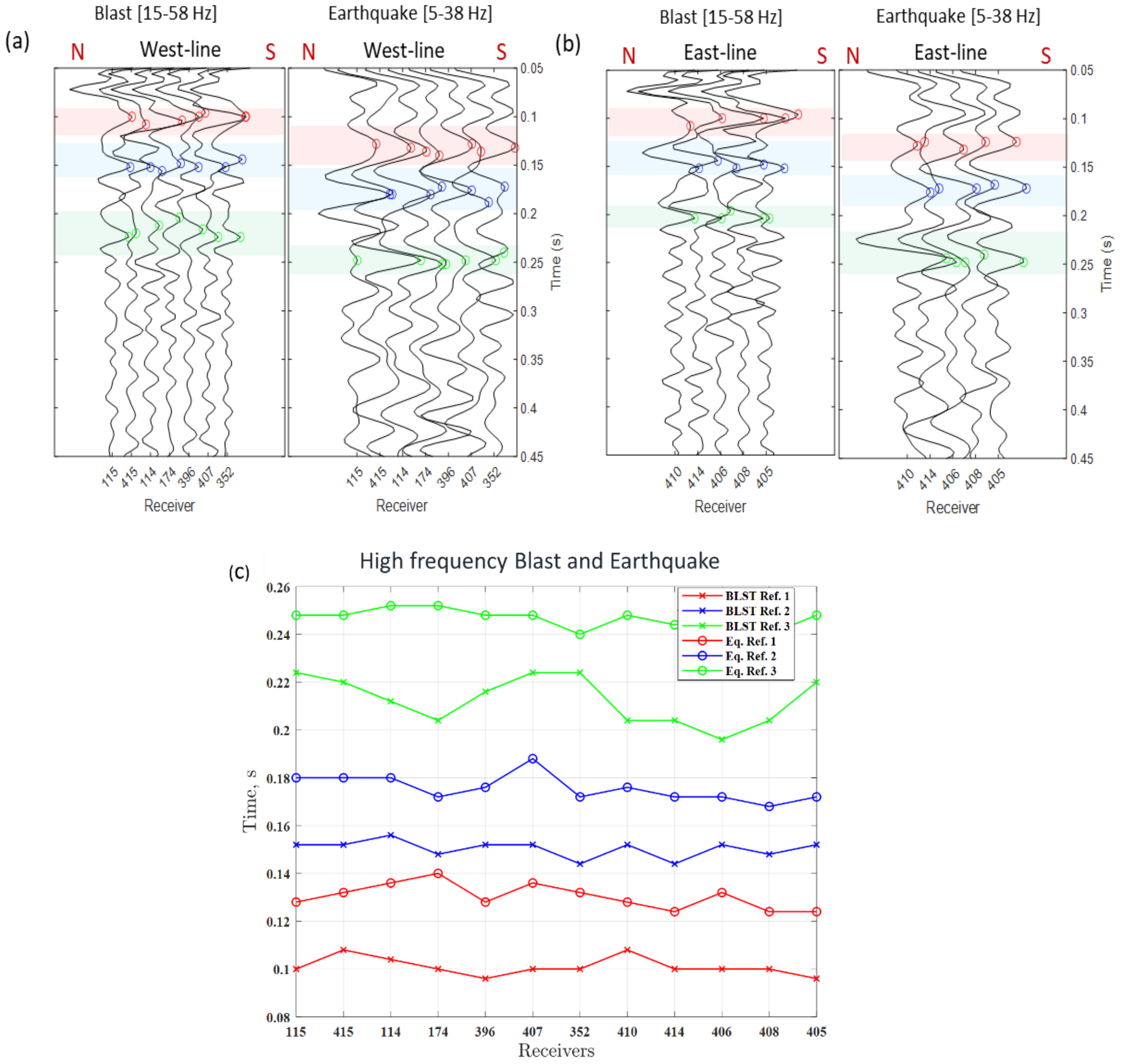

Figure 3.16: The autocorrelations of the blast and earthquakes for the high-frequency filters in the (a) west profiles and (b) east profiles. The peaks of the observed reflections from the early to late arrivals times (1 to 3) are plotted in the panel (c). The crosses and circles represent the reflections from blast and earthquake-derived reflections, respectively.

3.5.2 Autocorrelations using single-day dense seismometer data (second survey)

Figure 3.17 shows the reflection profiles calculated by autocorrelation analysis of the third of three blast shots recorded by the 33-seismometer array (Figure 3.1b). We used a single blast shot for this analysis because, depending on the amplitude and frequency of the signals, one high SNR in a wider frequency range and closer to the stationary phase zones is sufficient to obtain high-resolution seismic autocorrelation images (see Discussion). In Figure 3.17, the autocorrelation profiles at each station are projected along the NW–SE seismic line (black line in Figure 3.1b). The reflection profile shows horizontally coherent reflections indicating that it successfully imaged the lithological boundaries at high-resolution. We identified coherent reflections at 0.14, 0.21, 0.35, and 0.44 s TWT. In the second survey, some stations (173, 442, 114, 172 and 410; Figure 3.17a) showed reflections with negative polarity at about 0.23 s that are consistent with low-frequency (6-20 Hz) results of the first survey blast at about 0.2 s (station 114; Figure 3.12c), and both (low- and high-) frequency ranges of the earthquake-derived results between 0.2 and 0.23 s arrival times (stations 114, 115, 410; Figure 3.13).

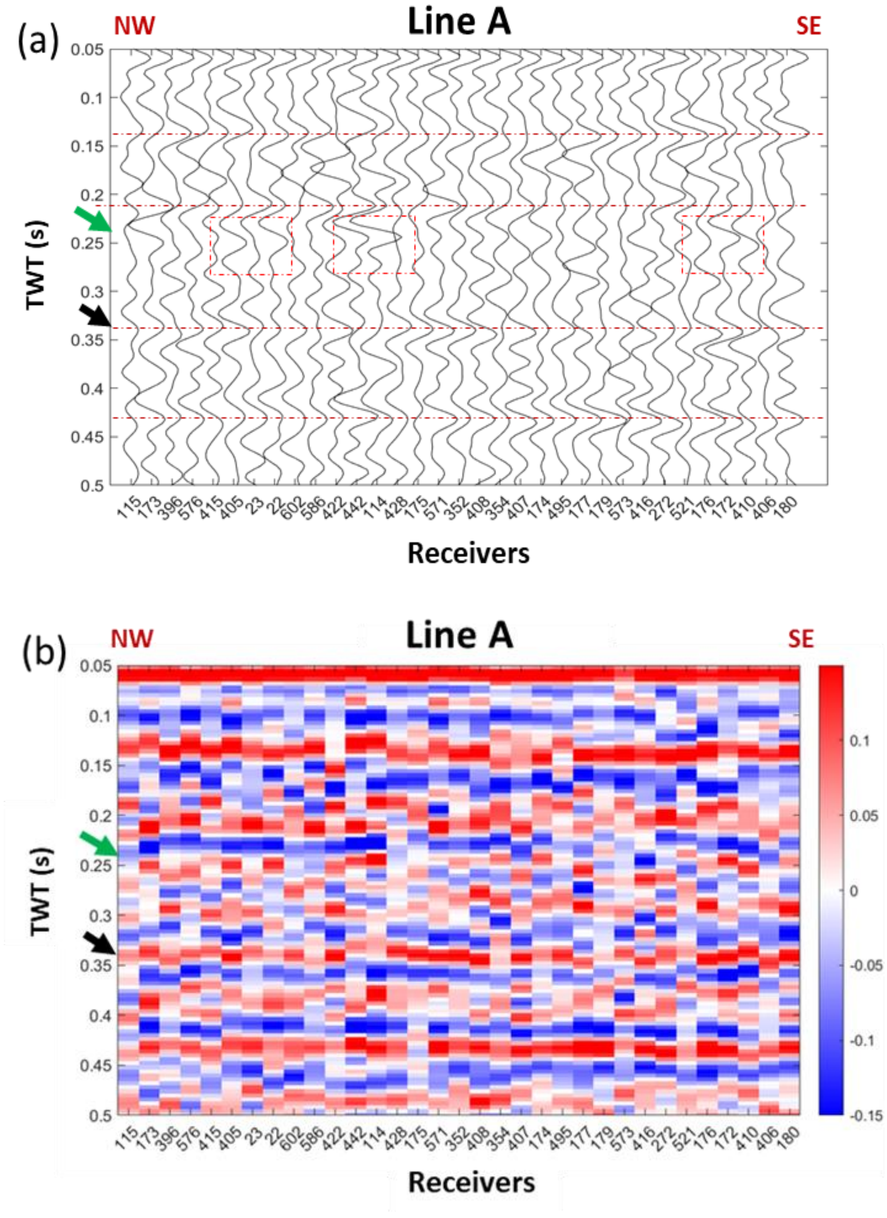

Figure 3.17: (a) Observed autocorrelations (single-day survey) and (b) their amplitudes projected onto line (A) in Figure 1b. Green arrows indicate the time-depth slice used in Figure 3.18b and black arrows indicate the time-depth slice used for the extracted surface in Figure 3.18c. The frequency range used in this survey was 12–40 Hz. The path distance from the southeastern-most station (180) to the northwestern-most station (115) was about 1200 m. Dotted horizontal lines indicate the continuous reflectors.

To map the 3D distribution of the reflections, we constructed a pseudo-3D autocorrelation reflection time-amplitude model (Figure 3.18a) by interpolating autocorrelations between stations. This 3D model shows the reflections of lithological boundaries and their lateral variations and continuities. As an example, we extracted the time slice at 0.24 s TWT in Figure 3.18b, corresponding to the arrival indicated by the green arrow in Figure 3.17. While Figure 3.18c shows the spatial distribution of the arrival times from dominant reflectors at ~0.35 s TWT (black arrows in Figures 3.17 and 3.18a). We succeeded in extracting 3D geometrical information (e.g., lateral depth and thickness variations) for shallow geological boundaries by using the blast signals.

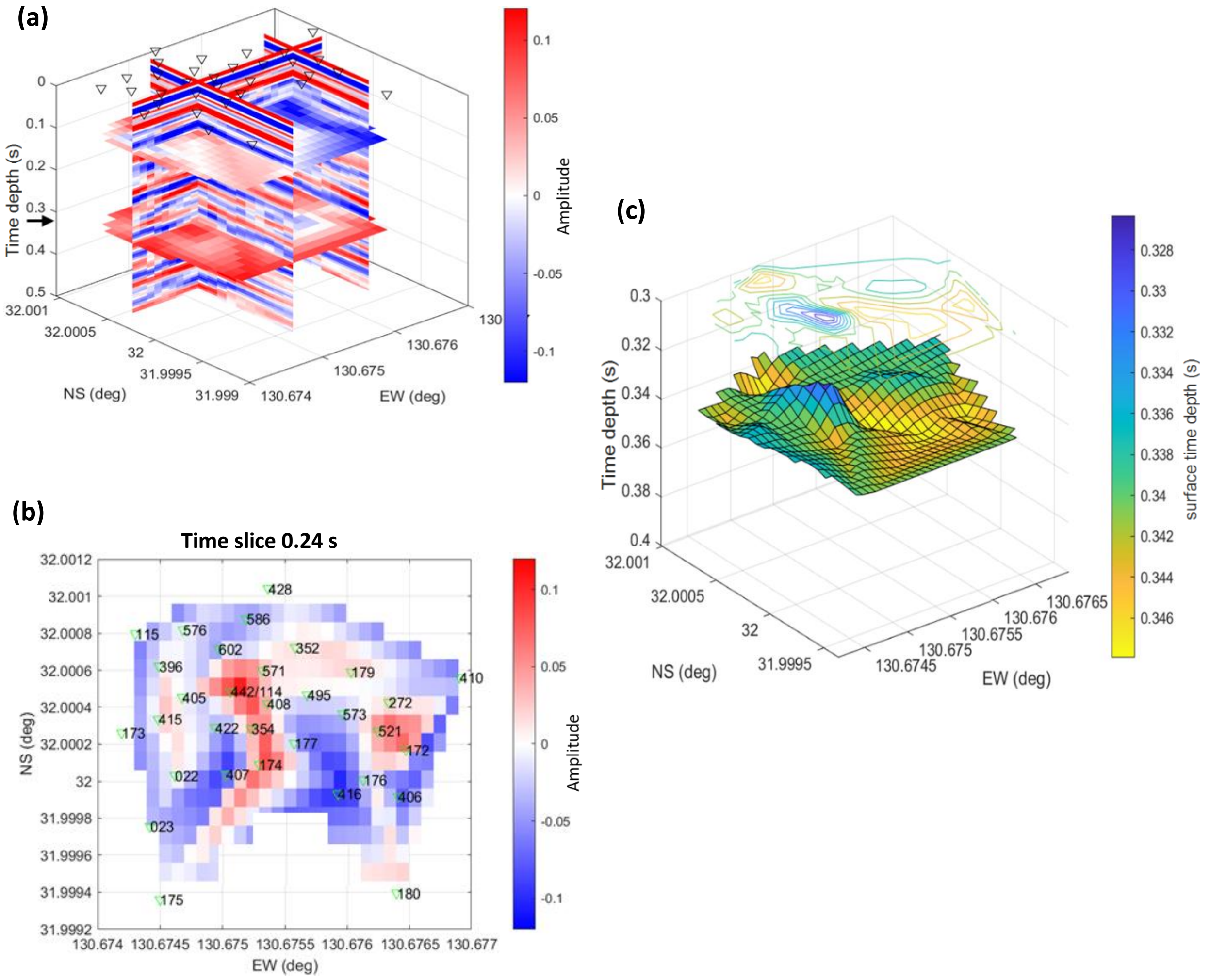

Figure 3.18: (a) Pseudo-3D autocorrelation reflection time-amplitude model constructed by interpolation of the calculated autocorrelations of the 33 stations used in the single-day survey. (b) Time slice at 0.24 s TWT showing possible ore-vein deposits. The plotted numbers and triangles correspond to the seismic stations. (c) A 3D projection of a reflection that may correspond to a lithological interface and its contour map, viewed at 0.3–0.4 s TWT vertically and 0.002° × 0.0015° laterally. This interface was extracted from the observed 3D autocorrelation reflection model (black arrows in panel (a) and Figure 3.17).

3.6 Discussion

In this study, we demonstrated the potential of seismic autocorrelations using blast signals as their source to constrain shallower lithological boundaries compared to conventional earthquake and ambient noise signals. Since the blast events included high-frequency and high-amplitude signals (Figure 3.3), the blast source is useful for extracting high-resolution reflection profiles (Figures 3.12, 3.17 and 3.18). In contrast, results using the earthquake source showed higher amplitudes at later arrival times in the low-frequency range (Figures 3.4 and 3.13). Although the observed reflections from ambient noise were consistent with those from the blast and earthquake in high-frequencies, the ambient noise results were the worst for the shallow formation imaging since the reflection signals had limited amplitude, included abundant low-frequency noise, and were easily influenced by localized noise (Figures 3.5 and 3.14).

One of the merits of using blast data over natural earthquake events is that blast events occur at scheduled times. Indeed, only a single natural earthquake large enough for autocorrelation analysis occurred during our two-month survey. Furthermore, the ambient noise data required several hours of stacking and additional signal processing to obtain only unclear shallow reflections. Therefore, the use of blast events as the source in autocorrelation studies is more effective for constructing lithological boundaries during a short survey period, such as second survey (Figure 3.18).

Our study also demonstrates that only one blast shot with sufficiently high signal-to-noise ratio (SNR) and frequency components can provide high-resolution autocorrelation reflections.

Several factors influence the quality of the shots (e.g., source depth, offset and source energy). Although the source depth and offset are important factors to accurately extract reflection signals beneath stations from stationary phase zones, such information is difficult to identify in our cases. We therefore rely on the SNR computed for each blast signal to evaluate separately the quality of each shot. To evaluate the impact of stacking, possible stationary phase contributions and SNR of blasts, the influence of the stationary phase contributions were investigated by assembling autocorrelations before stacking and comparing with the stacked one.

Figure 3.19a and 3.19b show the assembly of the 40 autocorrelations for the station 114 where the potential vein deposits at the ~0.25 s reflection (Figures 3.12c and 3.13). After stacking 40 autocorrelations, several reflections are emphasized (red lines in Figure 3.19a and 3.19b), probably associated with the stationary phase as stacking process attenuates incoherent signals or noise while boosting stationary signals (Schuster, 2009; Ito and Shiomi, 2012; Oren and Nowack, 2017; Mroczek and Tilmann, 2021; Aldawood et al., 2019, 2022). Some traces show high-amplitude that was also observed in the stacked trace, while some shots did not show signals at arrival times of high-amplitude in the stacked traces (Figures 3.19a and 3.19b). The unstable phases (peaks and troughs) may indicate either the source locations far from the stationary phase zone or the weak signals of the reflected wave from blasts. Evaluation by the SNR can rule out the shots with weak signals as the traces with the weak signals among the highlighted reflections (Figure 3.19a and 3.19b) have much lower SNR in the Figure 3.19c, such as shots number 2, 13, 24, 34, and 37. Reduced resolution of reflection traces were observed also at the shot number 28 and 29 which exhibited low SNR below 20 Hz (Figure 3.19c).

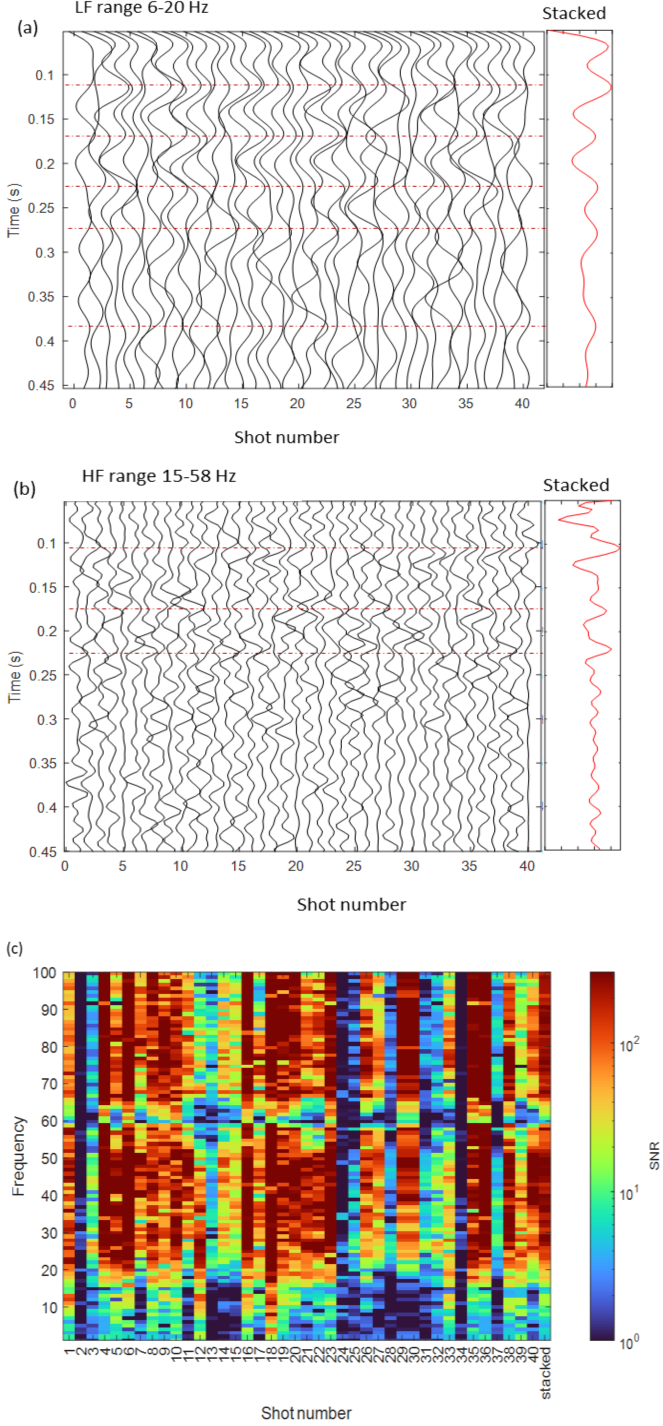

Figure 3.19: Autocorrelation of single station 114 (during the first survey) assembling 40 blast shots prior to stacking and the stacked waveform, showing the effect of stacking and stationary phase (a) low-frequency range 6-20 Hz and (b) high-frequency range 15-58 Hz. (c) SNR for all used 40 shots at station 114 and for the stacked waveform.

In the second survey, the number of available blasts is only three. Although the third blast shows large SNR and clear horizontally coherent reflection in the resulting autocorrelations (Figure 3.20), it is difficult to evaluate the stationary phase contribution. Therefore, we compare the reflections with those from the first survey with 40 shot stacking, which could be close to the stationary phase. The results of stacked traces of the first survey showed high-amplitude reflections (Figure 3.12, 3.19a and 3.19b) at similar arrival times with those from the third shot in the second survey at ~0.14, 0.21 and 0.35 s (Figures 3.17 and 3.20l). Thus, we interpret the third shot might be close to the stationary phase and define the optimum blast for calculating the autocorrelation functions of the second survey. To avoid any negative influence from stacking and obtain better results, we used only the third shot without stacking with any other shots. Because the stacking of high-amplitude shots with lower amplitude shots may reduce the resolution of reflections in the autocorrelation images. Only a single optimum (high-amplitude and frequency in wide frequency range and closer to stationary zone) shot is likely to be sufficient for obtaining high-resolution seismic autocorrelation images of shallow subsurface lithological structures.

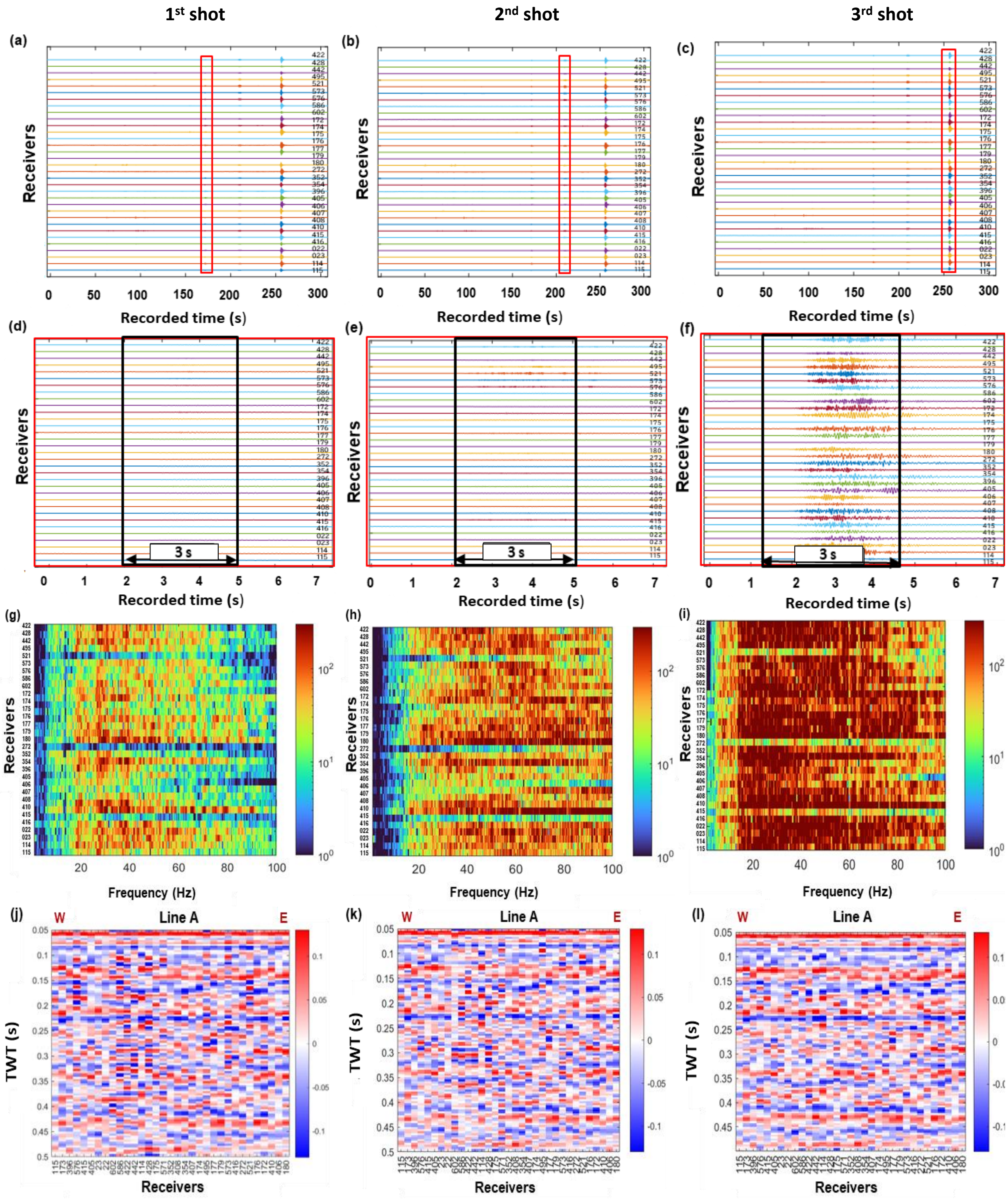

Figure 3.20: The first three shots recorded by the 33 stations during the single-day survey: (a-c) raw data showing the shots in a 300-s time interval, (d-f) close-ups of the 3-s time intervals used for autocorrelation function calculations, (g-i) calculated SNRs shown in the frequency domain, and (j-l) autocorrelation results sampled by filtering at 12–40 Hz.

Based on the results shown in Figures 3.12–3.14, wider and higher frequency bands can be used to produce sharp, high-amplitude reflections at early arrival times (shallower depths), whereas narrower, lower frequency bands can be used to extract relatively later (deeper) reflections. Therefore, a combined interpretation using autocorrelations from different frequency ranges is more effective in cases such as our first survey. The reflections obtained from the autocorrelation results of the first survey using three seismic sources (blast, earthquake, and ambient noise) were at about 0.11, 0.15, 0.2, and 0.34 s two-way travel time (TWT) (Figures 3.12–3.14). The clear reflections of the 2D and 3D high-resolution images in Figures 3.17 and 3.18 demonstrate the potential of the autocorrelation technique using mine blasts with dense station arrays; we observed higher-resolution reflections than those of the first survey. The four clear, high-amplitude reflectors at 0.14, 0.2, 0.35, and 0.44 s TWT imaged in the second survey (Figure 3.17) are highly consistent with the reflections imaged in the first survey.

For interpretation purposes, to estimate the depth of the geological boundaries from the calculated autocorrelation profiles, we must approximately assume the seismic velocities of the rock units in the area. The P-wave velocities of the different rock types in this area measured from the drill cores and drift-way walls by the Schmidt hammer test (Okada et al., 2018) range from 2500 to 3500 m/s. By assuming a constant P-wave velocity of 3000 m/s, we obtained the corresponding depths of the reflection boundaries at 0.11, 0.14, 0.2, 0.35, and 0.44 s to be 165, 210, 300, 525, and 660 m, respectively. We interpret the observed horizontally consistent reflections to correspond to the velocity contrasts at the lithological boundaries between, from top to bottom, the upper volcanic welded tuff, the Hishikari lower andesite lava and tuff breccia and lower sedimentary rocks and metamorphosed rocks of the Shimanto supergroup.

The three reflections at ~0.14, 0.2, 0.35 s (Figures 3.12, 3.13, 3.17 and 3.18) could be consistent with the three lithological boundaries identified in the previous resistivity surveys, that were interpreted as altered and unaltered volcanic rocks and basement (Okada, 1995,2000). For the later reflections, the autocorrelation results from the earthquake in the first survey showed the clear dipping trend toward the south at the arrival time (0.34–0.38 s) in the low-frequency (2-20 Hz: Figures 3.13c and 3.13d). Observed gravity anomalies and the geological setting in the first survey area indicate structural uplift of the basement rocks in the north and/or thickening of the volcanic intrusive flow into the lower tuff sequence in the south (Ishihara et al., 1986; Izawa et al., 1990, 1993; Uto et al., 2001; Okada, 1995, 2000). Therefore, this reflection (at 0.34–0.38 s) may indicate the bedrock interface between the Shimanto supergroup and overlying volcanic rocks, which is likely to be inclined to the south in the first survey area. In the second survey, the lateral distribution of the assumed bedrock reflection (at ~0.35 s TWT, extracted from the 3D model in Figure 3.18a) is shown in Figure 3.18c.

Our results also provide insights for mineral exploration. Indeed, we may identify relatively thin fractures based on the high-resolution seismic imaging performed during the second survey. The observed significant reflection with negative polarity at some stations in the first survey at 0.2 s and 0.23 s TWT of the blast and earthquake respectively (Figures 3.12c and 3.13) were consistent with those at some stations of the second survey at 0.23 s arrival time (Figure 3.17). These reflections may indicate the presence of thin fractures (fissures) which decreased in acoustic impedance. Furthermore, the red rectangles in Figures 3.12c and 3.13, and the green arrows and red rectangles in Figure 3.17 (~0.25 s) could highlight the laterally discontinuous high-amplitude reflections that may correspond to fissures filled with vein-ore deposits. The results of the Schmidt hammer test measured the rebound values of the different rock units, including the quartz-adularia associated with the vein system of this field (Okada et al., 2018). The large variation of the measured P-wave velocities indicates a high impedance contrast between the veins deposits and surrounding rocks that can produce seismic reflection responses. Therefore, the observed discontinuous reflections at ~0.25 s could correspond to the potential ore zones from the overlapping of the IP anomalies (high-chargeability) with low resistivity (Okada, 1995, 2000). Sekine et al. (2002) reported the results of near-surface drilling by Sumitomo Metal Mining (SMM): the vein-ore deposits in this mine reach 150 cm thickness, strike N30E to N70E, dip steeply to the north between 70° to 90°, and are present over at least 700 m along strike and over a vertical range of 100 m. In Figure 3.18b, we extracted a time-depth slice from the heterogeneous reflections to illustrate possible ore deposit veins trending N–S.

As described above, the estimated reflection profiles could be related to the lithological boundaries identified by the previous geophysical surveys (gravity, resistivity, and IP) (Okada; 1995, 2000). Compared to other non-seismic surveys, our seismic autocorrelation method using high-frequency blasts has the large potential to reveal higher resolution subsurface imaging including the potential zones of ore deposits down to the bedrock. Because the lateral resolution of our approach depends on the density of seismometers, it is difficult to investigate large areas in high-resolution. However, once potential areas are determined by other geophysical methods, high-resolution subsurface structure can be estimated by our approach as shown in the second survey. Considering survey cost, time and quality of the results, the seismic autocorrelation method based on blast signals can be a new cost-effective approach to explore mineralization areas in high-resolution.

3.7 Conclusions

Because seismic interferometry based on autocorrelation analysis of natural earthquake- or ambient noise-derived seismic signals has limited resolution at shallow depths, we developed an approach using artificial mine explosions as a seismic source. By autocorrelation analysis of the blast signal, we extracted P-wave reflection profiles as well as 3D structural information from the mine explosions. Because the blast signals contain high-frequency components over a wide frequency range, the resulting autocorrelation represents shallow lithological boundaries. The dense station spacing used during our single-day survey enabled us to image lithological boundaries from the surface to around 500 m depth at very high lateral and vertical resolution using only a single blast signal. Thus, exploiting mining blasts as seismic sources can be an effective method for exploring mining sites, including ore deposits, within a short time and without the need for additional artificial sources. We interpret the imaged lithological boundaries to be the interfaces between, from top to bottom, the upper volcanic welded tuff, the Hishikari lower andesite lava and tuff breccia and the lower sedimentary rocks of the Shimanto supergroup.

3.8 References

Aldawood, A., Almarzoug, M., Silvestrov, I., Bakulin, A. (2022) ‘Characterizing shallow subsurface using 3D seismic while drilling with a downhole pilot’, The Leading Edge, 41(5), pp. 304–312. doi: 10.1190/tle41050304.1.

Aldawood, A., Silvestrov, I. and Bakulin, A. (2019) ‘Virtual Shear-Wave Source Delivers a Reliable S-Wave Velocity Model for VSP Imaging’, in 81st EAGE Conference and Exhibition 2019. European Association of Geoscientists and Engineers, pp. 1–5. doi: 10.3997/2214-4609.201900695.

Becker, G. and Knapmeyer-Endrun, B. (2018) ‘Crustal thickness across the Trans-European Suture Zone from ambient noise autocorrelations’, Geophysical Journal International, 212(2). doi: 10.1093/gji/ggx485.

Bensen, G. D. et al. (2007) ‘Processing seismic ambient noise data to obtain reliable broad-band surface wave dispersion measurements’, Geophysical Journal International, 169(3). doi: 10.1111/j.1365-246X.2007.03374.x.

Chimoto, K. and Yamanaka, H. (2019) ‘S-Wave velocity structure exploration of sedimentary layers using seismic interferometry on strong motion records’, Exploration Geophysics, 50(6), pp. 625-633. doi: 10.1080/08123985.2019.1654835.

Chimoto, K. and Yamanaka, H. (2020) ‘Tuning S-wave velocity structure of deep sedimentary layers in the Shimousa region of the Kanto Basin, Japan, using autocorrelation of strong-motion records’, Bulletin of the Seismological Society of America, 110(6), pp. 2882-2891.

doi: 10.1785/0120200156.

Claerbout (1968) ‘Synthesis of a Layered Medium from its Acoustic Transmission Response’, Geophysics, 33(2), pp. 264–269.

Gorbatov, A., Saygin, E. and Kennett, B. L. N. (2013) ‘Crustal properties from seismic station autocorrelograms’, Geophysical Journal International, 192(2), pp. 861–870. doi: 10.1093/gji/ggs064.

Heath, B.A., Hooft, E.E.E., Toomey, D.R. (2018) Autocorrelation of the seismic wavefield at Newberry Volcano: Reflections from the magmatic and geothermal systems. Geophys Res Lett 45:2311–2318. https://doi.org/10.1002/2017GL076706

Ishihara, S., Sakamaki, Y., Sasaki, A., Teraoka, Y., Terashima, S. (1986) ‘Role of the basement in the genesis of the Hishikari gold-quartz vein deposit, southern Kyushu, Japan.’, Mining Geol., 36, pp. 495–509.

Ito, Y. and Shiomi, K. (2012) 'Seismic scatterers within subducting slab revealed from ambient noise autocorrelation', Geophys. Res. Lett., 39(19), L19303, doi:10.1029/2012GL053321.

Izawa, E. Urashima, Y., Ibaraki, K., Suzuki, R., Yokoyama, T., Kawasaki, K., Koga, A., Taguchi, S. (1990) ‘The Hishikari gold deposit: High grade epithermal veins in Quaternary volcanics of southern Kyushu, Japan. ’, Geochem. Explor., 36, pp. 1–56.

Izawa, E., Kurihara, M. and Itaya, T. (1993) ‘K-Ar ages and initial Ar isotopic ratio of adularia-quartz veins from the Hishikari gold deposit, Japan. ’, Resource Geol. Spec, Issue, 14, pp. 63–69.

Kennett, B. L. N., Saygin, E. and Salmon, M. (2015) ‘Stacking autocorrelograms to map Moho depth with high spatial resolution in southeastern Australia', Geophysical Research Letters, 42(18). doi: 10.1002/2015GL065345.

Mroczek, S. and Tilmann, F. (2021) 'Joint ambient noise autocorrelation and receiver function analysis of the Moho', Geophysical Journal International, 225(3). doi: 10.1093/gji/ggab065.

Nakahara, H. (2006) 'Theoretical background of retrieving Green's function by cross-correlation: one-dimensional case', Geophys. J. Int., 165, pp. 719–728.

Okada, K. (1995) 'Geophysical exploration for epithermal gold deposits: Case studies from the Hishikari Gold Mine, Kagoshima, Japan', Exploration Geophysics, 26(2–3). doi: 10.1071/EG995078.

Okada, K. (2000) 'Geophysical exploration at Hishikari gold mine, Kagoshima, Japan', The Leading Edge, 19(7). doi: 10.1190/1.1438708.

Okada, K., Minami, Y. and Ono, M. (2018) 'Microtremor Survey for Exploration Targetting Epithermal Vein Systems at the Hishikari Gold Mine, Kagoshima, Japan', in 2nd Conference on Geophysics for Mineral Exploration and Mining. European Association of Geoscientists and Engineers, pp. 1–5. doi: 10.3997/2214-4609.201802740.

Oren, C. and Nowack, R. L. (2017) 'Seismic body-wave interferometry using noise autocorrelations for crustal structure', Geophysical Journal International, 208(1). doi: 10.1093/gji/ggw394.

Romero, P. and Schimmel, M. (2018) 'Mapping the Basement of the Ebro Basin in Spain With Seismic Ambient Noise Autocorrelations', Journal of Geophysical Research: Solid Earth, 123(6). doi: 10.1029/2018JB015498.

Saygin, E., Cummins, P. R. and Lumley, D. (2017) 'Retrieval of the P wave reflectivity response from autocorrelation of seismic noise: Jakarta Basin, Indonesia', Geophysical Research Letters, 44(2). doi: 10.1002/2016GL071363.

Schuster, G. T. (2009) Seismic Interferometry. Cambridge University Press. doi: 10.1017/CBO9780511581557.

Sekine R., Izawa E. and Watanabe K. (2002) 'Timing of Fracture Formation and Duration of Mineralization at the Hishikari Deposit, Southern Kyushu, Japan', RESOURCE GEOLOGY, 52(4), pp. 395–404.

Suemoto, Y., Ikeda, T., and Tsuji T. (2020) Temporal variation and frequency dependence of seismic ambient noise on Mars from polarization analysis, Geophysical Research Letters, 47(13), e2020GL087123, doi:10.1029/2020GL087123.

Taylor, G., Rost, S. and Houseman, G. (2016) 'Crustal imaging across the North Anatolian Fault Zone from the autocorrelation of ambient seismic noise', Geophysical Research Letters, 43(6). doi: 10.1002/2016GL067715.

Tibuleac, I. M. and von Seggern, D. (2012) 'Crust-mantle boundary reflectors in Nevada from ambient seismic noise autocorrelations', Geophysical Journal International, 189(1). doi: 10.1111/j.1365-246X.2011.05336.x.

Uto, T., Imai, A. and Yamato, Y. (2001) 'Horizontal Strain Rate in Relation to Vein Formation of the Hishikari Gold Deposits, Southern Kyushu, Japan', Resource Geology, 51(1), pp. 7–18. doi: 10.1111/j.1751-3928.2001.tb00077.x.

Wang, C., Tauzin, T., Pham, T-S., Tkalčić, H. (2020) 'On The Efficiency of P -Wave Coda Autocorrelation in Recovering Crustal Structure: Examples From Dense Arrays in the Eastern United States', Journal of Geophysical Research: Solid Earth, 125(12). doi: 10.1029/2020JB020270.

Wapenaar, K. (2004) 'Retrieving the Elastodynamic Green's Function of an Arbitrary Inhomogeneous Medium by Cross Correlation', Physical Review Letters, 93(25). doi: 10.1103/PhysRevLett.93.254301.

Zhang, Y., Li, Y. E. and Ku, T. (2021) 'Soil/rock interface profiling using a new passive seismic survey: Autocorrelation seismic interferometry', Tunnelling and Underground Space Technology, 115, p. 104045. doi: 10.1016/j.tust.2021.104045.

Chapter 4

Summary and conclusion

4.1 Summary

In this dissertation, the reflected seismic body waves were utilized to develop methods of imaging and mapping for new applications of exploring unconventional geophysical targets. These methods were based on the seismic attributes for processing and better visualization of the complex deep structures and enhancing the subsurface seismic profiles' spatial resolution for comprehensive 3D modeling. The developed methods also were based on seismic interferometry to calculate the autocorrelation profiles of a minefield. The mining blast signals were proposed and evaluated as a high frequency, and amplitude seismic source, which enabled to resolve of the shallower target lithologies and structures than other commonly used low-frequency sources (natural earthquakes and ambient noise) could resolve. The proposed approaches in this dissertation have been successfully used to retrieve the P-wave reflectivity and high-resolution seismic images for the relatively deep structures and faults, even though the complex, highly faulted structures, and shallow deposited salt layers were dominant (chapter 2). The developed methods also could successfully resolve the shallow lithological boundaries associated with commercial ore deposits by obtaining high-resolution profiles although the presence of shallow volcanic geological formations (chapter 3).

Chapter 1 outlined the research background, motivation, and objectives. In this chapter, the simple and general definitions were explained. Some examples of previous studies related to the seismic attributes' utilization and the seismic interferometry methods mentioned that have been used in imaging the subsurface geological structures related to the Earth's resources.

Chapter 2 proposed a developed approach to use the post-stacked reflection seismic (P-wave) and well data comprising the check shot velocity data from active sources (air gun) to obtain and investigate detailed information about the structural fault orientation and dip of the Ras El Ush field (Egypt). The seismic energy was masked by the Pre-Miocene salt formation and attenuated by evaporite deposits in the upper Miocene, complicating the seismic interpretation process. Therefore, suitable seismic attributes were introduced as seismic conditioning, structural smoothing, and 3D edge enhancement and fault detection for better visualization of the seismic profiles related to complex structures and high faulting zones that characterize this field and nearby areas of the Gulf of Suez active rift zone. In addition to constructing 3D structural models of the formations of primary interest to help define the geological discontinuities and structural traps for the development of the field. This study includes findings from seismic attributes analyses to enhance the detection of the Clysmic fault-offsetting aggregate and the minor and major cross faults that passed through the Ras El Ush field. Integrating explicate faults, horizons, and designated zones into a three-dimensional grid enabled detailed enhanced structural modeling.

Chapter 3 presents an advanced approach that evaluates the potential of autocorrelation analysis for investigating shallow subsurface lithological imaging, including the ore deposits, using high-frequency blast mining signals. By using autocorrelation analysis, seismic data from natural earthquakes, ambient noise, and mine blasts were analyzed to map P-wave reflection profiles in a case study to assess the method at the Hishikari mine area in Japan. The blasting in the mine was employed instead of the conventional sources (natural earthquakes and noises) because blast events contain high-frequency signals that improve the spatial resolution of the imaging. Gaussian smoothing and spectral whitening were used to eliminate source effects from seismic data, including blast events, and then the best frequency range was examined to extract P-wave reflections successfully. The stacking method was used to distinguish the dominant P-wave reflections to attenuate the incoherent signals or noise while boosting stationary signals. High-resolution seismic reflectors were detectable on auto-correlograms at shallow formation depths. Compared with natural or ambient seismic sources, blasting signals produced remarkably spatially consistent reflections that would not be allowed with natural or ambient seismic sources. The implementation of blast autocorrelation seismic analysis during short survey periods is highlighted in this study. Higher resolution 3D reflection images of lithological boundaries, potentially containing ore veins, were successfully obtained using a single blast shot and dense seismic station spacings.

Chapter 4 summarizes the dissertation content, the conclusions, and the key points. The complex formations dominating the Gulf of Suez, Egypt, could be resolved by building 3D structural models based on seismic and well-logging data and applying the appropriate seismic attributes, advanced processing, and interpretation techniques. Investigating and exploring different minefields that use blasts to extract potential minerals from hard rocks with an inexpensive technique like seismic autocorrelation methods may be possible using active sources like the blast mining signals.

4.2 Conclusions

Imaging the subsurface geological structures in geophysical research by integrating several advanced data processing methods and interpretation approaches have produced substantial results. Seismic interferometry and attributes could be optimally favorable for imaging high-resolution seismic profiles and building detailed 3D structural models. In chapter 2, the applied seismic reflection interpretation processes of the Ras El Us field could be one proper way for seismic imaging of the associated structures, sedimentation, and geological controls on the hydrocarbon systems of similar potential fields or other earth resources having similar geological systems as the potential geothermal sites. Also, the proposed data processing schemes on simple recorded seismic data in chapter 3 are suitable for obtaining high spatial resolution shallow subsurface structures. The key findings of this dissertation are summarized below:

Chapter 2 presents a detailed structural model for the Ras El Ush field (Gulf of Suez, Egypt) constructed based on seismic and well-logging data. Implementing seismic attributes complemented offshore subsurface structural features, such as up-thrown trapping, subsalt structures, fault interpretation, and related possible hydrocarbon structural trap occurrence. The approach in this study offers clues to unlock some of the secrets of the active rift and its structural aspects on the fluid dynamics and explore undiscovered reserves. Also, the results of this study provide recent geologic structural updates that could be helpful for possible future enhanced recovery methods of oil and gas among previously drilled reserves of deeper formations such as Matulla and Nubia sandstones as Nukhul, Rudeis, Kareem, and Belayim. The structural evaluation of the Rudeis, Nukhul and Matulla formations in the Ras El Ush field exhibits distinct NW-SE to NE-SW fault systems. The final extracted 3D modeling subdivided the research area into several blocks, allowing future selection of appropriate wells in the area and offering insights into Ras El Ush's structural framework. Also, this model could be utilized to re-evaluate the hydrocarbon potentially within relatively shallower formations such as Rudeis and Nukhul formations. The structural model can be used in future monitoring and investigating variations in the complex structures' physical properties due to various tectonic stresses dominating the Gulf of Suez as the area lies in the active rift zone. Finally, this study suggests reprocessing the post-stacked seismic data of REU to achieve more accurate interpretation and high-resolution pre-salt images, especially for the productive layers such as Nubia, Matulla, and Lower Miocene formations.

Chapter 3 reveals that the seismic interferometry based on autocorrelation analysis of natural earthquake- or ambient noise-derived seismic signals has limited resolution at shallow depths. Therefore, the developed approach using buried artificial mine explosions as a seismic source was vital in constructing high-resolution shallow imaging. By autocorrelation analysis of the blast signal, we extracted 1D P-wave reflection profiles below seismometers and 3D structural information using many seismometers from the mine explosions. Because the blast signals contain high-frequency components over a wide frequency range, the resulting autocorrelation represents shallow lithological boundaries. The dense station spacing used during our single-day survey enabled us to image lithological boundaries from the surface to around 500 m depth at very high lateral and vertical resolution using only a single blast signal. Thus, exploiting mining blasts as seismic sources can effectively explore mining sites, including ore deposits, within a short time and without the need for additional artificial sources.

The research in this dissertation opens new opportunities to implement the following research:

1. The discussion in chapter 2 emphasizes that the pre and post-stacked processing and suitable seismic attributes could be used to achieve a reasonable and more accurate interpretation and pre-salt image. Integration of recent advanced seismic reprocessing techniques such as adaptive beam migration (ABM) and 3D depth/time migration should be applied to the pre-stacked seismic data of the REU area. These processing methods could clearly identify cases requiring multi-arrival (multi-component)

imaging, steeply dipping, and/or overturned structures below complicated salt bodies. Higher-resolution pre-salt images require a precise post-salt velocity model. A combination of tilted transverse isotropy (TTI) tomography and full waveform inversion (FWI) should be applied. Also, the utilization of seismic reflection and well logging data for building detailed 3D structural models showing the geological discontinuities and structural traps, which would help in the development of the field and similar hydrocarbon fields or the exploration of geologically comparable earth resource fields, including potential geothermal fields

2. The discussion in chapter 3 showed that, in general, the active source seismic exploration has a higher spatial resolution image than passive source (e.g., natural earthquake and ambient noise) exploration with significantly low cost of the used method compared to other active sources. However, manipulating the mine explosions as seismic sources can be a helpful strategy for prompt and cost-effective investigation of the mining sites, including ore resources, without the necessity of additional sources. Therefore, this case study evaluated the possibility of using this method in other minefields or potential targets with similar geological settings. Because the blast signals have the merits of containing high-frequency components over a wide frequency range, the explosions occur at buried depths close to the target resource compared to other seismic sources, such as a natural earthquake. Even though, the feasibility of using other high-frequency active sources could also be investigated, such as vibroseis, falling weights, and other continuously controlled seismic source systems (such as Accurately Controlled Routinely Operated Signal System (ACROSS) (Maeda

et al., 2015; Tsuji et al., 2021; Suzuki et al., 2021) and Portable Active Seismic Source (PASS) systems) (Tsuji et al., 2022) for imaging the subsurface geological structures of the potential fields by seismic interferometry methods.

4.3 References

Maeda, Y., Yamaoka, K., Miyamachi, H., Watanabe, T., Kunitomo, T., Ikuta, R., Yakiwara, H. and Iguchi, M. (2015). 'A subsurface structure change associated with the eruptive activity at Sakurajima Volcano, Japan, inferred from an accurately controlled source. Geophys Res Lett 42, pp. 5179-5186. doi: 10.1029/2011GL048800.

Suzuki, R., Yamaoka, K., Tsuji, S., Watanabe, T. (2021). 'Ground water-induced changes in velocities of P and S waves (Vp and Vs) measured using an accurately controlled seismic source'. Earth Planets Space 73, 152. doi: 10.1186/s40623-021-01484-3

Tsuji, T., Tsuji, S., Kinoshita, J., Ikeda, T., Ahmad, A. B. (2022). '4 cm Portable Active Seismic Source (PASS) for meter-to kilometer-scale imaging and monitoring of subsurface structures' Seismological research letters. doi: 10.1785/0220220049.

Tsuji, T., Ikeda, T., Matsuura, R., Mukumoto, K., Hutapea, F. L., Kimura, T., Yamoka, K., and Shinohara M. (2021). 'Continous monitoring system for safe managements of CO_2 storage and geothermal reservoirs' Sci Rep 11, 19120. doi: 10.1038/s41598-021-97881-5.